Fabrication of a Lung-on-chip Microfluidic Device Suited for Modeling the Alveolar-capillary Interface in a Healthy Lung and in a Lung with Adult Respiratory Distress Syndrome

By

Rachel Hattaway

Submitted to the graduate degree program in Bioengineering and the Graduate Faculty of the University of Kansas in partial fulfillment of the requirements for the degree of Master of Science.

Committee Members:

_____

Prajnaparamita Dhar, Ph.D.
(Chairperson)

_____

Susan Lunte, Ph.D.

_____

Karen Nordheden, Ph.D.

Date Defended: December 13, 2017

The Thesis Committee for Rachel Hattaway certifies that this is the approved version of the following thesis:

Fabrication of a Lung-on-chip Microfluidic Device Suited for Modeling the Alveolar-capillary Interface in a Healthy Lung and in a Lung with Adult Respiratory Distress Syndrome

By

Rachel Hattaway

_____

Prajnaparamita Dhar, Ph.D.
(Chairperson)

Date Approved: December 15, 2017

Abstract

With each breath, the mammalian lung must undergo a sequence of expansion and compression, bringing fresh air into the lungs and exhaling waste carbon dioxide. As that air is bought into the lungs it flows through structures of increasingly small dimensions, maximizing the surface area available, until reaching the alveoli, the cellular structures responsible for gas exchange. With healthy lungs we are able to breathe with an ease that belies the complexity of the lung surfactant (LS) at work, enabling us to do so. At the cellular level a monolayer of lung surfactant, a lipid-protein mixture, coats the alveolar surface and minimizes the work required to inhale. LS has evolved to meet the demands of this expansion-compression cycle. Among these are spreading rapidly during inhalation, minimizing the surface tension but resisting monolayer collapse during exhalation, and acting as a barrier to the outside world. To meet these requirements, therefore, LS must consist of many components acting in concert.

With such an important task, it comes as no surprise that the lack of LS or its dysfunction can result in disease states. For instance, a condition known as neonatal respiratory distress syndrome (NRDS) occurs in infants born prematurely, because in these babies the alveolar cells have not yet formed or secreted enough LS. These infants cannot overcome the additional work required to breathe and must undergo replacement LS therapy. In adult patients, existing surfactant can be displaced or inactivated by fluid buildup in the alveoli due to injury or illness in a condition collectively known as adult respiratory syndrome (ARDS). Treatment of these conditions using LS therapies could be improved or discovered with increased knowledge of the ways in which LS components interact at a molecular level to result in desired surfactant properties.

The evaluation of lipid-protein interactions is a primary focus of our lab. Work of this nature is typically done using a Langmuir Trough coupled with Wilhelmy plate surface pressure

measurements and fluorescent imaging. A microrheology system using magnetic nanorods has also enabled detection of small changes in interfacial viscosity that could not be detected by commercial rheometers. However, in order to truly evaluate LS properties, it is necessary to match the microscale environment of the alveoli as closely as possible. To this end, this thesis discusses the construction of a lung-on-chip device with the goal of creating an *in vitro* model of lung function that could be used in combination with the LS evaluation methods currently used in our lab.

The lung model discussed here consists of a three layer microfluidic device constructed entirely of polydimethylsiloxane (PDMS) polymer. This device was constructed using microfabrication techniques capable of creating a microenvironment mimicking that of the alveolar-capillary interface. The model consists of top and bottom center channels separated laterally by a porous membrane (PM) and flanked by functional side channels. The top and bottom center channels create the alveolar and capillary sides of the interface, respectively. The flanking side channels serve to simulate breathing by subjecting the PM of the center channel to expansion and compression caused by cyclic application of negative pressure on the side channels. The PM serves as the scaffold on which alveolar cells and endothelial cells can be grown to create the *in vitro* model and can withstand the stretching associated with simulated breathing. Methods of microfabricating an intact porous membrane with through-holes were evaluated. Additionally, two methods of opening the top center channel of the device, CO_2 laser ablation and precision milling via CNC, in order to create a true open air-liquid interface were evaluated.

Acknowledgment

I would like to begin by thanking my advisor, Dr. Prajnaparamita Dhar for her continued support and guidance throughout the entirety of this project. I cannot begin to express my gratitude that she helped me see this through to the end. Additionally, it was my pleasure to be Dr. Dhar's teaching assistant for multiple semesters. I have appreciated and greatly benefited from her enthusiasm and dedication, which she applies equally to her research and teaching.

I am also grateful for my committee members, Dr. Karen Nordheden and Dr. Sue Lunte. Karen, who was my undergraduate advisor in the Chemical Engineering Department, has been a mentor since long before I began graduate school. Sue, through her part in the creation of the Adams Microfabrication Facility and her hard work in securing the COBRE grant, made this work possible. Furthermore, I value the opportunity that I have had to work for Sue as a microfabrication technician in the Adams Microfabrication Facility. This opportunity allowed me to take the microfabrication skills I learned from my work in Dr. Dhar's lab and expand on them, ultimately, helping to build my confidence.

To the members of the Dhar Lab, past and present, I have enjoyed the times when our work overlapped. Since most of my time was spent hidden away in the cleanroom, these instances were few and far between, but they were appreciated. Aishik Chakraborty, I enjoyed being teaching assistants together and swapping movie suggestions. Coleman Vaclaw, I appreciated your detailed origin spreadsheet for microrheology and sharing classes with you. To Dr. Lorena Antunez and Dr. Nabil Alhakamy, thank you both for my introduction to cell culturing. And finally, to Dr. Saba Ghazvini, thank you for your persistent encouragement both in and out of the lab. Your friendship helped me through the many struggles that go hand in hand with graduate school. I fondly

remember the times we spent trying to distract ourselves from these problems by going out to eat on Mass street, and I look forward to many more shared meals together.

To my brother, Jeff, and his daughter, Ivy; to my sister, Sarah, and her son (and our newest addition), Harrison; but most of all to my mom, Kathleen, thank you all for your understanding. There were times that I didn't prioritize family as much as I would have liked to during this process. I am lucky to have you all and I appreciate the times that you gave balance to my life. In my experiences as an Aunt, I have realized that there is no better way to live in the moment, than to spend time with the children in your life. Mom, your love and support was always there when I needed it. Thank you for the trips you made to Lawrence to spend time with me. When I move out of Kansas, I will miss those short (and sometimes, surprise) visits.

To my partner in life, Nate, your support has been unwavering and I could not have made it to this point without it. Your belief in me kept me going and gave me faith in myself. Despite your inability to let go of your own projects, you still found time for me, even while progressing through your own degree. When you defended your Ph.D., I was proud and I shared a little in your accomplishment. I hope that you do the same, now, as I complete my master's degree. We are at the interface (pun intended) between two phases of our lives, and I can't wait to see what this next one brings us. I love you, now and always. The sentiment of this paragraph is also extended to our dog, Pete, who has become my unofficial emotional support dog. I couldn't have done it without you either, Pete.

Table of Contents

List of Figures

List of Tables

1. Introduction

1.1 Background and Motivation for the Fabrication of a Lung-on-chip

A healthy adult at rest takes on average 12-20 breaths per minute [1] or tens of thousands of breaths per day without needing to give it a single thought. The ease with which we breathe is actually quite misleading with regard to the complexities that enable us to do so. With each inhaled breath, the expanding lungs bring oxygen-rich air in, first in through the mouth or nose, through the trachea, branching into bronchi, into smaller bronchioles, further still into the alveolar sacs and finally into the smallest structures of the lungs: the alveoli (Figure 1). Once the air reaches the alveoli, oxygen (O_2) and carbon dioxide (CO_2) are exchanged as O_2 diffuses into (and CO_2 out of) the blood through the capillaries lining the exterior of the alveoli. Respiration of this one breath is completed upon exhalation, or expiration, which expels the carbon dioxide rich air from the lungs [2]. For the respiration cycle to occur, the lungs must undergo dramatic changes in surface area, as the volume of the lungs increases during inspiration and decreases during expiration.

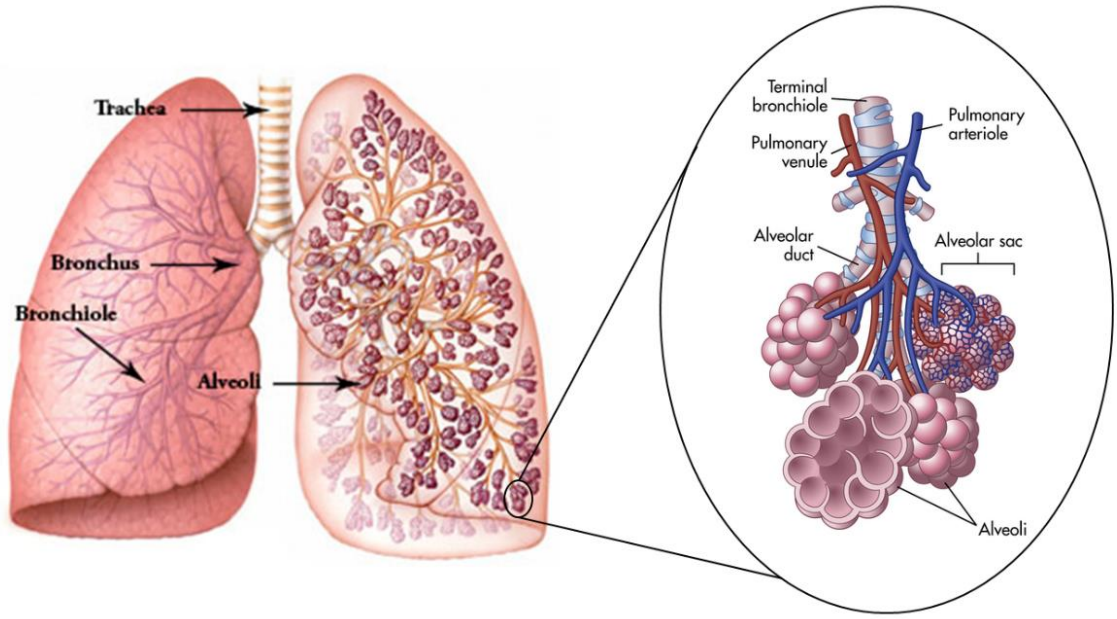

Figure 1: A schematic of lung physiology. Air enters the trachea, continues through the highly branched structure of the lungs to the capillary-lined alveoli, where gas exchange occurs. Reprinted with permission from [3].

This expansion-compression cycle in the lungs is made possible by lung surfactant (LS), which lines the inside of the alveoli as a monolayer film. Surfactants are **surf**ace **act**ive **a**ge**nts** that decrease the surface tension at the interface of two immiscible liquids; a liquid and a solid; or that of a liquid and a gas [4]. Lung surfactant, true to its name, serves to regulate the surface tension at the air-liquid interface found within each of the hundreds of millions of alveoli of the human lung. Upon expiration, the surfactant film compresses and the surface tension reaches near zero millinewton per meter (mN/m), reducing the energy required to re-expand the lungs, all while the LS monolayer remains rigid enough to prevent irreversible collapse of the alveoli [5, 6]. Surface tension, however, is not the only consideration. Viscosity of the LS is also important, because during inspiration the surface viscosity of the LS must be sufficiently low to allow for rapid spreading over the expanding alveoli [7]. By balancing these mechanical properties, LS enables the alveoli to function during both the inspiration and expiration phases of breathing. The LS film also functions as a barrier to the outside world, preventing infection from inhaled pathogens [6]. Due to these varied requirements, lung surfactant is actually a mix of lipids and proteins, all working in concert to reach an optimal tradeoff of tension and fluidity.

LS is composed primarily of phospholipids (80 wt. %), proteins (10 wt. %), and neutral lipids (10 wt. %) [8]. As phospholipids have a hydrophilic headgroups and hydrophobic tails, they find it energetically favorable to orient themselves such that the hydrophilic headgroups are adsorbed to the aqueous side of the alveoli's air-liquid interface and the tails protrude out into the air side (Figure 2A). The most abundant phospholipid head group in LS is phosphatidylcholine (PC) and the majority of these PC lipids exist in the saturated form: dipalmitoylphosphatidylcholine (DPPC) (Figure 2C). DPPC has two saturated palmitic acid tails that allow it to pack tightly upon compression. While DPPC is known to form a rigid monolayer and to reduce the surface tension

to near zero mN/m, effectively reducing the work needed to breathe, it does not adsorb from the subphase to the air-liquid interface at a rate that would allow for rapid respreading of the LS over the expanding alveoli [6]. In fact, none of the LS phospholipids alone can provide the mechanical properties required during both phases of breathing. The addition of unsaturated lipids, which do not pack as tightly as DPPC, lower LS viscosity, facilitating more rapid adsorption and respreading of the LS monolayer [7]. These unsaturated phospholipids mostly have PC headgroups but smaller fractions of phosphatidylglycerol (PG), phosphatidylinositol (PI), and phosphatidylethanolamine (PE) lipids are also present in both saturated and unsaturated forms. Finally, the neutral lipids, such as free fatty acids, sphingomyelin, triglycerides and cholesterol, give additional fluidity to the LS mixture [6].

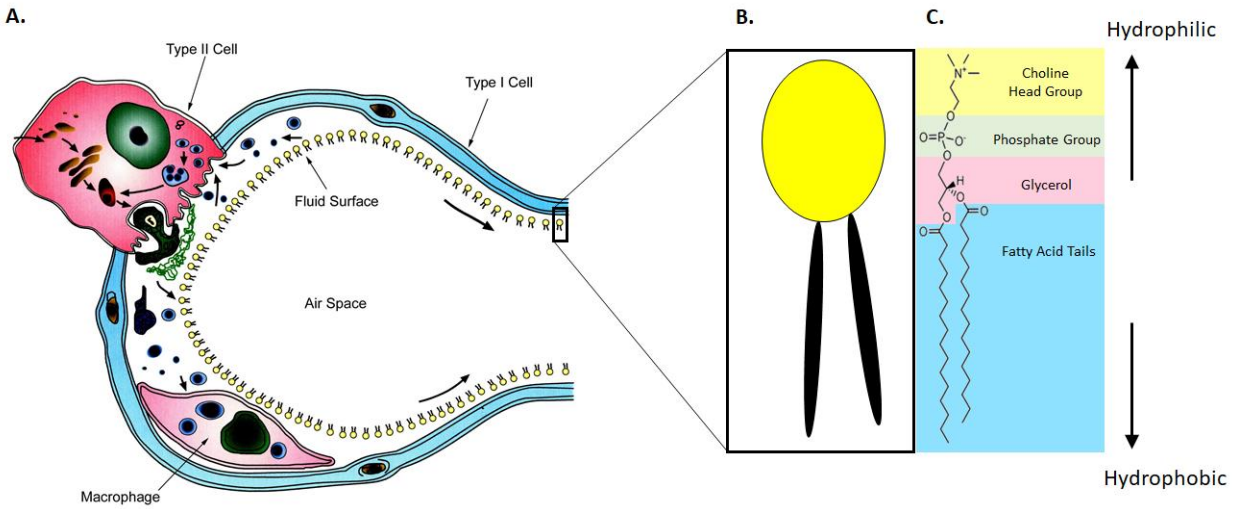

Figure 2: A) Schematic of an alveolus with a LS monolayer at the air-liquid interface reprinted with permission from [9]. The hydrophilic headgroups of the phospholipids adsorb to the aqueous subphase and the hydrophobic tails protrude into the air. B) Cartoon image of a LS phospholipid. C) Chemical structure of DPPC, the most abundant phospholipid in LS, with functional groups indicated.

The protein portion of LS consists of surfactant proteins A, B, C and D (SP-A, SP-B, SP-C, and SP-D). SP-B and SP-C are hydrophobic and help with attaining near zero surface tensions and with the adsorption of LS from the aqueous subphase after collapse, making them beneficial for

both phases of breathing. SP-A and SP-D, however, are hydrophilic proteins that remain in the bulk aqueous subphase and have not been shown to play a significant role in the mechanical properties of the LS monolayer, but are important in the innate immune response [6]. This mixture of phospholipids and proteins allows the seemingly opposing monolayer mechanical properties (rigidity and fluidity) of LS to be met during both the inspiration and expiration phases of breathing.

Given how important LS is to alveolar function it should come as no surprise that its absence or dysfunction results in significant disease states. Type II alveolar epithelial cells, which make up only 5% of the alveolar surface, are responsible for the synthesis, secretion, reuptake and recycling of the LS lipids and proteins [6, 10]. These cells are not formed until 24-26 weeks into fetal gestation and do not produce adequate quantities of lung surfactant to support breathing until 33-36 weeks gestation, when rapid lung maturation occurs [11, 12]. Therefore, premature babies often suffer from neonatal respiratory distress syndrome (NRDS) and the incidence of NRDS increases with increasing prematurity. Newborns suffering from NRDS are unable overcome the increased work of breathing, due to the lack of LS, without the medical intervention of a mechanical ventilator. According to data collected by the American Thoracic Society, NRDS affects about 1% of newborn babies. More significantly, NRDS is the leading cause of death in premature infants [13].

The restoration of normal lung function in NRDS patients is accomplished by replacing the missing LS with exogenous LS, either synthetic or an animal-derived. This surfactant replacement therapy has been in use for close to three decades, having first been demonstrated as safe and effective in the early 1990s [10]. Almost all of the first available replacement lung surfactants for clinical use in the US were animal-derived: Curosurf (cow), Infasurf (calf) and Survanta (pig),

which although clinically effective, can include impurities and thus further compromise the health of an already fragile patient through an immune response. Synthetic replacement LS is less expensive to produce and does not come with the risk of inflammatory response that animal-derived surfactants do, but producing a formulation capable of recapitulating the mechanical properties of native LS is quite difficult [14].

Another disease state, Acute Respiratory Distress Syndrome (ARDS), differs from NRDS in that the LS is present, but it has been displaced, or inactivated, by fluid buildup in the lungs due to severe injury or disease. This characteristic fluid buildup disrupts the LS monolayer and thus LS function and breathing. Unlike NRDS, which essentially has a single cause, ARDS encompasses critically impaired breathing as a result of a wide variety of causes, making it much more difficult to treat. According to the American Lung Association there are approximately 200,000 ARDS cases per year in the United States and the mortality rate is between 30-50% [15]. The mortality rate is high because ARDS occurs in critically ill patients and progresses rapidly. Clinical treatment of ARDS with surfactant replacement therapy has not been widely successful so far [16].

Replacement LS formulations differ in composition of phospholipids and proteins based on the source, procedure, and solvents used in production [10, 14], and there is not a consensus on whether or not cholesterol should be present at all [17]. Given the differences in formulation, and the complexity of LS function generally, additional study is necessary to determine the optimal concentration of each component of the LS mixture. With a better understanding of the mechanical properties provided by each individual component and how the components interact together in mixtures, synthetic replacement LS with ideal properties and no inflammatory response could be designed to better treat NRDS. Furthermore, characterizing the interfacial mechanical properties of LS could aid in the design of tunable surfactant replacement therapies for the complex disease

state of ARDS that, when combined with additional clinical therapies, would be capable of preventing further disruption of LS and restoring its natural function.

Recent work by the Dhar lab has aimed to characterize LS monolayers and understand how the individual components interact and affect the LS mixture as a whole. Measuring the interfacial surface viscosities of LS monolayers is difficult because separating the properties of the subphase from the interface is challenging. This limitation has been addressed through the use of magnetic nanorods rotating at the fluid interface in response to an applied external magnetic field (active rheology). By recording the turning nanorod with digital imaging and then balancing the magnetic and viscous forces, the surface viscosity can be obtained [18]. Decreasing the size of the rheological probe (the magnetic nanorod), helps to decouple the interfacial and bulk properties and has made it possible to detect more subtle changes in the surface viscosity of lipid monolayers compared to current commercial rheometers [18]. This method has been used in our lab to measure the viscosities of phosphatidylethanolamine monolayers with the system seen in Figure 3 [19].

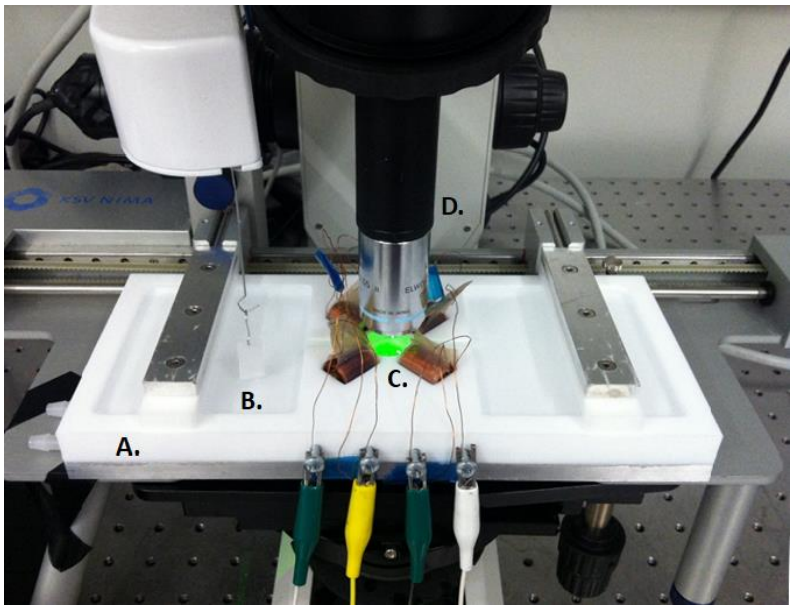

Figure 3: A novel Langmuir trough (A) coupled with Wilhelmy plate (B) surface pressure measurements, magnetic coils (C) for active microrheology, and fluorescent microscopy (D) for domain imaging and recording the turning nanorods. This system provides a lot of information regarding interfacial rheological properties, but it does not recapitulate the alveoli microenvironment. Reprinted with permission from [19].

Furthermore, unpublished work has measured viscosities of lipid-protein mixtures that mimic LS to quantify the effect of unsaturated tails, headgroup charge, and the presence of a synthetic analog of SP-B, Mini-B, on the mechanical properties of lipid monolayers. In addition to surface viscosity measurements, Langmuir troughs are used to obtain surface pressure-area isotherms and coupled with fluorescent imaging to study phase transitions and monolayer collapse. Specifically, recent work has shown that the addition of Mini-B can offset the tendency for cholesterol to have deleterious effects on reaching near zero surface tension upon expiration [17].

While these studies have added to the understanding of LS monolayers, they have been limited in that they did not account for the microenvironment of the alveoli. In order to properly mimic the environment at the alveolar scale, the system must incorporate the expansion and compression of the LS monolayer to simulate "breathing" with living alveolar cells inside a microenvironment. With this motivation in mind, this work focuses on the fabrication of a lung-on-chip, an *in vitro* model of the lung alveoli, capable of doing so. The same techniques mentioned previously, such as microrheology with nanorods, imaging, and surface tension measurements can be used with this model to verify and further understand the mechanical properties of LS components and mixtures. Additionally, the design of this microenvironment is well suited for an ARDS surfactant model. To this end, a microfluidic lung-on-chip system is the focus of the following sections.

1.2 From Microfluidics to Organs-on-chips

Microfluidics is a term applied to systems designed to handle extremely small fluid volumes that are manipulated in equally small channels. The channels in these systems are on the scale of tens to hundreds of microns (μm) and are typically used with fluid volumes on the order of 10^{-6} to 10^{-18} liters [20]. The ability to handle these vanishingly small amounts of liquid have made

microfluidic systems very attractive to fields such as medical diagnostics and bioanalysis, in which small sample sizes are desirable. As a field, microfluidics originated through an adaptation of microfabrication techniques used in the semiconductor industry [21]. Beginning in the middle part of the 20th century, the development of integrated circuits containing thousands to billons of components necessitated the development of new methods of manufacturing to create structures at the micron scale. Chief among these were photolithographic methods that used light exposure to faithfully transfer desired patterns, creating complex circuits for microelectronics [22]. These manufacturing techniques easily translated to the field of microfluidics, where they created fluid channels as opposed to circuits. These microfabrication techniques as they pertain to microfluidics are discussed in detail in Chapter 2.

Initially, the ability to create microchannels in hard materials such as glass allowed analytical techniques to be rendered in microfluidic formats [23]. These methods work well when using extremely narrow channel dimensions, and were therefore well placed to take advantage of the developments in microfabrication. However, the use of rigid, gas impermeable substrates such as glass posed limitations with regard to the types of assays that could be developed especially in terms of cell research. With the development of polymer based methods, most notably that of polydimethylsiloxane (PDMS) in the late 1990's by the Whitesides group, these limitations were overcome [24].

PDMS has many properties that make it ideal for the construction of microfluidic devices (microdevices). First among these is that it is optically clear and thus ideal for imaging. Second, PDMS has excellent bonding abilities and can produce an irreversible seal with other PDMS layers or substrates such as glass, following an oxidation step [24, 25]. The ability to seal in this way allows the microdevice to withstand pressures from syringe pump produced fluid flows or from

pneumatic controls. It also allows for complex, multilayer PDMS devices. Unlike glass and silicon, PDMS is gas permeable and thus provides a biocompatible surface upon which cells can be grown, leading to the coupling of *in vitro* models and microfluidics [26]. PDMS remains soft and flexible following the polymerization step but maintains a high mechanical durability, an attribute that has enabled the integration of mechanical valves into devices, greatly expanding the realm of functionality [20, 26, 27]. Additionally, creating microdevices through casting of PDMS onto silicon molds makes it possible to repeatedly create identical devices [28]. Finally, PDMS is inexpensive and easy to use, allowing rapid prototyping of designs without significant investments [29].

These attributes of PDMS have led to an explosion of novel *in vitro* assays in recent years as more and more functions have been moved to microdevices. These include DNA sequencing and polymerase chain reaction (PCR) for rapid sample identification [29], on-line monitoring of neurological damage [30, 31], cell cytometry [27], and importantly for the goal of this work, the development of on-chip cell culturing [32]. These analytical devices have become known collectively as "lab-on-chip" devices in reference to the electronic microchips from which the microfabrication methods originated. Their goal is to integrate the function of a lab into a single microdevice, allowing researchers to utilize small sample sizes such as single drops of blood. Lab-on-chips offer the promise of portability with decreased costs, because they are significantly smaller [33].

Advances in lab-on-chip microengineering and the ability to grow cells directly within three-dimensional (3D) geometries has also enabled organ-on-chip devices to be created. The motivation behind such work has primarily been driven by the drug discovery field in an effort to decrease the substantial time and costs involved in bringing drugs to market. By some measures, developing

a single drug can exceed a cost of $800 million [34] with only 10% to 30% of those drugs making it to market [35]. A large percentage of these costs is due to the process of pre-clinical animal studies which while necessary, are very time consuming and often inaccurate as successful testing in animals does not necessarily predict successful outcomes in patient testing [36-38]. In contrast, Organ-on-chip devices, which can be produced using human cell lines, promise significant cost savings and provide *in vitro* studies of human tissue responses. Furthermore, organ-on-chip devices recapitulate the microenvironment of complex tissue-tissue interfaces, including the mechanical and chemical cues provided by the dynamic microenvironment, features that traditional two-dimensional (2D) cell culture methods lack [39]. Work in this field has produced a variety of organ systems including the lung [40, 41], the heart [42], the intestine [43], and the liver [44], leading some to speculate that the future of such research lies with a "human-on-chip", integrating multiple organ-on-chip platforms, complete with blood circulation [36-38, 45].

1.3 Lung-on-chip: an *In Vitro* Model of the Alveolar-capillary Interface

The focus of this work, is the fabrication of a lung-on-chip model initially developed by Huh et al. (Figure 4) [41]. This device was developed as an *in vitro* model of human lung function at the alveolar-capillary interface. This biomimetic microsystem is constructed from three individual layers of PDMS. The middle PDMS layer is a 10 μm thick porous membrane, which is essentially the flexible scaffolding upon which human cells are grown, mimicking the alveolar-capillary interface. The top and bottom PDMS layers of the device both contain a center 400 μm wide channel flanked by 200 μm wide side channels, all of which are 100 μm tall. When layered, the center channels of the top and bottom layers become one compartmentalized channel, divided by the porous membrane. The side channels provide the functional aspect of this microenvironment. Once the device is assembled, the porous membrane is etched from both of the layered side

channels, creating large side chambers. When negative pressure is applied to these side chambers, the sidewalls, which separate the center channel from the side chambers, bow inwards narrowing the side chambers, while stretching the porous membrane of the center channel. This cyclic stretching creates a biologically-relevant 10% strain on the porous membrane and thus on the cultured cells in the completed lung-on-chip device, thereby recapitulating the mechanical cues experienced by the same cells *in vivo* during breathing.

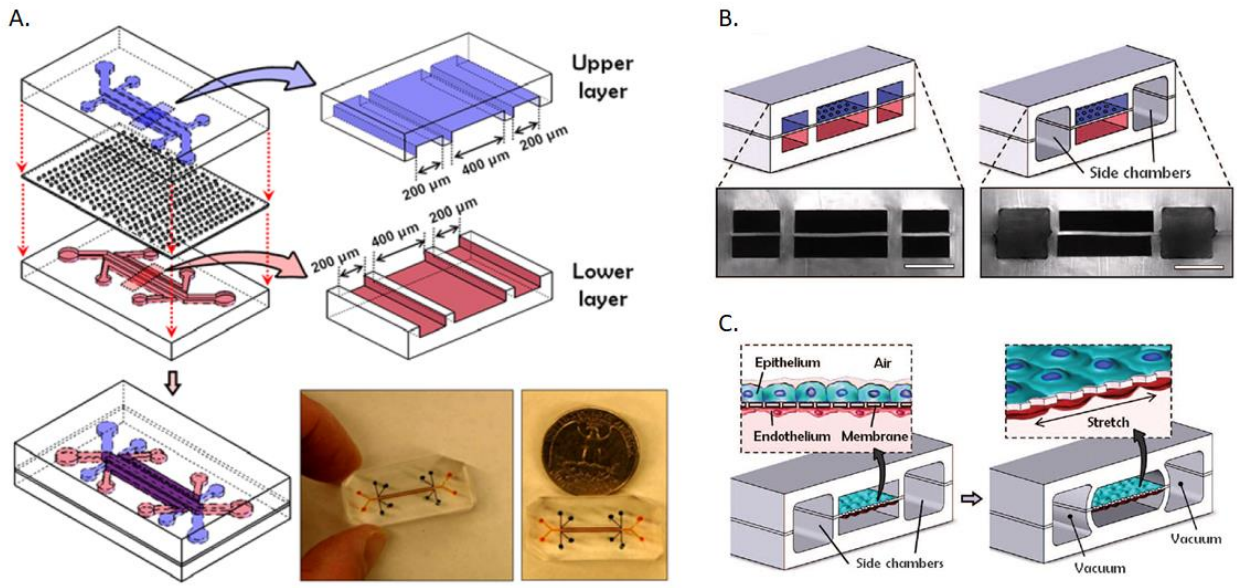

Figure 4: The lung-on-chip device designed by Huh et al. [41], reprinted with permission. A) Schematics of the three PDMS layers and how they align; the channel dimensions of the top and bottom layers; and images of completed device with a quarter for scale. B) Cross-sectional schematic (and images) of the device before and after etching the side channels to create side chambers. C) Cross-sectional schematic of the device with cultured cells (left) and when negative pressure is applied to the side chambers to stretch the PM to simulate breathing (right).

Upon assembling the three layers and etching of the side channels, human alveolar epithelial cells and human pulmonary microvascular endothelial cells are cultured on opposing sides of the porous membrane within the device. The compartmentalized center channel with cultured cells, has an alveolar air side (created by the top layer) and a vascular side (created by the bottom layer). Using this lung-on-chip device Huh et al. introduced *Escherichia coli* bacteria into the alveolar channel

and neutrophils into the vascular channel and monitored the inflammatory response. They found that the neutrophils were able to migrate through the interface to the alveolar side and the site of infection, demonstrating the ability of this lung-on-chip device to serve as a representative model for this tissue interface. This research also showed that the application of cyclic strain on the cells altered the cellular uptake of nanoparticles, demonstrating that the mechanical cues play a significant role in function [41]. The same device was also used to evaluate a model of pulmonary edema as a result of an acute dosage of interluekin-2 (IL-2). In modeling this, it was demonstrated that the addition of IL-2 to the vascular channel resulted in fluid leakage into the alveolar channel, accurately modeling the disease state [40].

While these examples show the lung-on-chip device can be used for modeling disease states, to date no investigations of LS interfacial properties or disease states such as ARDS resulting from LS dysfunction have been performed using the device. The vascular side (lower channel) of the compartmentalized channel allows for introduction of albumin into the alveolar side (upper channel) as it passes through the porous membrane, making the device well-suited for modeling ARDS, where LS is displaced by a buildup of fluid in the lungs. The construction of a device that could be used for such work is the subject of the following sections. We further investigate techniques that could be used to produce a more biologically representative air-liquid interface.

2. Description of Microfabrication Techniques

2.1 Photolithography for the Purpose of Making Master Wafers

Photolithography is a microfabrication technique used to create microstructures on a substrate using light at a specific wavelength to transfer the desired pattern. During this process, a polymer is coated onto a substrate, covered by a mask containing a pattern, exposed to a light source, and then preferentially removed during development, leaving behind the desired structures with a feature height determined by the coating process.

In this section the techniques behind the processes of photolithography, PDMS casting, and PDMS bonding that are used to create microfluidic devices are described. This includes a discussion of photoresist selection, mask type, and the process of photopolymerization that are all necessary for accurate pattern transfer as well as subsequent casting of the resulting mold and finally bonding of PDMS layers.

2.1.1 Photoresist Polymers

The photoreactive polymers used in standard photolithography are called photoresists and they fall into two main categories, positive or negative, based on how the photoresist responds chemically to a radiation source at a specific wavelength. Photoresist (PR) is composed of the polymer (or base resin), a solvent, and a sensitizer. The relief features created during the photolithography process will be made up of this resin, while the solvent is needed to decrease viscosity of the polymer. By decreasing the viscosity, the polymer will be less resistant to flow during the spin coating process, which allows the resist to both spread over the substrate and form a thin, uniform layer. The solvent is subsequently forced out of the polymer during baking steps, leaving a stable resin.

The third component of the PR, the sensitizer, is the photoreactive component of the photoresist and upon exposure to radiation at a certain wavelength, it changes the ability of the photoresist to chemically resist the developer solution. For positive PRs, the exposed regions of resist become sensitive to the developer whereas, the unexposed regions do not become more soluble. The development rate of the unexposed regions is significantly less than that of the exposed regions. In this manner the exposed regions can be preferentially removed (Figure 5D). For negative PRs, the reverse is true. The exposed regions become more resistant to the developer solution and the unexposed regions are preferentially removed.

Positive Photoresist

The positive photoresists commonly used in the Adams Microfabrication Facility, such as the AZ series PRs made by MicroChem, fall into the two-component category of positive PRs, because they include a sensitizer in addition to the resin. More specifically, the AZ resist series is of the diazoquinone ester (DQ) and phenolic novalac resin (N) or DQN family. Single component resists such as poly(methylmethacrylate) (PMMA) were the earliest positive photoresists. Although they, like other positive photoresists, become soluble by breakage of the polymer links in deep UV, they require long exposure times and organic developers due to the lack of sensitizer. The two-component DQN resists are more commonly used as they have much shorter exposure times at near UV, 365 nm, and are soluble in mildly alkaline developer solutions.

In the DQN resist family the novalac resin (N) (Figure 5A) ultimately provides the structure of the final resin pattern. It is not, however, photoactive. Rather, the DQ component reacts with the N component to create a photosensitive diazonapthoquinone (DNQ) compound. When this new compound is exposed to UV light, a carboxylic acid is formed that is preferentially removed based

on the development rate with a basic developer [46] (Figure 5B-C). The formation of carboxylic acid (Figure 5B) also requires water, making humidity control an important variable in fabrication. Consequently, a rehydration step is performed after the soft bake, prior to exposure. As stated previously for positive resists, exposed regions become soluble and are preferentially removed.

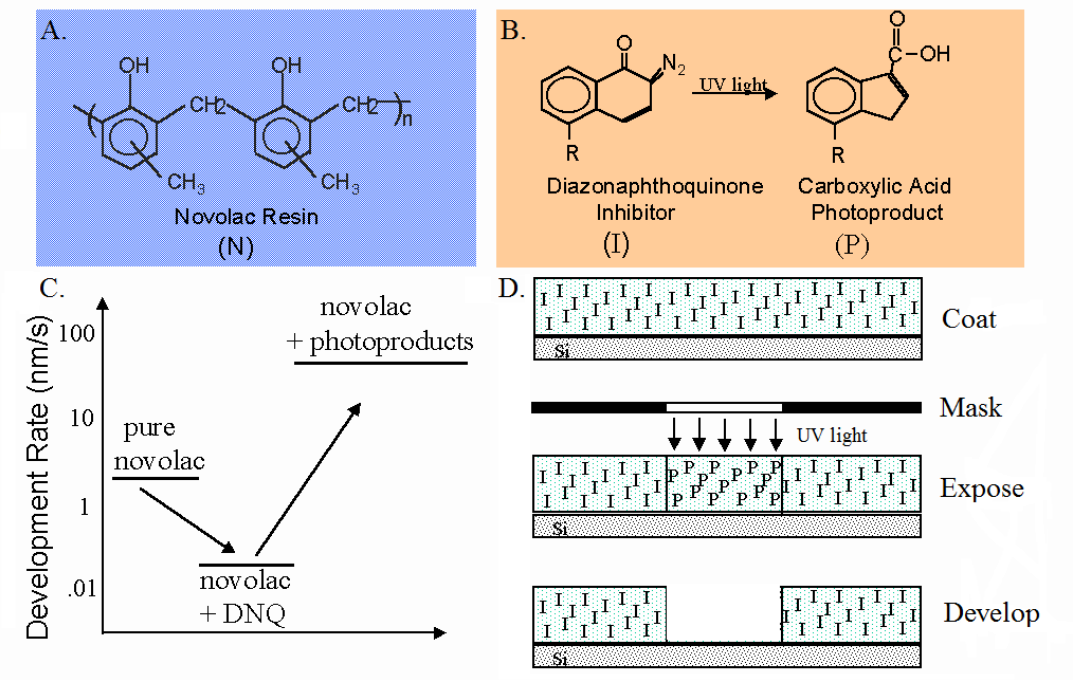

Figure 5: A) The chemical structure of the novalac resin (N). B) Chemical reaction of DNQ (labeled I) into carboxylic acid photoproduct (P) upon UV light exposure. C) A comparison of development rates for novalac resin, novalac resin plus sensitizer (DNQ) and novalac resin plus the carboxylic acid photoproduct. D) Schematic of the photolithography process with a DQN resist. Modified from [46, 47].

Negative Photoresist

The photoresist used for the purpose of making the lung-on-chip device, as described in Chapter 3, is a negative PR. Negative PRs function differently than positive PRs in that upon irradiation, the PR polymer becomes increasingly cross-linked in the exposed areas, rather than becoming more soluble in exposed areas. As the internal cross-linking of the polymer increases, so does its ability to withstand the developer solution. In the case of negative PRs, the areas that are exposed remain on the wafer and the unexposed areas are preferentially removed.

The negative PRs commonly used in the Adams Microfabrication Facility are of the SU-8 series made by MicroChem. As stated previously, both positive and negative PRs consist of three primary components: polymer, casting solvent and sensitizer. The SU-8 polymer (Figure 6A) consists of repeating bisphenol-A-novolac glycidyl ether monomers and on average each SU-8 molecule has eight epoxy groups. This average of eight epoxy groups is where the SU-8 PR derives its name. The SU-8 polymer is dissolved in an organic solvent and up to 10 wt. % of triarylsulfonium hexafluoroantimonate salt is added as a photo sensitizer [48]. To accommodate films ranging in thickness from 1 μm to 500 μm, the ratio of organic solvent to SU-8 polymer has been varied to create SU-8 formulations differing in viscosity. The greater the ratio of organic solvent to SU-8 resin, the lower the viscosity of the PR and the thinner the resulting film after spin coating.

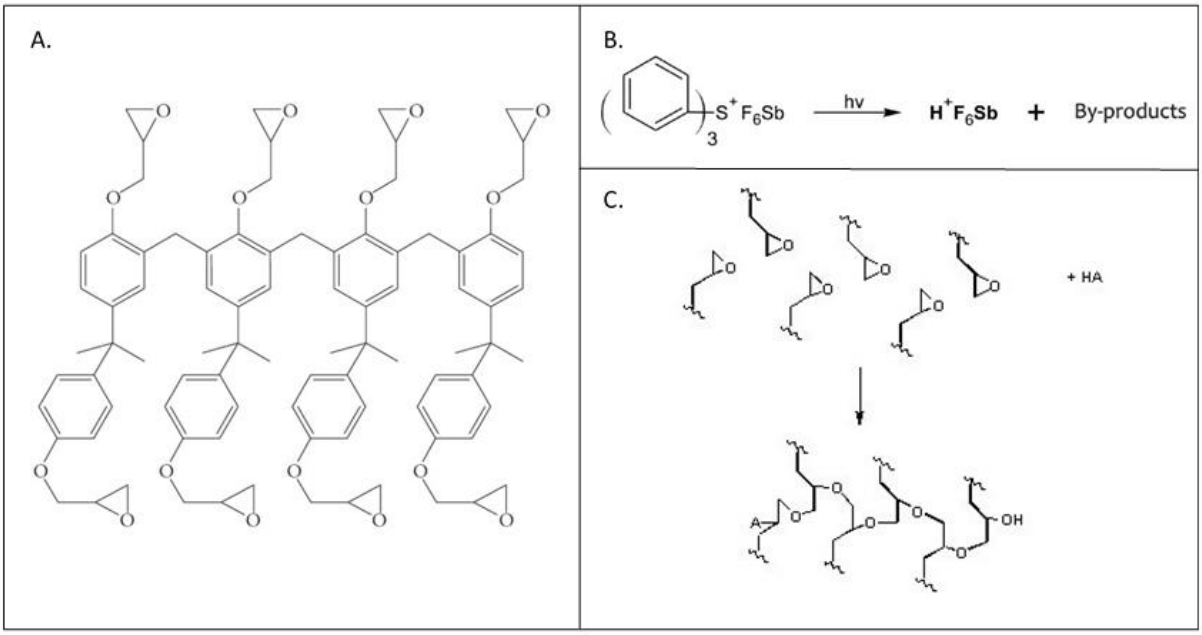

Figure 6: A) SU-8 polymer [48]. B) Formation of an acid by decomposition of the sensitizer salt during UV exposure [49]. C) Acid-catalyzed (H^+F_6Sb) polymerization of the SU-8 molecule at the epoxy groups [50].

Irradiation of the salt in exposed areas of the PR results in a low concentration of a strong acid, hexafluoroantimonic acid, formed through decomposition of the salt (Figure 6B). This acid

photoproduct can subsequently protonate many epoxide groups, opening the rings and catalyzing polymerization (Figure 6C). Cross-linking is further activated during the post exposure bake due to the elevated temperature. The acid-catalyzed cross-linking of the SU-8 polymer is considered to be a chemical amplification process since a single photon is able to produce an acid that in turn initiates multiple reactions, initiating polymerization [51].

Resist Requirements

For commercial purposes resists must be inexpensive, easily processed, and have a long shelf life. More importantly, for applications in microfabrication, resists must have high sensitivity, contrast, and purity; good adhesion, resolution, and chemical etching resistance; minimal solvent use; and a high glass transition temperature [22, 52]. Negative PR is typically the preferred choice of resist for soft lithography, because its adhesion to silicon wafers is superior. In soft lithography repeated casting of PDMS onto the master wafer and subsequent removal by peeling away, requires robust molds and thus good adhesion. Ultimately, the choice between positive and negative PR is highly dependent on a variety of design considerations. When photolithography is followed by etching to create microchannels in the substrate, positive photoresist is typically used, because it has better resolution. The minimum feature size for positive and negative PRs is approximately 0.5 μm and 2 μm, respectively [22].

Wafer Pretreatment

In the previous section positive and negative PRs were discussed, and it was mentioned that negative PRs are more commonly used in soft photolithography. From this point forward, the photolithography process will be discussed as it relates to the use of SU-8 PR in soft lithography

unless otherwise stated. It should be noted, however, that many of the principles behind these techniques apply regardless of the type of lithography, PR, or substrate.

Prior to PR deposition, silicon wafer substrates used in soft lithography need to undergo a pretreatment to promote adhesion of the PR. This is the first step in the overall process of photolithography for making master molds. This step is also called priming. At the very least new, clean silicon wafers should be baked at 200 °C for 30 minutes (min) or more to dehydrate the wafer immediately prior to spin coating. Dehydration is crucial because PR, which is hydrophobic, is repelled by moisture. Any moisture present on the wafer can result in poor spreading of the resist during PR deposition and ultimately poor adhesion of the PR to the wafer. If too much time passes between this bake and the spin coating step, the wafer will have time to rehydrate from atmospheric water vapor and adhesion will be adversely affected.

Other pretreatments include piranha baths or the application of hydrofluoric acid (HF). Piranha, which is a mixture of 30% hydrogen peroxide (H_2O_2) and concentrated sulfuric acid (H_2SO_4) in a 1:3 volume ratio, is used to completely strip any organic impurities from the surface of the wafer. Dilute HF is used to etch the silicon dioxide (SiO_2) film, leaving a bare Si surface on the wafer. This surface is hydrophobic, which although ideal for PR deposition, will react with atmospheric oxygen and water vapor to reform these bonds and over time and could also attract impurities. A dehydration bake is recommended after both piranha and HF priming and PR deposition should be performed as soon as the wafer has cooled.

Vapor deposition of hexamethyldisilazane (HMDS), an adhesion promoter for SU-8 PR, is the preferred pretreatment method in soft lithography. Vapor deposition of HMDS results in a hydrophobic surface, which allows the hydrophobic PR to flow more easily during deposition and further improves PR adhesion over simply dehydrating the wafer. The surface chemistry of this

process is shown below (Figure 7). Water adsorbed from air humidity onto the silanol surface of the silicon wafer results in polaric oxygen-hydrogen (OH) bonds (due to the strong dipole of H_2O). Following the application of heat, the adsorbed water is removed and the silanol surface returns, leaving a comparatively less hydrophilic surface with a decreased polarity (Figure 7A). The vapor deposition of HMDS creates a monolayer bound to the surface. The methyl groups of the HMDS monolayer provide a significantly increased hydrophobic area promoting adhesion of PR upon deposition. Unlike the other pretreatment methods mentioned above, a benefit to using HMDS is that the resulting monolayer resists rehydration of the wafer surface for an extended period of time [53]. Proper application of HMDS is necessary to obtain a HMDS monolayer as thick films of HMDS are undesirable.

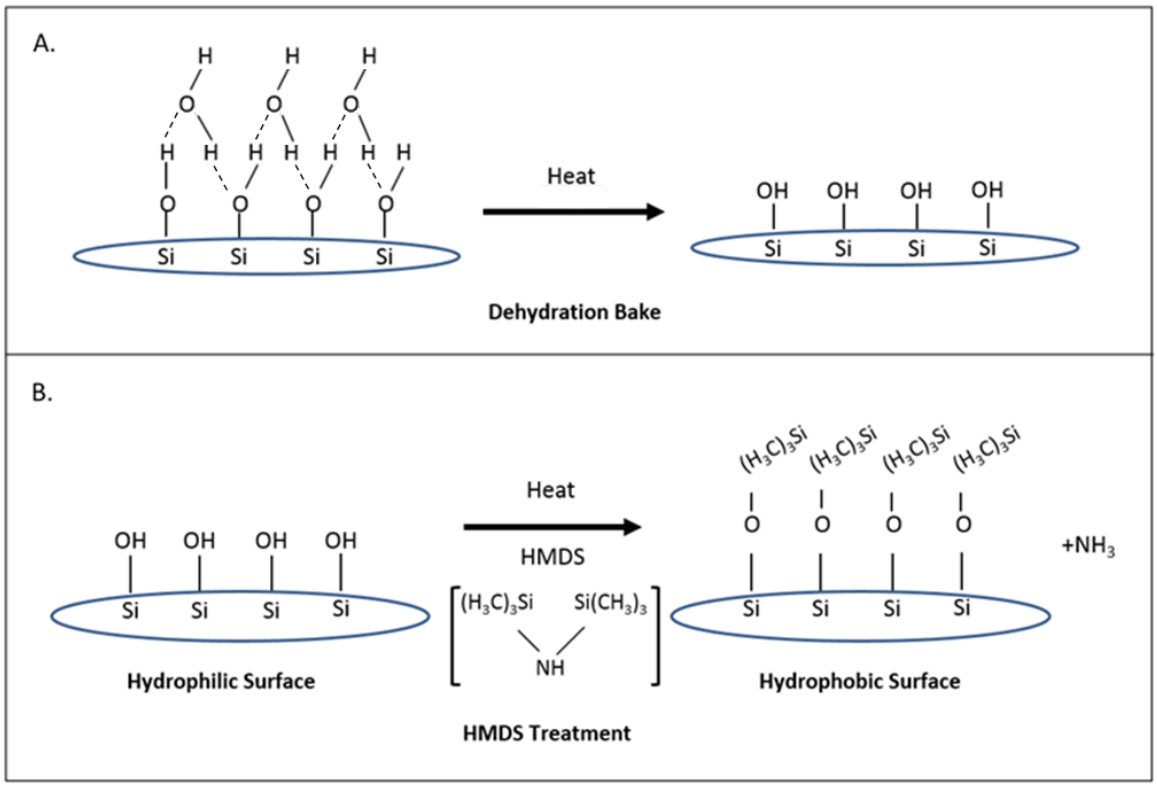

Figure 7: A) Surface chemistry of a silicon wafer before and after a dehydration bake. B) Surface chemistry of a silicon wafer before and after vapor deposition of HMDS. Modified from [54]. Covalent bonds and hydrogen bonds are presented as full and dotted lines, respectively.

Hydrophobic surfaces, such as HMDS treated wafers, tend to oppose the flow of water across their surfaces, causing droplets to "bead up". The degree to which this happens can be quantified by measuring the contact angle. This is the angle created by the intersection of the lines formed by the solid-liquid interface and the liquid-vapor interface. The latter line is taken to be the line tangent to the liquid-vapor interface that also runs through the point where all three phases are in contact as seen in Figure 8. Contact angles are also said to measure the wettability of a surface. A contact angle of zero occurs when the liquid fully spreads on the surface and creates a flat puddle. The greater the contact angle the more hydrophobic the surface is [53, 55, 56]. It should be noted that the liquid used to measure contact angles does influence the measurement. For HMDS pretreatment the contact angle obtained with water should be between 45° and 70°, with 60° being a commonly reported value [53]. It is possible to over prime the wafer, which would result in the PR rolling right off of the surface.

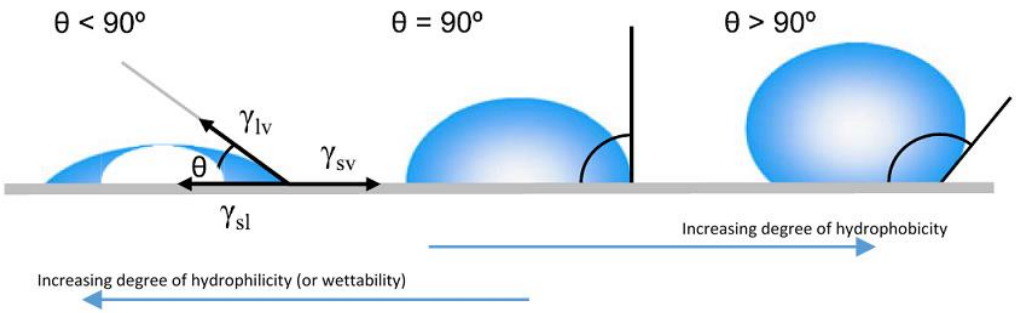

Figure 8: Illustration of contact angle measurement and indication of the degree of hydrophobicity or wettability of the surface. Reprinted with permission from [56].

2.1.2 Spin Coating

Spin coating is the standard in microfabrication for deposition of PR, as predictable and uniform film thicknesses can be achieved. Briefly, spin coating uses centrifugal force to spread the deposited PR over the wafer surface and to expel the excess PR from the wafer edge (Figure 9).

To begin the pretreated wafer is placed on the vacuum chuck of a spin coater, which holds the wafer in place during the spin coating process. It is important for film uniformity that the chuck is level and that the wafer is centered on the chuck. Likewise the PR should applied in the center of the wafer. As spin coating proceeds, the PR will spread across the wafer. To guarantee the wafer is entirely coated, it is therefore necessary to apply an excess of PR. Although it is not necessary to measure out the exact volume of PR to dispense, a common guideline for SU-8 formulations is one milliliter (mL) of PR per each inch of wafer diameter [57]. Once the PR is dispensed on the wafer, the wafer is rotated with the chuck in two steps. The first step is considered the spread step as it is responsible for coating the PR over the wafer and the second step is the spin step where the target spin rate is reached, dictating the PR film thickness. Both of these steps have a spin profile described by rotation speed, acceleration, and duration.

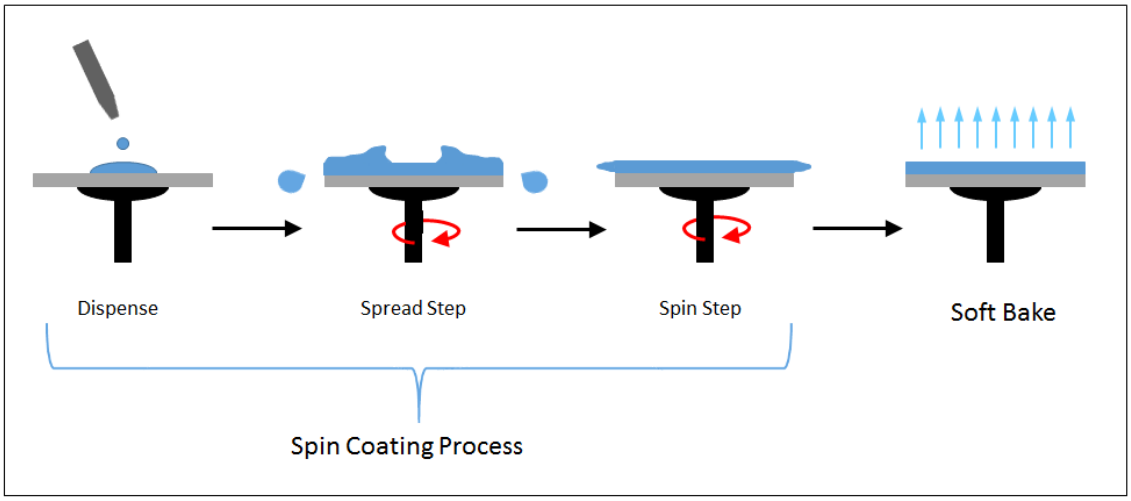

Figure 9: Schematic of the three steps in the spin coating process and subsequent soft bake step.

The rate at which the wafer is rotated in the spin step to obtain a target thickness depends on several factors including the intrinsic viscosity of the PR, the concentration of the polymer in the PR, and

an overall calibration constant. These variables are related to the final thickness, T, of the PR by the following equation:

$$T = \frac{KC^{\beta}\eta^{\gamma}}{\omega^{\alpha}}$$

Where K is the calibration constant; C is the polymer concentration in grams per 100 mL; η is the intrinsic viscosity; ω is the number of rotations per minute (rpm); and α, β, and γ are formulation specific exponents [22]. As these values are specific to individual (and often proprietary) formulations of PR, pre-calculated spin rates corresponding to desired film thicknesses are typically provided by the manufacturer in datasheets, greatly simplifying the spin speed determination.

The primary difference between the SU-8 formulations is the percentage of solvent and therefore the viscosity. When the ratio of solvent to polymer is increased, the viscosity of the PR decreases and the resulting formulation is able to produce thinner films. Additionally, as spin rate is increased, the resulting film thickness decreases (Figure 10) [57]. These relationships are also seen in Equation 1. Thickness, T, and rotation frequency, ω, are inversely proportional, while the polymer concentration, C, and molecular weight (represented by the intrinsic viscosity, η) are directly related to the thickness. The wide range of possible film thicknesses after one deposition of SU-8 PR (1 - 500 μm) is thus made possible both by the many formulations (i.e. viscosities) and by the spin speed. Finally, although the acceleration and duration of the spin profile can affect the film thickness, for simplicity in SU-8 datasheets for given formulations, these are kept constant and only the spin speed is changed to obtain a desired thickness. Optimization of spin speed to obtain a desired film thickness using a specific spin coater and resist available for master wafer construction is advised.

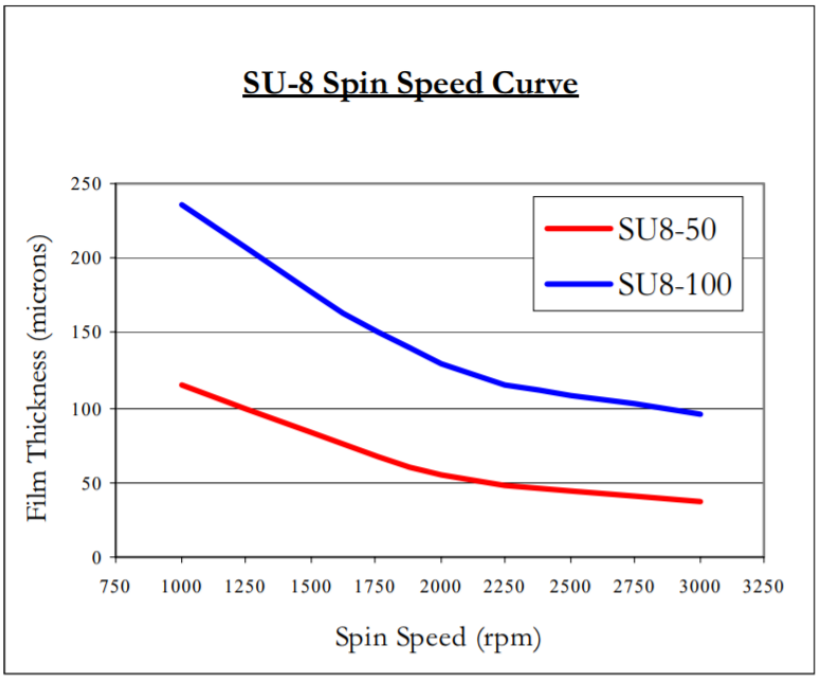

Figure 10: Film thickness (μm) vs. spin speed (rpm) for two SU-8 PR formulations given in the MicroChem datasheet [57]. For any formulation, a higher spin speed results in a decreased film thickness. Additionally, lower viscosity formulations (SU-8 50) are able to produce thinner films.

Soft Bake

Following the spin coating process, a soft bake (also called prebake) is performed to remove solvent and improve polymer adhesion to the substrate [22, 52]. The specific parameters of time and temperature used during the soft bake depend highly on the film thickness and PR formulation, parameters that can be found within tables provided in the same manufacturer supplied datasheets discussed above. For SU-8 PRs, the PR coated wafer is placed on a hot plate for a two-step baking process, typically 65 °C then 95 °C. Through the application of heat, solvent is driven out of the PR film and the film is able to relax into its most stable energetic state [22].

To remove the internal stresses of the PR and toughen the film, the PR coated wafer must be heated above the glass transition temperature, T_g, of the PR for a period of time and then allowed to cool to room temperature. When heated above T_g, the polymer experiences significant molecular motion of the polymer chain segments through viscous flow, promoting annealing of the film [22].

At the same time, solvent is driven out of the film. For reference, the T_g of SU-8 PRs is 55 °C. It should be noted, though, that overly high temperatures (> 120 °C for SU-8 PR) cause thermal activation of the photoinitiator that in turn reduces contrast and results in decreased resolution. Care must also be taken to not heat the wafer for too long as excessive baking can induce cracking [52]. Proper solvent removal prepares the film for the next step in photolithography: exposure.

2.1.3 Exposure

As stated previously, the process of photolithography uses light at specific wavelength to transfer a desired pattern onto a PR film for the purpose of creating microstructures on a substrate. In order to accurately reproduce a pattern on a substrate, many factors must be considered, such as: the energy in the wavelength of light, the duration of exposure and the region exposed.

Photomask

To control which regions of a PR coated substrate are exposed to light, an opaque (at the exposure wavelength) photomask is used. Corresponding to the two types of PRs, there are two variations of photomasks, called dark field and light field (Figure 11). Dark field masks, used with negative PRs, such as SU-8, consist of clear pattern regions and a dark background, or field. This allows exposure light to reach the PR only in the regions that will create the desired pattern, and not in the background. Light field masks are used with positive PRs and are exactly opposite in polarity, with opaque pattern regions and a clear background (field). In the case of light field masks, the exposure light reaches the background but not the pattern features. Two commonly used photomasks are chrome-coated glass masks and transparency films made with high-resolution printing. For the purposes of soft lithography, transparency films are more commonly used because they are less expensive and have a more rapid turnaround from design to production. Chrome

masks are significantly more expensive but they are more robust and can achieve better resolutions, down to 1 μm or less [29].

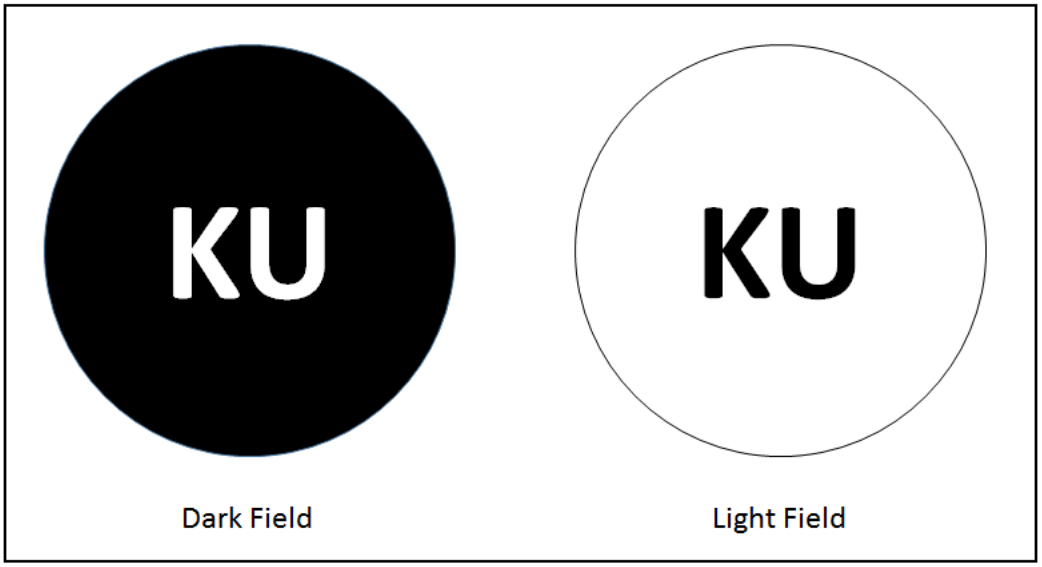

Figure 11: Example of a dark field mask (left) used with negative resist and a light field mask (right) used with positive resist that would result in raised features of the letters K and U.

Exposure

The exposure process is the mechanism by which the pattern is transferred into the PR layer (Figure 12). For SU-8 this transfer begins when UV light activates the photoinitiator and polymer cross-linking begins. Practically speaking, the application of UV light to a PR coated substrate is typically performed using a broad band mercury lamp which produces several wavelengths of light. Optical filters can be used to block undesirable wavelengths, typically leaving i-line (365nm) for exposure, as i-line is compatible with both AZ series positive photoresists and SU-8 series negative resists.

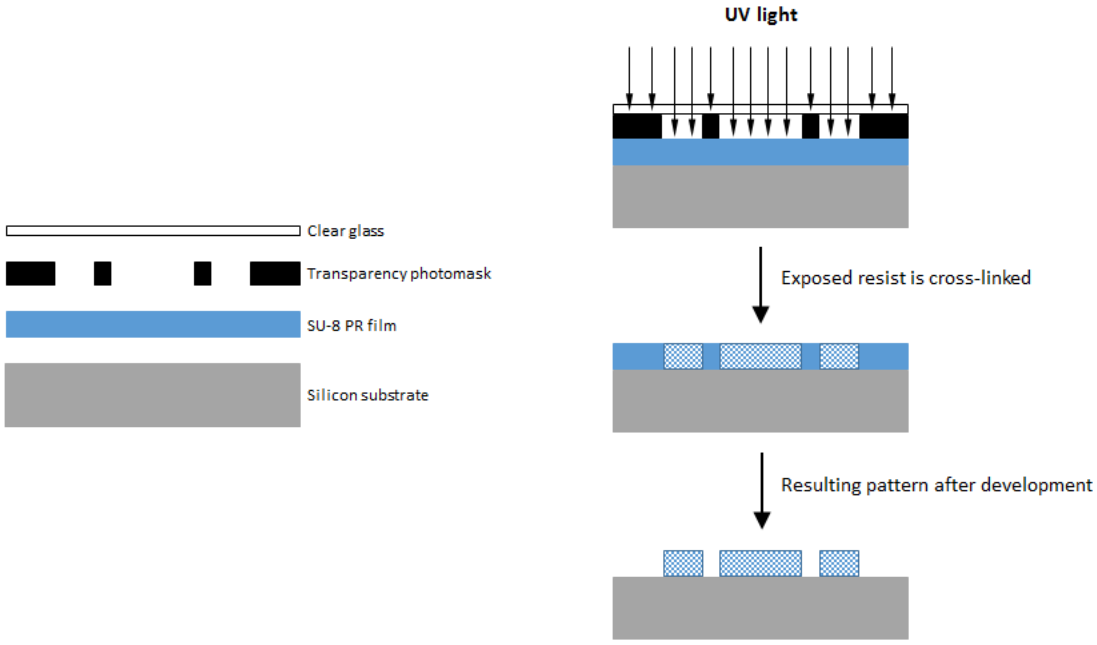

Figure 12: Schematic of SU-8 (negative) PR exposure and resulting pattern.

The exposure energy dose required to transfer a pattern onto a PR coated wafer is a function of the thickness as seen in Figure 13, given in the MicroChem datasheet for SU-8 50-100 [57]. Higher doses are needed for thicker films to fully polymerize as the energy dose attenuates as it moves down into the film. The datasheet provides two curves that indicate a maximum and minimum suggested exposure dose for a given thickness. From these curves a maximum and minimum exposure time can be obtained. To determine the exposure time, t, in seconds, the energy dose obtained from the datasheet must be divided by the light intensity (LI) of the specific UV source used.

$$t = \frac{Dose}{LI}$$

Where Dose is the exposure energy in mJ/cm^2 and LI is the light intensity in mW/cm^2.

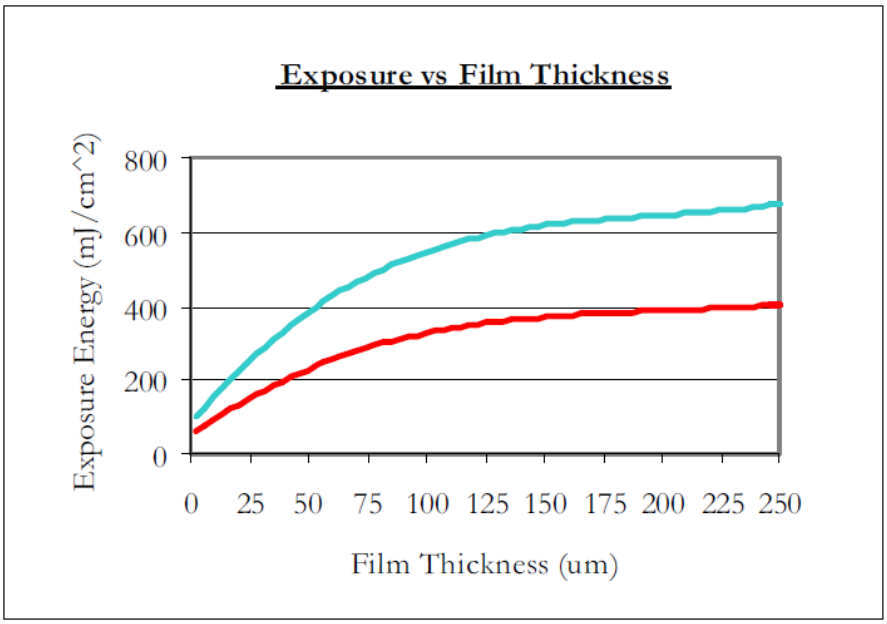

Figure 13: Exposure Energy (mJ/cm^2) vs. film thickness (μm) for SU-8 given in the MicroChem datasheet for SU-8 50-100 [57]. The teal line indicates the maximum suggested energy dose and red, the minimum for a given thickness. As film thickness increases, a higher energy dose is needed to initiate polymerization throughout the entire film thickness.

An optimal exposure time will result in the full polymerization of the PR in the desired region after the post exposure bake. In the event that the PR film is underexposed (too small a dose for a given thickness of PR), the region of polymerization will not extend all the way down to the underlying substrate. The result will be "lift off" of the PR during development as the PR will not have cross-linked to the substrate. In contrast, a PR film can also be overexposed. This can happen when shorter wavelengths of light are insufficiently blocked by the filtering optics or when the dose is too high. The result can be an exposed surface, like a crust, with a region below the surface that is underexposed. This phenomena is known as T-topping, due to the profile created in the features. Overexposure can result in an over production of the hexafluoroantimonic acid. This excess of acid can then diffuse outside of the exposed areas, cross-linking regions outside of the desired pattern, and decreasing the overall resolution. For each new process, it is typically necessary to optimize the exposure time to result in the best pattern transfer.

Post Exposure Bake

The post exposure bake (PEB) is a critical step in SU-8 photolithography because the polymerization process, first activated by the acid formed when the photoinitiator is exposed to a UV lightsource, is further catalyzed by increased temperatures. A proper PEB with lower temperatures and longer times will ensure fully cross-linked structures and mold robustness [52]. MicroChem's SU-8 datasheets recommend, like the soft bake, a two-step PEB to reduce internal stresses caused by rapid temperature changes. The recommended temperatures are again 65 °C and 95 °C, and the baking times based on the film thickness can be found within tables provided in the datasheets [57].

2.1.5 Development

During development, the regions of unpolymerized SU-8 that remain after the PEB are preferentially dissolved by the developing solution, which is why PEB times are important. An optimized PEB will ensure fully polymerized features that will not be affected during development. Although the polymerized SU-8 is still susceptible to the developing solution, the dissolution rate is significantly slower due to the variation in molecular weight between the polymerized and unpolymerized regions. The development step takes advantage of the different dissolution rates to preferentially dissolve the unexposed regions of PR and leave the exposed regions, where cross-linking has occurred, behind as relief microstructures. The PR coated wafer is immersed in the developer and gently agitated. Thicker films require longer development times to remove all of the unpolymerized SU-8 PR. The organic developer used for SU-8 is called SU-8 developer and can be purchased from MicroChem. The MicroChem datasheets provide tables with development times for given thicknesses. The wafer is removed from the developer, rinsed with isopropyl alcohol (IPA) and dried using compressed nitrogen gas.

Hard Bake

A hard bake, while not absolutely required, is often performed to drive out any additional solvent residue from both the SU-8 relief microstructures and the wafer itself, further annealing the structures onto the wafer. This annealing is recommended to counteract developer penetration at the resist-wafer interface or swelling of the resist caused by the developer [22, 52] and is especially beneficial for the purposes soft lithography where the resist structures remain as part of the final mold. MicroChem datasheets recommend hard baking at 150 °C to 200 °C with slow ramping [57]. Times greater than 20 minutes are typical [22] and the Adams Microfabrication Facility recommends a hard bake of an hour or more.

2.2 PDMS Casting and Bonding for Device Fabrication and Assembling

2.2.1 Casting

The photolithography process described thus far has detailed the fabrication of master molds, which can be used repeatedly to create microfluidic devices through elastomeric casting. Repeated casting with an elastomer has enabled inexpensive prototyping and mass production of microfluidic devices. Soft lithography applications are broad and diverse in both their methods and their resulting microdevices, but they are all characterized by the use of an elastomer, hence the name *soft* lithography. For the purposes of creating microfluidic devices, such as organ-on-chip devices, soft lithography begins where photolithography ends: with a master mold containing a relief pattern. An elastomer is poured onto the master mold, cured and removed from the mold, transferring an inverse of the mold's relief pattern into the solidified elastomer. This elastomer layer can then be bonded to glass or to other elastomer layers, thereby completing the fabrication of a microfluidic device (Figure 14).

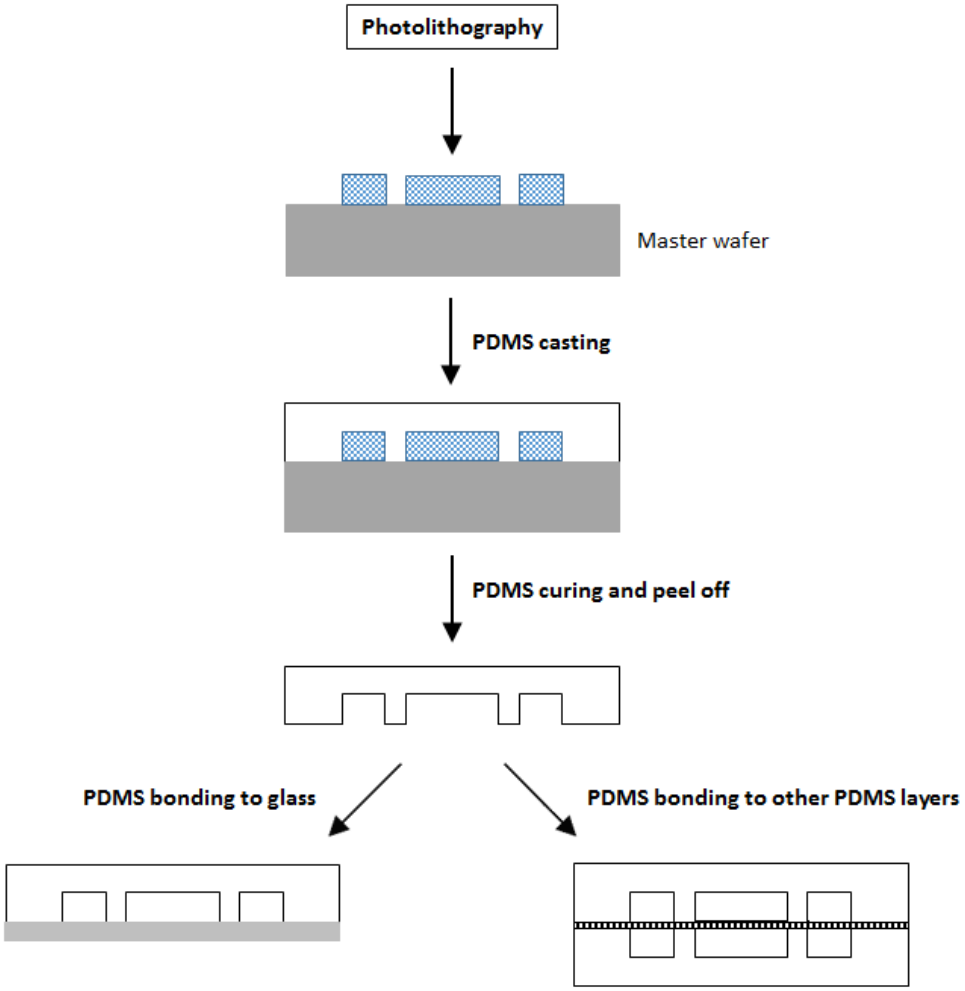

Figure 14: Schematic of soft lithography using PDMS elastomer to create microfluidic devices.

Polydimethylsiloxane (PDMS) is the elastomer of choice for most soft lithography applications, especially for organ-on-chip devices, as it is optically clear, flexible, gas permeable, and bonds well with glass and other PDMS layers. PDMS is supplied as a two part system: a base and a curing agent. The liquid parts must be mixed to initiate the polymerization. The cross-linking reaction (Figure 15) is catalyzed by a proprietary platinum based catalyst contained in the curing agent and is accelerated with heat. The ratio of PDMS base to curing agent determines the hardness of the cross-linked polymer and can be manipulated depending on the application.

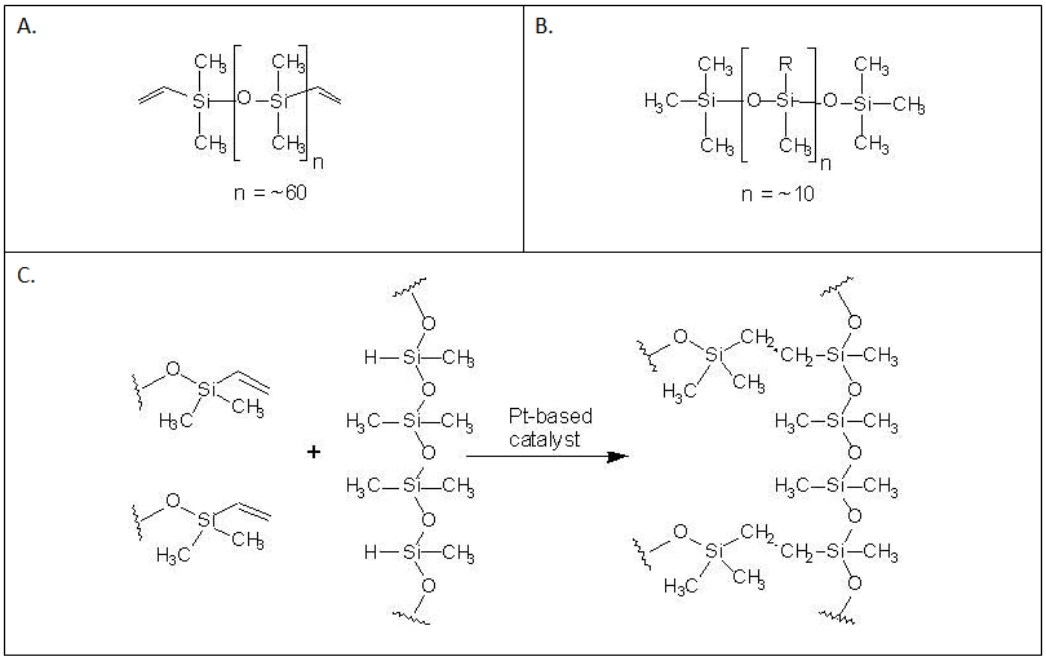

Figure 15: A) Siloxane oligomer of the PDMS base. B) Siloxane cross-linker of the PDMS curing agent. C) PDMS cross-linking reaction. Modified from [58].

As the master wafer molds need to be used repeatedly, release agents are used to facilitate removal of the cured PDMS layer from the silicon master wafer to prevent damage of the relief features and extend the life of the mold. Hexamethyldisilazane (HMDS) or trichloro(1H,1H,2H,2H-perfluorooctyl)silane (PFOTS) are vapor deposited onto the master wafer, a process referred to a silanization, for the purpose of creating a hydrophobic monolayer that resists adhesion of the PMDS to the silicon master wafer [59, 60].

Following the application of the release agent, the mixed and degassed PDMS is applied in a liquid form and cured. The solidified polymer can then be peeled off, resulting in a transfer of the relief patterns of the master mold to the PDMS as hollow channels.

2.2.2 Bonding

An important technique, and often the final step, in the creation of microfluidic devices is the bonding of the PDMS layer(s) to glass or other PDMS layers for the purpose of creating fully

enclosed channels. PDMS has become ubiquitous in microfluidic applications for several reasons, but a significant reason is its ability to bond well both to glass and to other PDMS layers. This property has enabled the construction of complex, multi-layered devices. The generalized process of bonding involves the creation of hydroxyl groups at the surface of both substrates using the application of oxygen or air plasma followed by a thermal assist to induce the formation of covalent bonds between the substrates. The plasma oxidation of PDMS and glass substrates results in charged surfaces that are energetically favorable to bonding. When PDMS is exposed to an oxygen plasma the methyl functional groups are replaced by hydroxyl groups resulting in a silanol surface. When glass is exposed to oxygen plasma the silicon dioxide surface also forms silanol groups. When two oxidized surfaces (whether glass-PDMS or PDMS-PDMS) are brought into contact, silicon-oxygen-silicon (Si-O-Si) bonds are formed at the interface of the two surfaces, irreversibly bonding the two substrates. The two surfaces should be brought into contact as soon as possible after plasma oxidation, as the hydrophilic surfaces quickly recover their hydrophobic properties and lose their ability to bond.

3. Experimental Methods to Fabricate a Lung-on-chip Device

3.1 Materials

To create the lung-on-chip device, SU-8 50 negative photoresist (PR) (MicroChem, Westborough, MA) was used along with SU-8 developer (MicroChem, Westborough, MA) and isopropyl alcohol (IPA) (Fischer Scientific, Waltham, MA) to create the master wafer molds that in turn create the top and bottom polymer layers needed for device construction. SU-8 10 negative PR (MicroChem, Westborough, MA) was used also with SU-8 developer and IPA to create the master wafer mold used in creating the porous membrane (PM) layer. Clean, 4-inch diameter silicon wafers (University Wafer, South Boston, MA) were used as the substrates for SU-8 spin coating and photolithography. Photomasks were designed using AutoCAD 2014 (Autodesk, San Rafael, CA) and subsequently printed at high resolution, 40,000 dots per inch, on transparent photofilm (Infinite Graphics, Minneapolis, MN). Polydimethylsiloxane (PDMS) and the corresponding curing agent (Dow Corning Corporation, Midland, MI) were used to create PDMS casts of the master wafer molds. Hexamethyldisilazane (HMDS) (Acros Organics, New Jersey, USA) or trichloro(1H,1H,2H,2H-perfluorooctyl)silane (PFOTS) (Sigma Aldrich, St. Louis, MO) was used to coat the master wafer molds prior to PDMS casting or to coat the PDMS slab used to create the PM layer.

3.2 Microfabrication of the Lung-on-chip Device

Fabrication of the multilayer PDMS lung-on-chip device followed five broad steps: **(1)** Fabrication of the master wafers by coating silicon wafers with SU-8 PR and performing standard photolithography procedures which are introduced in Chapter 2; **(2)** Creation of the top and bottom layers of the device by PDMS casting; **(3)** Creation of the porous membrane (PM); **(4)** Opening of

the middle channel of the top layer; and **(5)** Assembling the three layers with plasma oxidation and careful alignment.

3.2.1 Fabrication of the Master Wafers by Photolithography

The master wafers for the top and bottom layers of the lung on chip device were created by following this procedure only differing in the photomask used during photolithography, thereby creating different features out of the SU-8 PR for the respective layers. When creating a master wafer, a new 4-inch silicon wafer was prebaked at 200 °C for a minimum of 2 hours to completely desiccate the wafer's surface, ensuring optimal adhesion of the SU-8 photoresist. Previously used wafers could be reused by removing the PR features with a razor blade and cleaning with acid piranha followed by base piranha. However, for this work new wafers were used. While the wafer baked, approximately 10 mL of SU-8 50 PR was poured into the Handy Step® S repeating pipette (Fischer Scientific, Waltham, MA). An important step prior to dispensing the PR was to remove trapped air bubbles from the viscous PR. Air bubbles cause an unwanted decrease the dispensed volume of PR, but more importantly, they can disrupt features if they remain on the film as bubbles or as defects when the spin coating is completed. The loaded syringe was left, tip up, shielded from the ambient light by a foil cover while the bubbles made their way into the syringe tip. The bubbles were ejected from the syringe tip, sacrificing a few milliliters of PR to ensure the remainder was as bubble free as possible.

As soon as the wafer returned to room temperature from the prebake, the wafer was placed and centered on the chuck of the spin coater (Brewer Science, Inc., Model 100, Rolla, MO), using a 3D printed tool seen in Figure 16, and a vacuum was applied. Centeredness was checked visually at low speeds. This process may also be accomplished by hand, but the tool makes the process considerably faster and easier. The repeating pipette was set to dispense 4 mL of PR, as 1 mL of

PR per inch of wafer diameter is recommended for the spin settings. The PR was applied to the center of the wafer. Any bubbles remaining in the PR were popped using a 27 ½ gauge needle. The wafer was first ramped at 100 rpm s^{-1} to 500 rpm and run for 15 seconds to spread the PR. Then the wafer was ramped at 300 rpm s^{-1} to 1300 rpm and run for 30 seconds to produce a 100 μm thick layer of PR on the wafer. The wafer was removed from the chuck and placed on a hot plate initially at room temperature. The hot plate was brought up to 65 °C, then the wafer was soft baked for 10 minutes. For the second step of the soft bake, the hot plate was brought to 95 °C. Once the hot plate reached 95 °C, the wafer was baked for 30 minutes, and then the hot plate was turned off. The wafer was allowed to cool to room temperature on the hot plate.

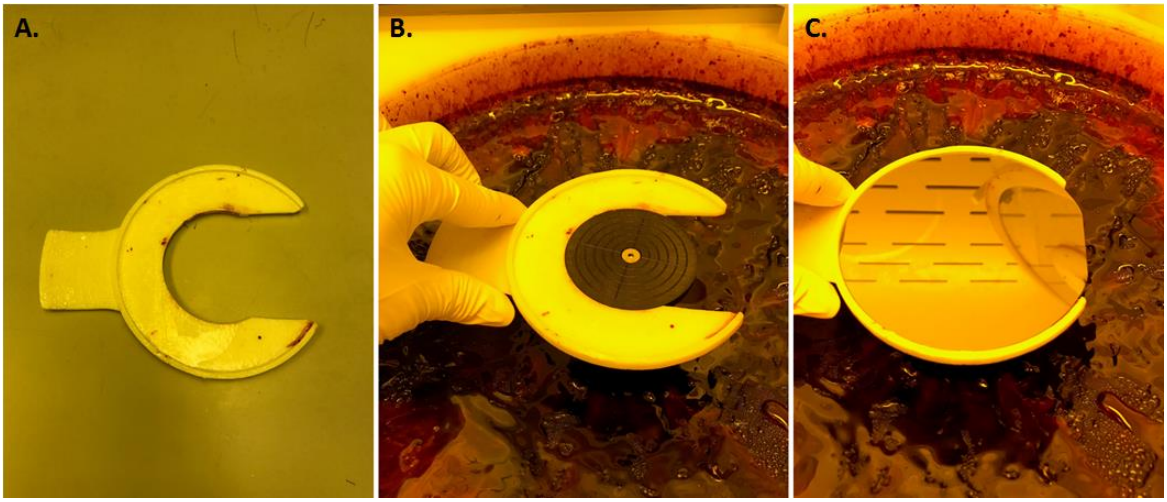

Figure 16: A) The 3D printed centering tool. B) The centering tool on the vacuum chuck of the spin coater. C) A silicon wafer centered on the vacuum chuck with the aid of the centering tool.

After the soft bake, the mask aligner (ABM Inc., ABM Flood Source, San Jose, CA) was used to perform UV lithography. The mask aligner was turned on 10 minutes prior to use to allow the UV lamp to warm up. The exposure dose used was 567 mJ/cm^2. Once the wafer was placed on the substrate chuck of the mask aligner, the photomask of the top layer of the lung on chip device was placed, ink-side down, onto the PR coated wafer. The photomask was placed such that any features of the device were not placed on regions containing bubble defects. A glass mask was placed on

top of the photomask and brought into tight contact with the photomask and the PR coated wafer. Observation of newton rings indicated close contact. The substrate was exposed for 27 seconds, calculated from the exposure dose needed for a 100 μm film thickness and the light intensity of the UV lamp, 21 mW/cm^2. After UV exposure, the wafer underwent a post exposure bake. The wafer was placed on a room temperature hot plate. The hot plate was brought to up to 65 °C. After the wafer baked for 5 minutes at 65 °C, the hot plate temperature was raised to 95 °C, and the wafer was baked for 20 minutes. The hot plate was turned off, and the wafer was allowed to cool to room temperature. SU-8 developer was used to remove the unexposed PR. The developer was poured into a Pyrex dish and the wafer was placed in the dish, submerged in the developer. The dish was agitated by hand for 10 minutes. Once removed from the developer, the wafer was rinsed with IPA to ensure that all the unexposed PR was washed away by the developer. If a milky residue appeared during rinse, the wafer was placed back into the developer for an additional 30 seconds. The wafer was then removed and again rinsed with IPA. This process was repeated until the IPA rinse produced no milky residue. Compressed nitrogen gas was used to dry the wafer. The dry wafer was placed on a room temperature hot plate which was ramped to 200 °C for a hard bake. The wafer was baked for 2 hours. This process was repeated exactly to create the bottom layer master wafer, except that the photomask containing the pattern of the bottom layer was used instead.

Once the master wafers of the top and bottom layers of the lung-on-chip were made, the master wafer that is used to make the PM layer was made. The same general procedure described for fabricating the top and bottom master wafers was used; however, the parameters were modified to create 25 μm features on the wafer instead of 100 μm features. The wafer was still prebaked for 2 hours at 200 °C; however, SU-8 10, a less viscous PR, was used in the coating process rather than

SU-8 50. Coating of the wafer was achieved with a similar initial step used to spread the PR (ramped at 100 rpm s^{-1} to 500 rpm and run for 5 seconds). The second step of coating was coincidentally the exact same as the second step for creating 100 μm features with SU-8 50. After the initial spread step the wafer was ramped at 300 rpm s^{-1} to 1300 rpm and run for 30 seconds to produce a 25 μm thick layer of PR on the wafer. The durations of the soft bake, UV exposure, post exposure bake, and development step were less than those used in the process to make the 100 μm feature wafers. The wafer was soft baked at 65 °C for 2 minutes and 95 °C for 6 minutes. The UV exposure time was 18 seconds, based on an exposure dose of 378 mJ/cm^2. For the post exposure bake, the wafer baked at 65 °C and 95 °C for 1 and 2 minutes, respectively. In the development step, the wafer was agitated in the developer for 4 minutes. An IPA rinse was still used to verify that all the unexposed PR was removed. The final hard bake was the same as before: 200 °C for 2 hours.

The three separate master wafers created using the methods described above are used repeatedly to create the individual PDMS layers of lung-on-chip devices as described in the next steps. A summary of these parameters can be found in Table 1 which contains the recommended parameters optimized by the Adams Microfabrication Facility for the fabrication of master wafers. However, as discussed in Chapter 4, the outcomes were subject to day-to-day variability.

Master Wafer	Feature Height (μm)	PR	Spread Step			Spin Step			Soft Bake (min)		Exposure		Post Exposure Bake (min)		Development (min)
			Speed (rpm)	Acceleration (rpm/s)	Duration (s)	Speed (rpm)	Acceleration (rpm/s)	Duration (s)	65 °C	95 °C	Dose (mJ/cm^2)	Time (s)	65 °C	95 °C	
Top	100	SU-8 50	500	100	15	1300	300	60	10	30	567	27	5	20	10
Bottom	100	SU-8 50	500	100	15	1300	300	60	10	30	567	27	5	20	10
Porous Membrane	25	SU-8 10	500	100	5	1300	300	60	2	6	378	18	1	2	4

Table 1: Photolithograpy parameters for microfabrication of the three master wafers needed to create the lung-on-chip device. Exposure times are based on a light intensity of 21 mW/cm^2.

The results of the photolithography process were verified using a profilometer and optical microscopy. The master wafers were used indefinitely until the PR features pulled away from the silica wafer or even broke off, at which point new master wafers were fabricated.

3.2.2 Fabrication of the Top and Bottom Layers by PDMS Casting

The top and bottom layers of the lung-on-chip device were made by PDMS casting of the respective master wafer. PDMS casting consists of wafer pretreatment, mixing of the elastomer and curing agent, degassing the mixture, pouring the mixture on the wafer, curing the PDMS, and removal of the PDMS from the master wafer.

The master wafers were first silanized with either hexamethyldisilazane (HMDS) or trichloro(1H,1H,2H,2H-perfluorooctyl)silane (PFOTS) to allow for easy removal of the cured PDMS from the master wafer. Silanization of the wafer by vapor deposition was performed under a fume hood with a vacuum desiccator (Bel-Art, Model F42400-2141, Wayne, NJ). A master wafer and a glass microscope slide were placed inside the vacuum desiccator. If HMDS was used, a quarter-sized amount was dispensed onto the glass slide using a glass syringe. If PFOTS was used, a single droplet was dispensed onto the glass slide using a disposable transfer pipette. The lid to the desiccator was put in place, the chamber's valve was opened to the vacuum pump, an d the pump was turned on to establish a vacuum inside the chamber. Once a vacuum of at least -0.08 Megapascals (MPa) was established, the valve was closed to seal the chamber and maintain the vacuum. The pump was then turned off. The wafer was left under vacuum overnight or for minimum of 8 hours to complete pretreatment by silanization.

The PDMS elastomer and curing agent were weighed out, at the desired mass ratio, into a plastic cup on a tared scale. A glass stirring rod was used to vigorously stir the two components until they

were well mixed and the mixture was white and frothy. The cup was placed into a glass vacuum chamber, and a vacuum pump was used to pull a vacuum. The vacuum was held until the air bubbles in the mixture rose up almost to the top of the cup, at which point the vacuum was released. This cycle was repeated until the bubbles no longer rose when the vacuum was reapplied. At this point the vacuum was maintained for an additional 10 minutes to fully degas the PDMS mixture. The pump was turned off and the degassed mixture was removed from the chamber. After degassing, the mixture was clear with no bubbles. This degassed mixture was then poured over a pretreated master wafer. If more than 12 g of the mixture was poured onto the wafer, a foil boat was used to prevent the mixture from running off the edges. In this manner a thicker PDMS device layer could be made. When the mixture reached the edges of the wafer, it was placed on a leveled rack in an oven to cure for a minimum of 5 hours at 70 °C. After curing, the wafer was removed from the oven and allowed to cool to room temperature. A razor blade was used to separate the cured PDMS from the edge of the master wafer and the cured PDMS was slowly and carefully peeled off of the wafer.

For this work the PDMS monomer and curing agent were mixed at a mass ratio of 10:1 or 15:1 (PDMS monomer to cross-linking agent) depending on the study, and the total mass of the mixture also varied. During evaluations of the casting method, the top and bottom layers were made with a 12 grams (g) of the PDMS mixture, at a 10:1 mass ratio. During evaluations of the stamp method, the bottom layer was made with 40 g of the PDMS mixture, and the top layer was made with 12 g of the PDMS mixture, both with a 15:1 mass ratio. The thick and thin top layers used for laser ablation evaluations were made with 5 g and 12 g of PDMS mixture (10:1 ratio), respectively. Finally, for CNC milling the top layers were made from 12 g of PDMS at a 10:1 ratio.

3.2.3 Fabrication of the PDMS Porous Membrane Layer

Casting Method

The first method tested to microfabricate the 10 μm thick PM layer consisted of a casting method, using a spin coater to spread the PDMS over the PM master wafer, because pouring a 10 μm thick layer by hand is not possible. A schematic of this casting method can be seen in Figure 17 and the steps are described in detail below.

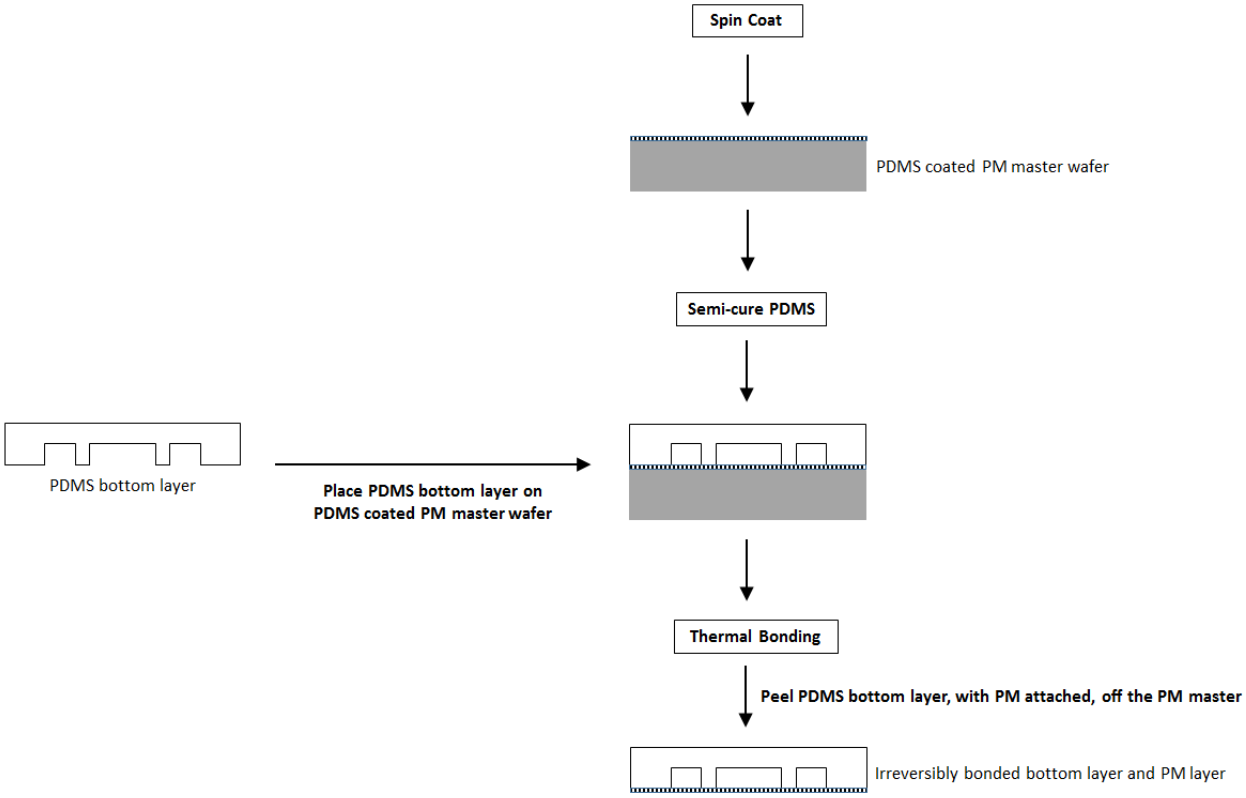

Figure 17: Schematic, shown as a cross-sectional view, of the casting method used to create the porous membrane layer that results in a PM layer irreversibly bonded the PDMS bottom layer.

The PM master wafer was first pretreated with HMDS in a vacuum desiccator, following the same protocol detailed above in section 3.2.2. After overnight silanization, 12 grams of a 10:1 (base: curing agent) PDMS mixture was made, also following the protocol described above. The treated

master wafer was placed, centered on the chuck of the spin coater and a vacuum was applied. A volume of 4 mL of the PDMS mixture was dispensed onto the master wafer, using the repeating pipette. The PDMS was first spread over the treated wafer by ramping at 100 rpm s^{-1} to 500 rpm and held for a duration of 5 seconds. Several variations of the second spin step were performed. For this step, rotation rates between 3300 rpm and 5000 rpm were tested, but the acceleration and duration were held constant at 300 rpm s^{-1} and 30 seconds, respectively. Another variation of the spin step was a long duration and low spin speed. In this case, a spin rate of 2500 rpm, an acceleration of 300 rpm s^{-1} and a duration of 10 minutes were used. The PDMS layer on the master wafer was semi-cured by incubating at 70 °C for a short time so that the PDMS was still tacky. Semi-curing tests were performed at a range of 7 to 14 minutes. After semi-curing, the wafer was removed from the oven and a PDMS bottom layer (produced in the previous section) was immediately lowered onto the semi-cured PM layer, channel side down. This assembly was returned to the oven and left overnight for the PM layer to finish curing and permanently bond to the bottom layer through thermal bonding. The following morning, a razor was run along the edge of the wafer to help release the PM layer from the wafer. Finally, the PDMS bottom layer, with the PM layer attached, was carefully peeled away from the PM master wafer.

Stamp Method

The second method used to create the PM layer followed the protocol by Dongeun Huh et al. [32]. This process was not a casting process. Rather, the microfabricated posts of the PM master wafer were used to stamp the through-holes into an uncured PDMS layer. The process consisted of spin coating a film of uncured PDMS onto a silanized slab of fully cured PDMS, inverting the film (on the PDMS slab) over the microfabricated posts of the silanized PM master wafer, and placing the film onto the posts. A glass slide and an iron weight were then placed on the PDMS slab in order

to ensure that the posts pierced the uncured PDMS film, thereby creating through-holes. After curing, the PDMS slab and film (now containing through-holes) were removed from PM master wafer. A schematic of this process can be seen in Figure 18 and a detailed explanation is described below. To remove the PM film from the sacrificial PDMS slab, the PM was irreversibly bonded to the PDMS bottom layer of the lung-on-chip device, transferring the PM from the slab.

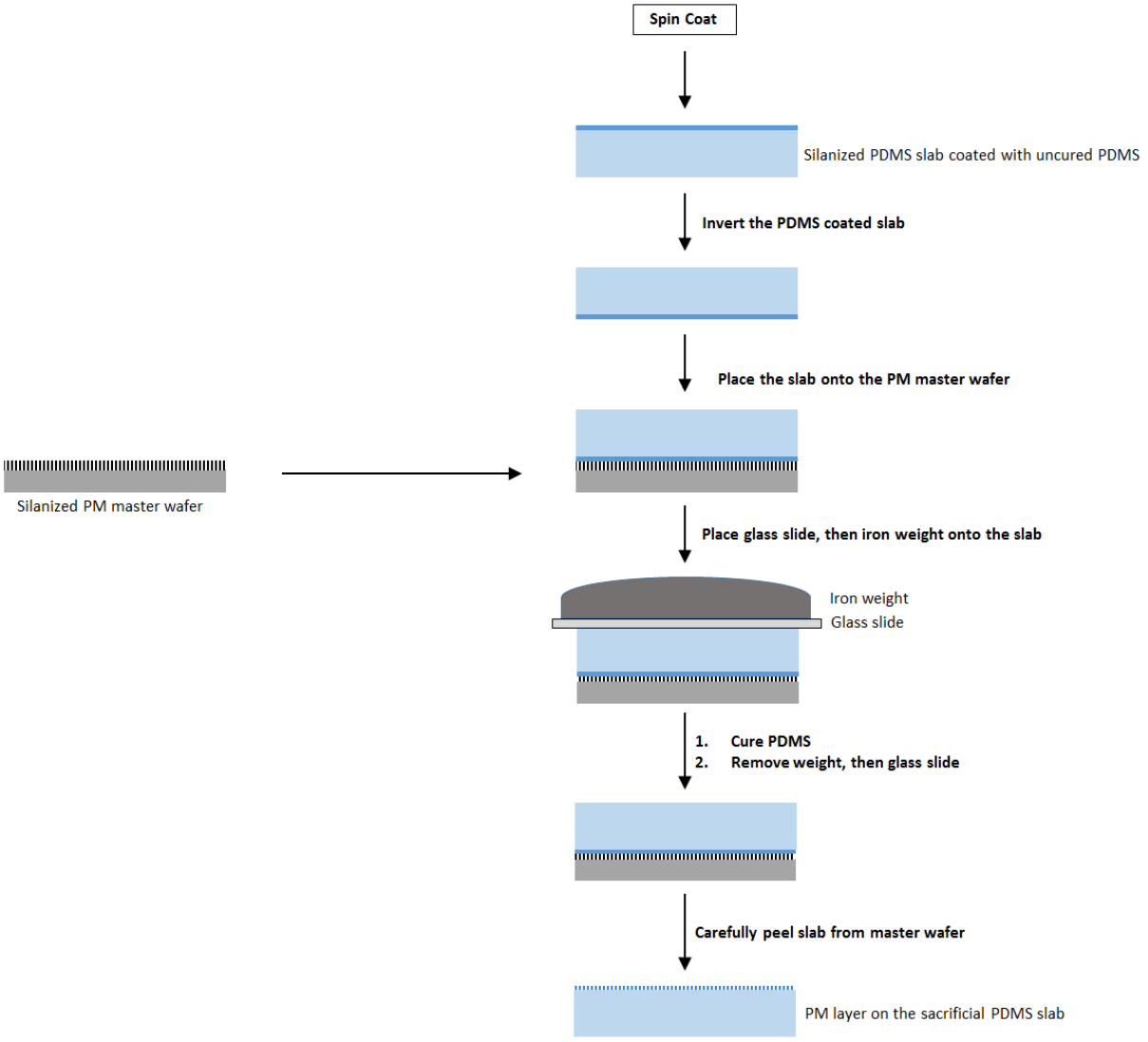

Figure 18: Schematic, shown as a cross-sectional view, of the stamp method used to create the porous membrane layer that results in a PM layer on a sacrificial slab on PDMS. In this method a weight is used to ensure that the posts of the PM master wafer pierce the film of uncured PDMS.

For the stamp method, PDMS base and curing agent (40 g total) were mixed at a 15:1 mass ratio and the mixture was degassed following the same protocol detailed in section 3.2.2. The degassed PDMS was poured onto a clean, featureless 4-inch silicon wafer resting in a foil boat to create an approximately 5 mm thick PDMS slab. The PDMS layer was cut away from the wafer by running a razor blade along the edge of the wafer and was subsequently cut into four 2.5 cm x 4 cm rectangular slabs. The corners of the slabs were cut away at 45° angles. This facilitated bonding by removing the uneven edges created when cutting PDMS by dragging a razor through it. One of the PDMS slabs was cleaned of dust particles by applying scotch tape and peeling the tape away. The remaining slabs were wrapped in tape and stored for future use.

The slab was placed on a glass microscope slide which was then placed in the vacuum desiccator used for silanization. The slab was pretreated with either HMDS or PFOTS to facilitate the removal of the PM layer from the PDMS slab. This pretreatment followed the same guidelines described in step section 3.2.2. A quarter sized amount of HMDS was used or a droplet sized amount of PFOTS was used. A vacuum of at least -0.08 MPa was applied to the chamber, and the PDMS slab was left overnight for a minimum of 8 hours for silanization. The PM master wafer was also pretreated with HMDS or PFOTS following the same guidelines.

PDMS monomer and curing agent were mixed a 10:1 mass ratio totaling 5 g and degassed, following the same protocol described previously. The treated silanized slab was cleaned of dust particles with compressed nitrogen gas. The slab on the glass slide was placed in a custom, 3D printed slide holder onto the chuck of the spin coater (Figure 19). The 10:1 PDMS mixture was then poured onto the center of the silanized PDMS slab making circular pool of PDMS, filling the width of the slab. The PDMS was allowed to self-spread on the slab for 10 minutes. The spin coater was then ramped at 100 rpm s^{-1} to 500 rpm and held for 20 seconds to evenly spread the

mixture over the entire PDMS slab. To create a 10 μm thick layer of PDMS on the slab, the spin coater was then ramped at 160 rpm s^{-1} to 2,400 and held for 10 minutes. The uncured PDMS layer on the PDMS slab was left to rest for 3 minutes on the vacuum chuck before the silanized slab was peeled away from the glass slide. Care was taken to minimize bending of the slab and the layer of uncured PDMS on it. The slab was inverted, putting the PDMS-coated side face down, ready to be lowered onto the PM master wafer. The film side of the slab was placed onto the microfabricated posts and a glass slide was placed on the slab with light pressure and weighted with a 300-400 g iron weight. The weighted slab and film was left overnight or for a minimum of 8 hours on a level shelf.

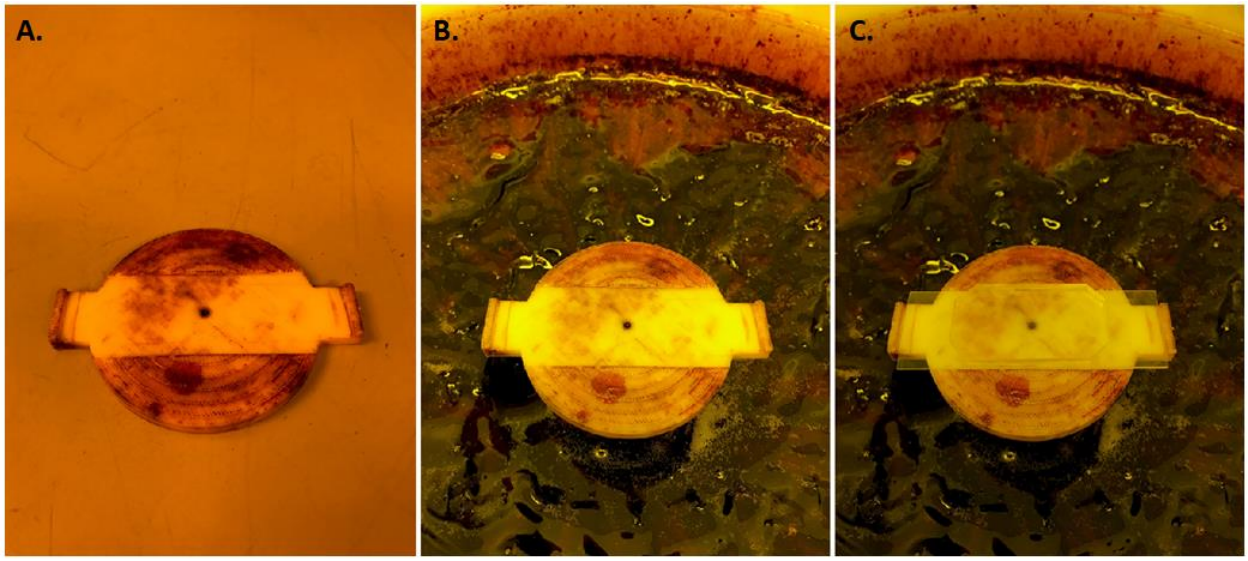

Figure 19: A) The 3D printed slide holder. B) The slide holder fitted on the vacuum chuck of the spin coater. C) A PDMS slab on a glass slide fixed to the vacuum chuck using the slide holder. In the stamp method for creating the porous membrane, a thin film of PDMS is spin coated onto the PDMS slab before the microfabricated posts of the PM master wafer are pressed, or stamped into the film.

After overnight curing, this assembly was placed in an oven for one hour at 70 °C to finish curing. Once the assembly was removed from the oven and allowed to cool to room temperature, the weight and glass slide were removed from the PDMS slab. Finally, the slab with the attached PM

layer was slowly and carefully peeled away from the posts of the master wafer. Through the methods described here, the PM layer (still attached to the PDMS slab) was fabricated. The bonding step which transfers the PM layer from the slab to the PDMS bottom layer is described in section 3.2.5.

3.2.4 Methods Evaluated for Opening the Middle Channel of the Top Layer

A goal of this thesis was to open the middle channel of the top layer of the lung-on-chip device to allow for an air-liquid interface during lung-on-chip surfactant experiments. A schematic, drawn as cross-sectional view, demonstrating the creation of an open middle channel which would allow for an air-liquid interface is shown below (Figure 20).

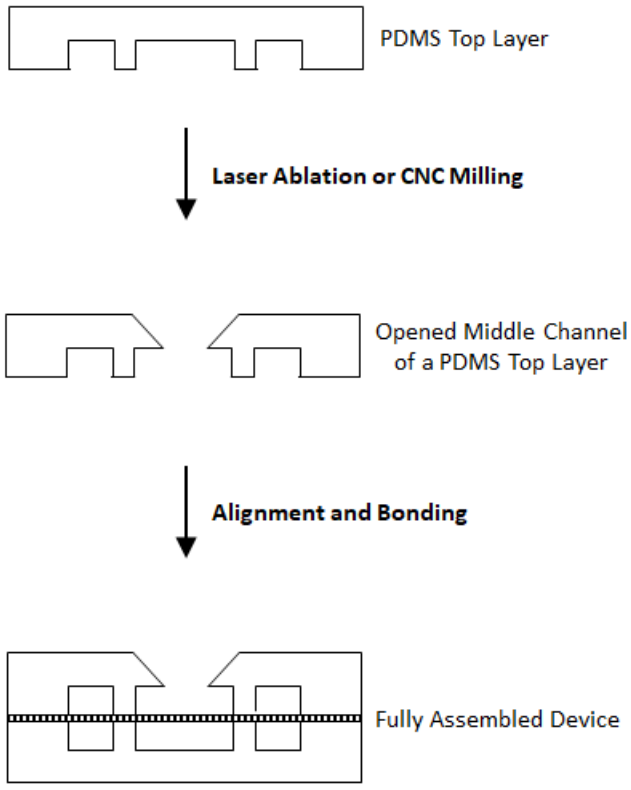

Figure 20: Schematic demonstrating the opening of the middle channel by either laser ablation or computer numerical control (CNC) milling to allow for an air-liquid interface in the lung-on-chip device.

Two techniques were tested to cut an opening along the length of the middle channel, the results of which will be discussed in Chapter 4. One technique used a CO_2 laser (Universal LaserSystems Inc., Model M-Class, Scottsdale, AZ) with the goal of ablating through the entire thickness of the PDMS layer, reaching the top of the middle channel. The second technique used a computer controlled milling machine to cut through the PDMS covering the middle channel.

Laser Ablation

The laser cutter was controlled using CorelDraw (Corel Inc., Ottawa, Canada). The laser functions as a printer, printing patterns drawn by the user in CorelDraw. The user can control variables such as speed, power and pulses per inch (PPI) of the laser by changing settings in the printer properties while the z-axis of the laser platform, and consequently the laser focal point, is controlled by settings on the laser system itself.

To laser ablate the center channel, a straight, 12 mm line was drawn in CorelDraw, creating the channel pattern. Prior to "printing", a piece of clear acrylic was secured to the laser platform using tape. By first laser ablating this acrylic with the channel pattern and subsequently placing the PDMS top layer over the cut such that the cut in the acrylic fell within the center channel, alignment of the device layer for laser ablation could be performed. Using this method ranges in speed (1% - 10%) and power level (50% - 100%) were tested and the PPI was kept at 1000. Either 5 g to 12 g of PDMS mixture were used to create the top layer following the casting methods described previously to test changing thicknesses of the top PDMS layer on laser ablation.

CNC Milling

The second technique tested to open the center channel was computer controlled milling. The general process for this technique is similar to the laser ablation technique: a pattern is drawn often with the aid of computer software and communicated to the cutting device, in this case a milling bit as opposed to a laser. Normally, the pattern communicated to the computer numerical control (CNC) milling machine is created using a computer aided drafting (CAD) software package such as AutoCAD or Inventor (Autodesk, San Rafael, CA) and then converted to a type of programming known as G-code. Although G-code is not a programming language, it is a fairly complex instruction set containing all necessary information for the milling machine. These instructions include spin rate of the milling bit (rpm), XYZ coordinates for each point, rate of speed for changes in XYZ coordinates, as well as automatic tool changes and other, more complex motions.

Rather than draw the design in CAD and convert it to G-code, the simplicity of the channel pattern allowed the direct editing of a G-code file. The top PDMS layer, made from 12 g of PDMS mixture, was placed over a piece of black acrylic on the CNC milling machine's platform. Methods tested for securing the PDMS layer to the acrylic included light pressure by hand, firm pressure by hand, and taping the entire layer down (milling directly through the tape). The narrow channel dimensions (400 μm) and the need for the bit to pass through the entire thickness of the PDMS layer limited the possible selection of milling bits to a triangular (10°) engraving bit with either a 100 μm or 200 μm tip diameter. Alignment was made possible through the use of a handheld digital microscope (Veho, Model VMS-004 Deluxe, Dayton, OH). By manually adjusting the milling bit position while monitoring the surface of the PDMS using the microscope, the bit could be moved to the beginning of the channel and to the surface of the PDMS itself. This XYZ point was taken as "zero" for the purposes of the G-code. The milling bit was then raised and moved to the other

end of the channel (taking care not to drag the bit along the surface of the PDMS). The bit was lowered until a small depression was seen in the surface of the PDMS. This new XY coordinate was taken as the stop point. If the new Z coordinate was positive, meaning higher than the zero coordinate at the other end of the channel, it became the new "zero" for the z axis in order to account for variations in PDMS thickness. By this method, a straight line would be cut from the initial coordinate to the final coordinate regardless of the orientation of the PDMS layer fixed to the acrylic while maintaining a cutting depth just greater than the thickness of the device, itself.

3.2.5 Assembling the three layers to create the lung-on-chip device

The final step in microfabrication of the lung-on-chip device was assembling the individual layers. In the casting method used to fabricate the PM, the PM layer had already been transferred from the PM master wafer to the PDMS bottom layer of the final device through thermal bonding. Therefore, to complete the construction of the device, only irreversible bonding to the PDMS top layer remained. In the stamp method, however, the PM layer was still attached to the sacrificial PDMS slab and had yet to be transferred to the PDMS bottom layer. This transfer was accomplished through irreversible bonding of these layers, induced by a handheld corona generator (Electro-Technic Products Inc., Model BD-20, Chicago, IL) capable of generating an air plasma at atmospheric pressure through an electrical discharge, oxidizing the PDMS surfaces.

For this PM transfer, the sacrificial slab was placed, PM side up, on the workbench next to the PDMS bottom layer, channel side up. The corona generator was turned on and slowly passed over the surfaces of the two layers for 1 minute and 40 seconds. After plasma treatment, the bottom PDMS layer was held over the PM layer and slowly lowered onto a defect free region of the PM layer with the aid of a magnifying lens. The bottom PDMS layer, now bonded to the PM layer on the sacrificial slab, was placed in an oven overnight at 70 °C to complete the irreversible bonding

of two device layers. The next morning the assembled layers were removed from the oven and allowed to cool to room temperature. The edges of the bottom PDMS layer were traced with a razor and one of the corners of this layer was gently lifted and slowly peeled away from the silanized PDMS slab. The PM layer transferred to the bottom layer due to both the permanent bonding between the two device layers and the easy release of the PM layer by the silanized PDMS slab.

Regardless of the method used to create PM layer and bond it to the PDMS bottom layer, the final step in the fabrication of the lung-on-chip device is permanent bonding of the PDMS top layer to the assembled PM/bottom (PMB) layers. To irreversibly bond the PMB layers to the top layer, two methods were evaluated. The first of these used a plasma generated by a plasma cleaner (Harrick Plasma, PDC-32G, Ithaca, NY). When using this method, both the PMB assembly and the top layer were placed in the plasma cleaner such that the surfaces to be bonded were oriented up. The plasma chamber was then pumped down to a pressure of 300 mTorr, before ignition of the air plasma. The PMB assembly and top layer were exposed to the plasma for times ranging from 30 to 60 seconds at medium power. Following exposure, the surfaces were immediately brought into uniform contact, forming the best possible bond. The other method, shown in Figure 21, used the handheld corona generator described above. The corona generator was turned on and passed over the PMB assembly (PM side up) and the top layer (channel side up) for 1 minute and 40 seconds minutes. Again, following plasma oxidation, the surfaces were brought into immediate and uniform contact.

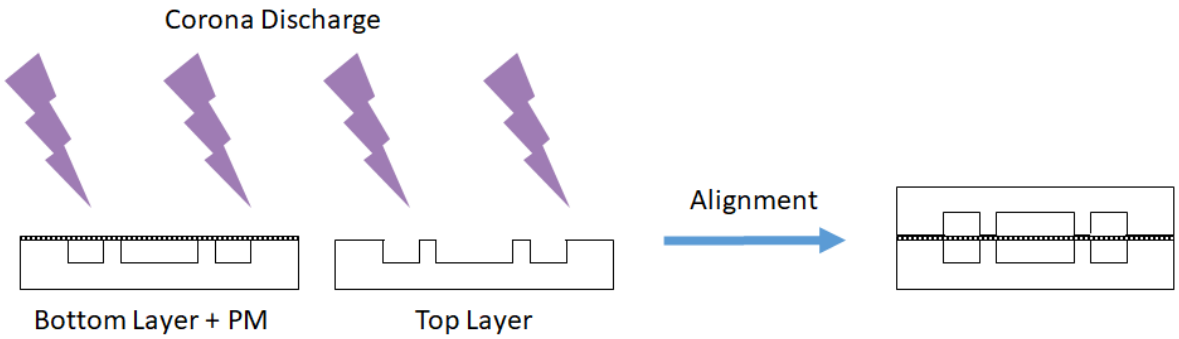

Figure 21: Schematic demonstrating irreversible bonding of the layers of the lung-on-chip device through plasma oxidation using a handheld corona generator prior to alignment.

For this final bonding step, precise alignment was vital, but must be performed quickly as the surface oxidation is temporary. Whether using the Harrick plasma cleaner or the corona generator, the PDMS top layer (channel side down) was held over the PMB assembly (PM side up) and with the aid of a magnifying lamp, lowered onto the PMB assembly such that the center channels and sidewalls of the top and bottom layers overlapped, separated by the PM layer. The bonded layers were placed in an oven at 70 °C to facilitate irreversible bonding.

4. Outcomes of Lung-on-chip Microfabrication

4.1 Photolithography of SU-8 Master Wafers

To microfabricate the lung-on-chip device, master wafers were made, possessing the respective relief features, for each of the three layers: top, bottom and porous membrane. These master wafers were fabricated following the methods described in detail in Section 3.2.1 and had to be made repeatedly as the relief features can lift off or break away with use. The dark field photomasks used in the photolithography process were printed from the AutoCad drawings seen in Figure 22.

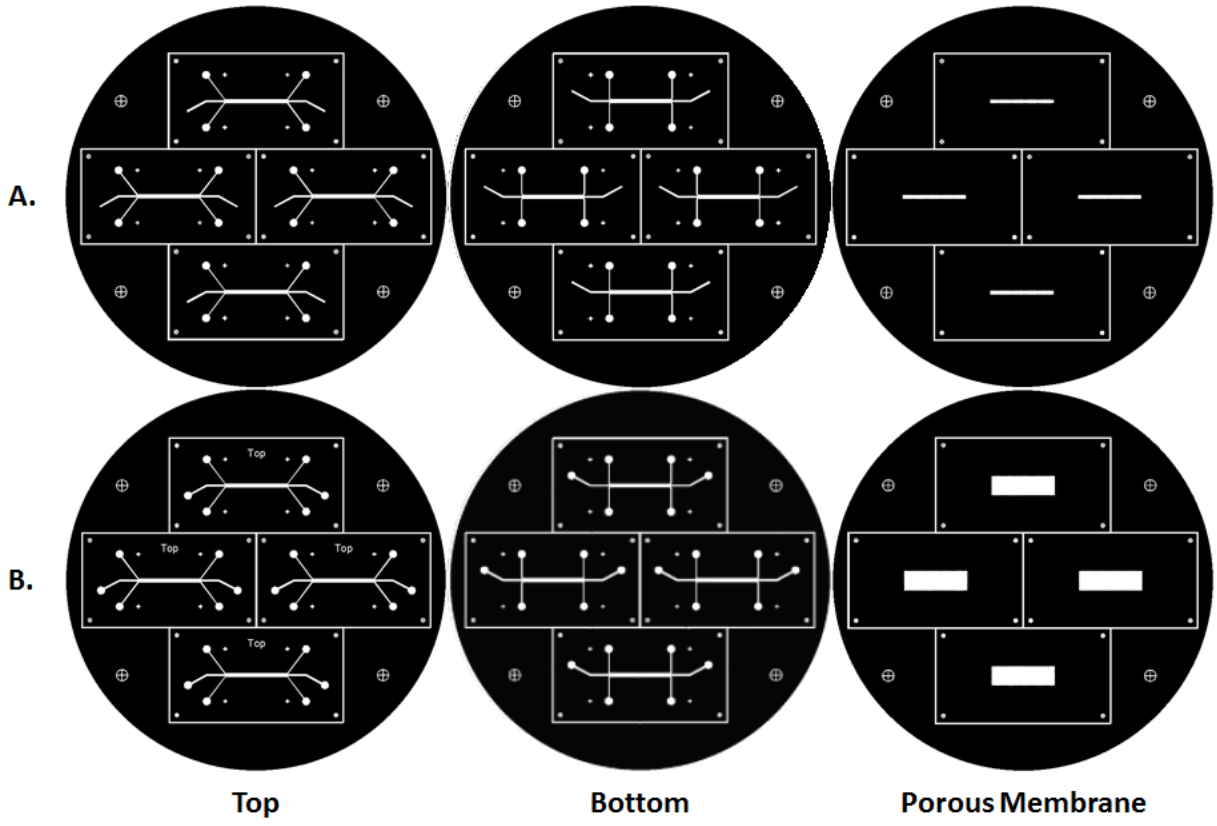

Figure 22: AutoCad drawings of the three individual layers of the lung-on-chip device that were used to create the transparency photomasks. A) Initial drawings and B) final drawings with slight modifications.

The first row (A) shows the initial designs of the three individual layers of the lung-on-chip device. The second row (B) shows the final designs, which were only modified slightly. For the

photomasks of the top and bottom layers, ports were added to the inlets and outlets of the middle channel and the word “TOP” was added to indicate which layer was the top layer. This label guarantees that you are looking at the device from the top rather than the bottom, i.e. if you can read the word top, then the top layer channels are actually on the top. The PM photomask was modified to create a larger surface area of PM to make for easier alignment when assembling the device. The width of the PM pattern in the initial design only spanned the width of the three channels. This left very little room for error in alignment and resulted in little success as seen in the cross-sectional images of fully-assembled devices in Figure 39 in Section 4.3.1.

The lung-on-chip device consists of a top and bottom layer, both with a 400 µm wide middle channel flanked by 200 µm wide side channels. The walls separating the middle channel from the side channels are 75 µm wide. The overlapping portion of the three channels is approximately 1.7 cm long. The top and bottom layers differ only in the placement of the “arms” that extend off the channels. These arms are needed to space the inlet and outlet ports of the various channels and to make room for a microscope objective. Although the three channels of the top and bottom layers need to overlap in the final device, the ports cannot. These dimensions are shown in Figure 23.

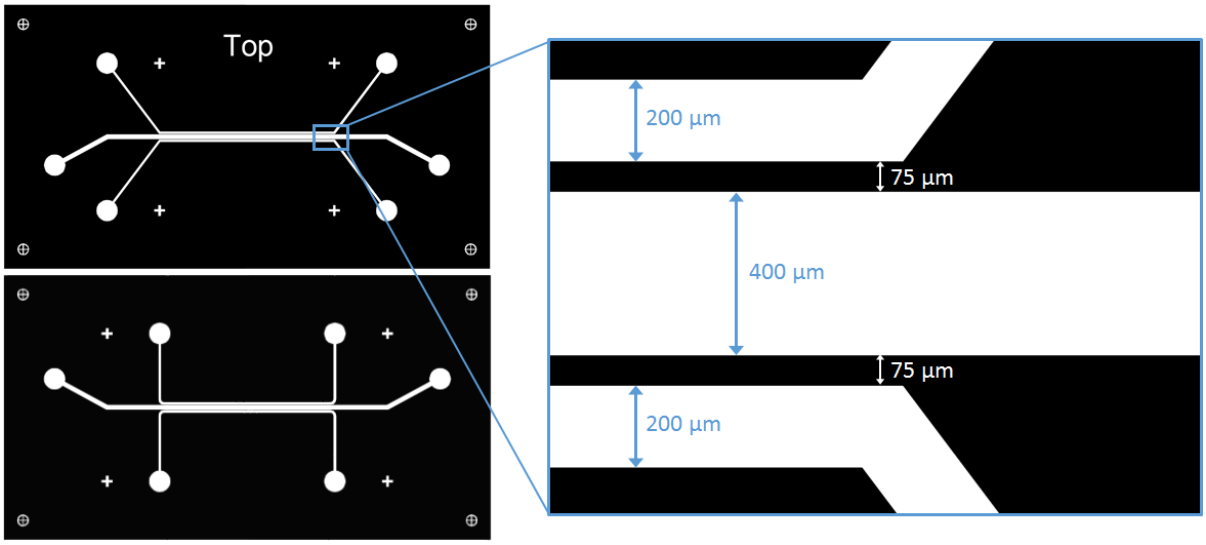

Figure 23: Top and bottom layer channel patterns (left) and expanded top layer (right) with channel dimensions.

The porous membrane layer of the lung-on-chip device consists of an array of 15 µm hexagonal through-holes spaced 63.6 µm apart, center to center, in rows along the length of the array and 45 µm apart, center to center, between adjacent rows. The through-holes of adjacent rows are offset by 45°. These dimensions are shown on the AutoCad drawing in Figure 24.

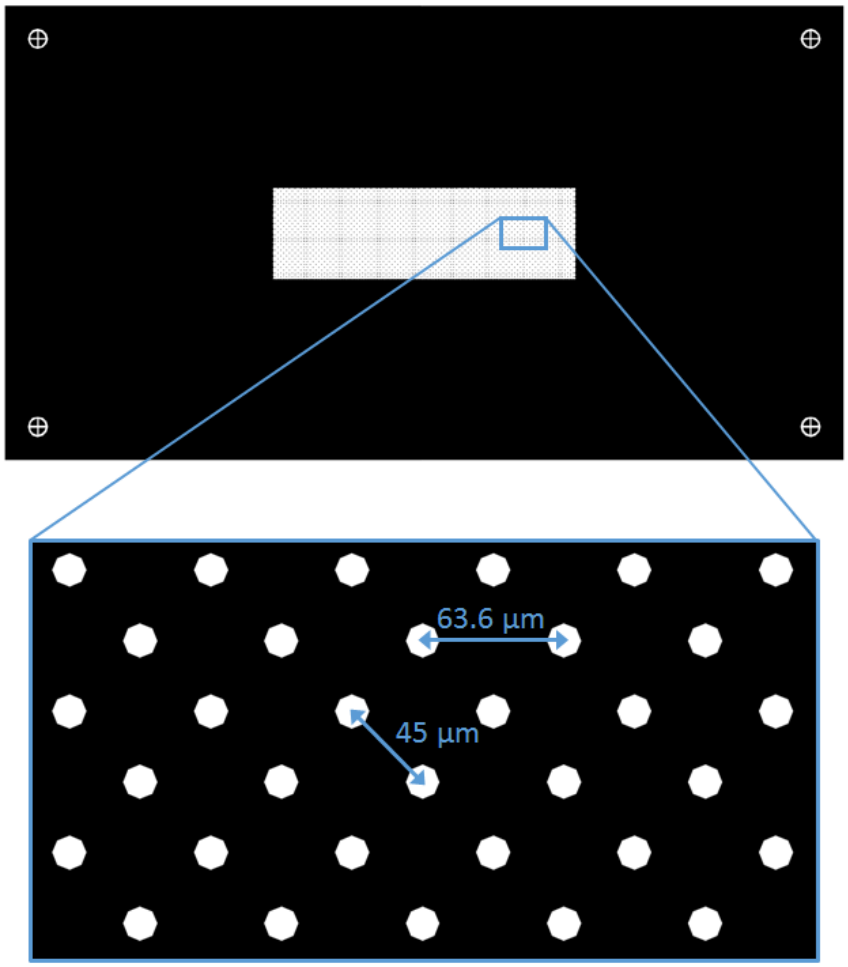

Figure 24: Porous membrane pattern (top) and expanded view (bottom) with spacing dimensions of the 15 µm hexagonal pores.

These AutoCad drawings were made by the Adams Microfabrication Facility before being transferred onto transparency film via high-resolution printing by Infinite Graphics Inc., creating the photomasks for this work. As the exposure method used in contact photolithography results in a 1:1 image transfer from the photomask to the relief features, the measurements of the resulting

master wafers should be nearly the same. Using an optical microscope fitted with a camera and Amscope software, width measurements of the microfabricated master wafers were verified. A representative example for a top layer master wafer and a porous membrane master wafer is shown in Figure 25.

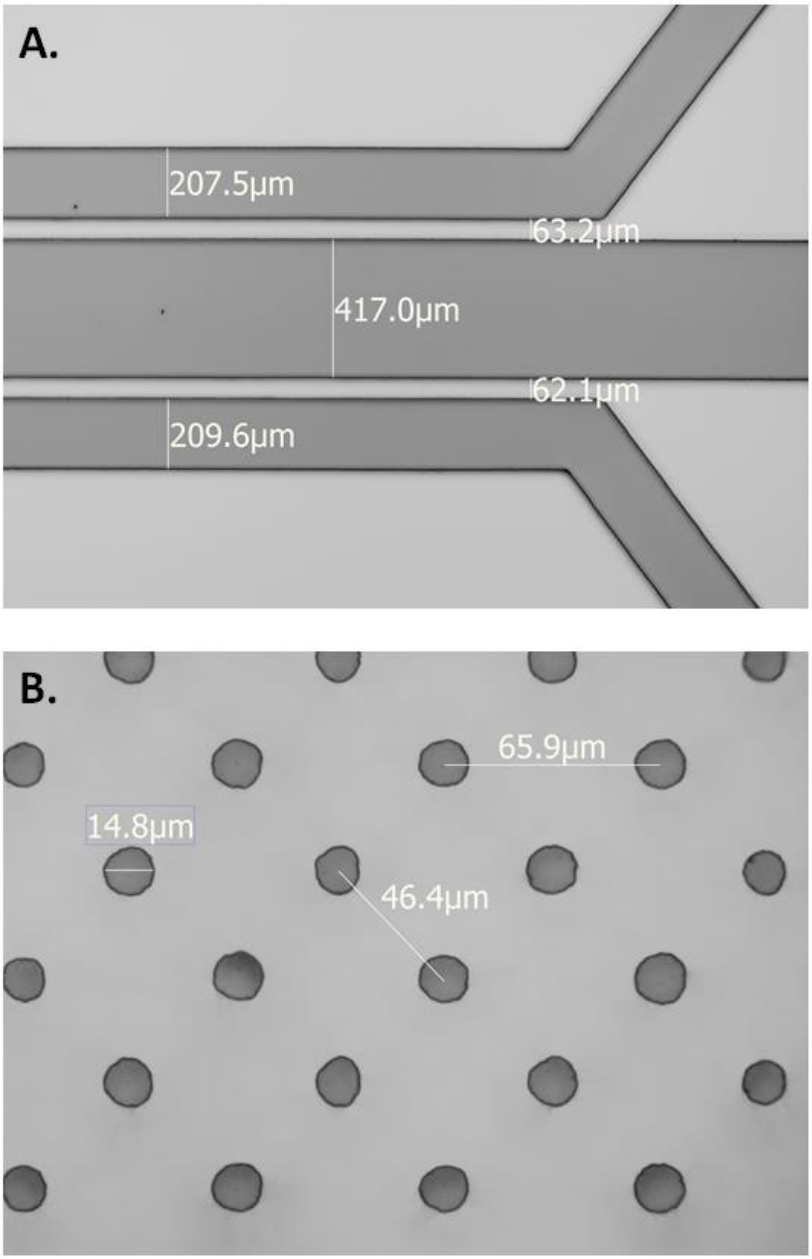

Figure 25: Master wafer dimensions measured with Amscope software. A) Top layer master (5X magnification) with channel and sidewall widths noted. B) Porous membrane master (50X magnification) with pore diameter and spacing noted.

Comparing Figure 25 to Figures 23 and 24, we can see that ratio of the pattern transfer from the photomask to the SU-8 coated substrate for these representative wafers is not quite 1:1. The channel features ended up slightly larger for this top layer master wafer (400 to 417.0 μm for the center channel), narrowing the width of the sidewalls as a result. This could be explained by diffusion of the hexafluoroantimonic acid produced when the SU-8 is exposed to UV. Diffusion of this acid outside of the exposed areas results in poor contrast of the pattern transfer. While SU-8 PR has good contrast, overexposure can cause an excess production of the acid. If the PR was overexposed, the acid would have diffused outside of the exposed regions (into the sidewalls and background) and the resulting channels would be widened while the sidewalls were narrowed. In Figure 25B the size of the pores varied and consequently, so did the spacing. Additionally, spacing measurements were taken center to center, which can result in error since the center is not well defined. However, for this representative PM master wafer the ratio of the pore diameter of the mask to the wafer is nearly 1 to 1 (15 to 14.8 μm)

The feature height, resulting from the spin coating setting, was verified for master wafers using a profilometer and the results of one master wafer can be seen in Figure 26. The height of this representative example was measured at 101.9 μm, slightly greater than the 100 μm that was intended. The feature heights varied from wafer to wafer, similar to the variation found in feature dimensions, exemplified above. However, for this work these dimensions were acceptable as the exact dimensions and height were inconsequential. Fabrication of a lung-on-chip that recreated the scale of the alveolar microenvironment was the primary goal of this work, so variations in photolithography outcomes were tolerated.

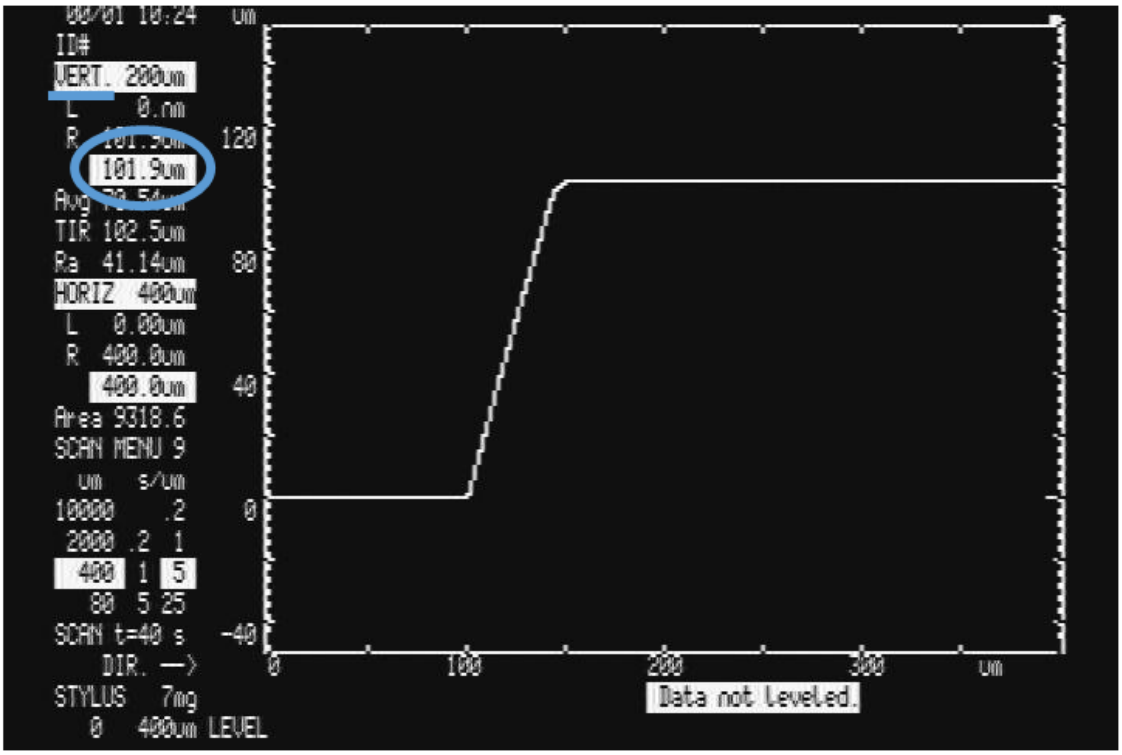

Figure 26: Screenshot of a profilometer measurement indicating the SU-8 PR feature height of a bottom layer master wafer. The vertical height circled in blue was found to be 101.9 µm.

Master wafers of the top and bottom layers made in this work are shown in the following figures and serve as representative examples. For the top layer master wafer (Figure 27), you can see that three of the four devices had no problems upon fabrication. The southernmost device, shown in an expanded view (Figure 27C), is a good example of pattern transfer and adhesion. The rightmost device, however, also seen in an expanded view (Figure 27B), has features that are lifting away from the silicon wafer due to poor adhesion. This is evident by the light color of the PR features that occurs when the features are not in contact with the wafer. Two of the ports are lifting, as is the arm of the middle channel. This was a common problem in this work.

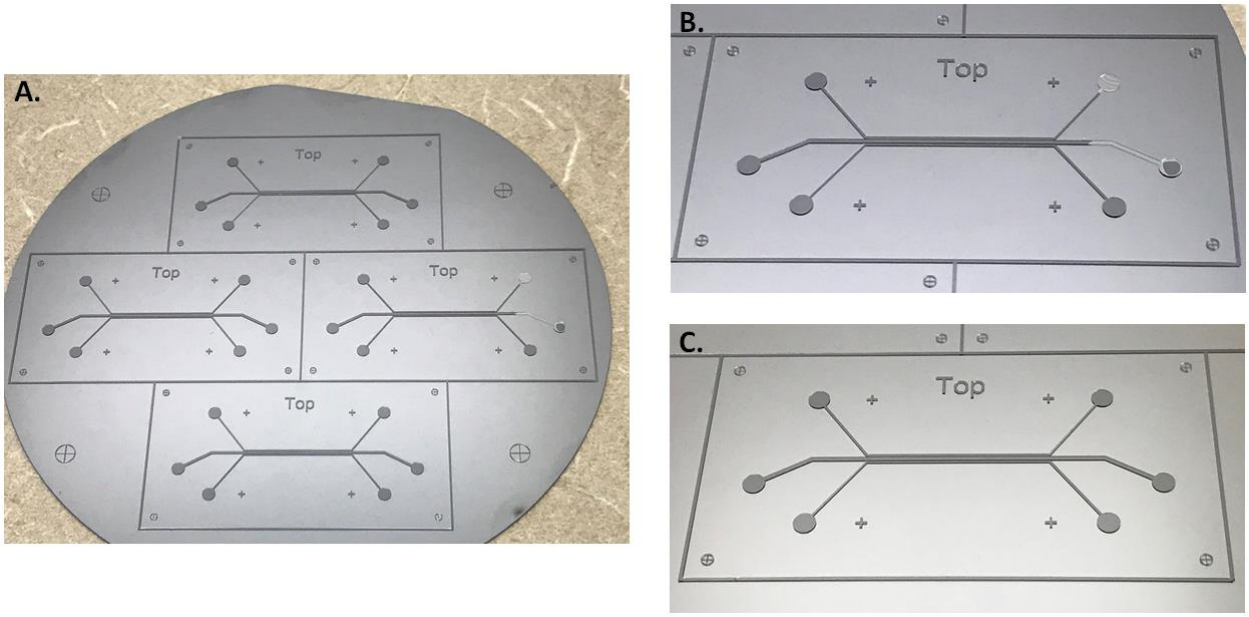

Figure 27: A) Images of the top layer master wafer. B) Expanded image of the rightmost device on this wafer, showing lifting of the features. C) Expanded view of the southernmost device, showing good features with no lifting.

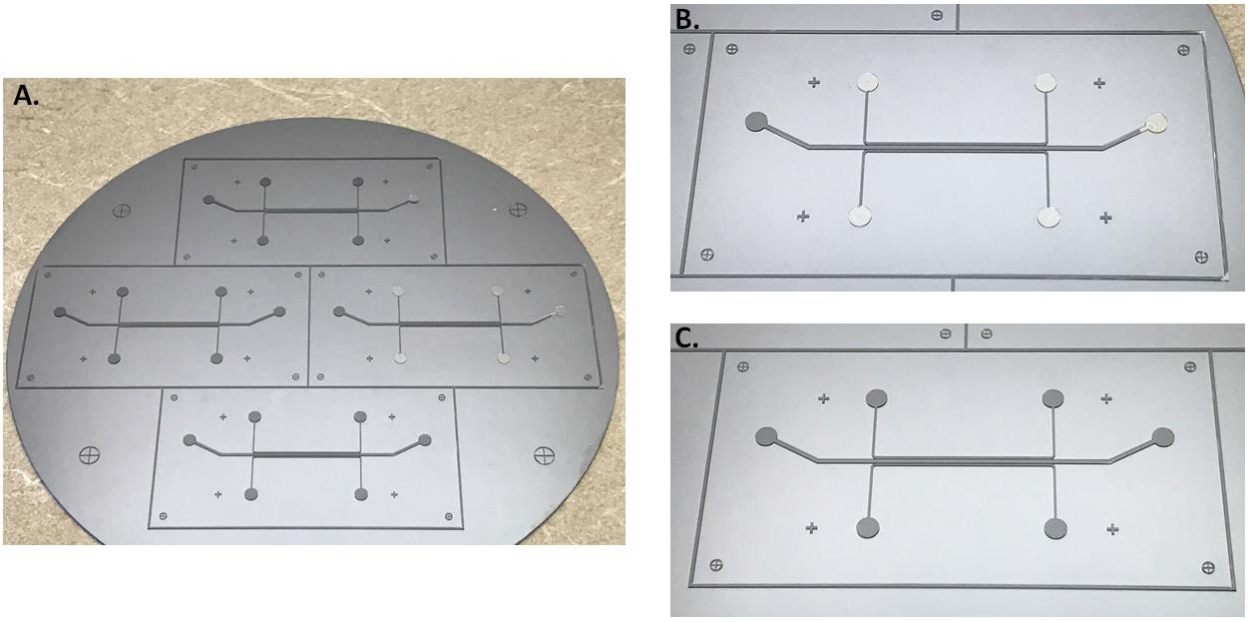

Figure 28: A) Images of the bottom layer master wafer. B) Expanded image of the rightmost device on this wafer, showing lifting of the features. C) Expanded view of the southernmost device, showing good features with no lifting.

Lifting of features is also evident in the image of a bottom layer master wafer (Figure 28). The rightmost device, also seen in expanded view (Figure 28B) has lifting in almost all of the ports. There is also lifting of a port in the northernmost device. Lifting of the features, although not ideal, is not immediately detrimental. The wafers shown here can still be used to create PDMS layers by casting, preferentially to cast the good devices, but even the devices with some lifting can be used. Casting of these devices can continue until the features completely lift off the wafer as can be seen below in Figure 29. Once the features have broken free of the wafer, that particular device is rendered useless.

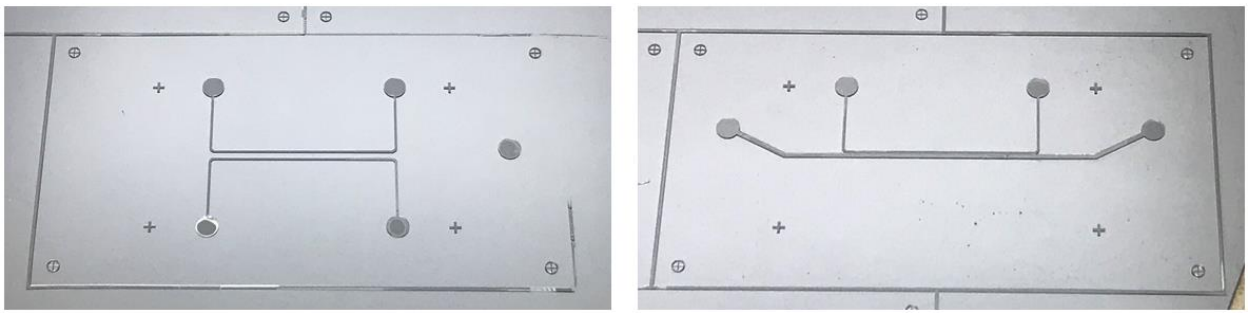

Figure 29: Two examples bottom layer master wafers that had devices with features completely lifted off the wafer, rendering them useless. In the device pattern on the left, the middle channel was removed and on the right, one of the side channels was removed.

The production of SU-8 masters was a continuous process throughout this work. Although the microfabrication techniques are seemingly straightforward, in practice the results can be very unpredictable. Even the "good" devices shown in Figures 27 and 28 can develop lifting over time as they are repeatedly used in the casting steps. Master wafers are expected to fail eventually but not before many uses. The wafers produced in this work often exhibited lifting immediately after development or after casting a handful of times, sooner than should be expected. This was not true however of the thinner, 25 μm, PM masters which lasted for an extended period of time.

The variability from one photolithography attempt to the next was high with respect to wafer failure and number of times casting could be performed. Optimization of the individual steps, such as exposure time, can help decrease this variability but there are some contributing factors that can be difficult to control. The photolithography process takes place in an ISO class 5 clean room, meaning the room is filtered such that the number of 0.1 μm particles should be less than 100,000 per cubic meter. However, if there are particles on the wafer prior to SU-8 PR spin coating, these could affect adhesion of the PR features to the wafer. Compressed nitrogen is used to clean the wafers prior to spin coating but since the impurities can be microns in size, they are not seen by the naked eye and could be overlooked.

The formation of defects in the photoresist film was observed during the photolithography process. The defects were caused when either trapped air bubbles or particulate impurities, that had been present in the volume of PR contained in the dispensing syringe, made their way into the film during spin coating. To prevent defects caused by bubbles, the syringe was left out for an extended amount of time, allowing the bubbles to slowly migrate into the syringe tip, where they could be expelled prior to dispensing. Due to the high viscosity of the PRs used when fabricating the top and bottom master wafers, it was particularly difficult to remove all the trapped bubbles. Consequently, these thicker films had more defects on average. The extended time in the syringe could also inadvertently affect the PR by changing the solvent content (through evaporation) or by introducing particulate impurities. These particles could then end up on the PR film. The defects in the PR film that remain after spin coating caused by bubbles or impurities can affect the film thickness or adhesion. Fortunately, if the defects were few, it was possible to place the photomask in such a way that the features of the mask avoided the defects. In this way, defects were removed upon development.

Humidity is another variable in the clean room that can affect the results. If after the dehydration step the wafer has the opportunity to rehydrate from atmospheric water vapor, adhesion is adversely affected. The cleanroom facility does not maintain a constant humidity and therefore day to day changes in atmospheric humidity can effect master wafer fabrication. However, the Adams Microfabrication Facility has recently added an HMDS oven for HMDS pretreatment, which should prevent room humidity from causing adhesion issues as described in section 2.1.2. This HMDS pretreatment is superior to a dehydration bake and thus the HMDS oven should be used when making future master wafers to continue this work.

Finally, another possible source of variability in the photolithography process is the UV lamp itself. The light intensity of the UV lamp should be tested prior to each exposure to ensure the wafer is receiving the intended exposure dose as normal aging of the mercury lamp can cause changes in output. Changes in light intensity could explain why a once optimized photolithography process can suddenly stop working.

As mentioned in Section 3.2.1, the wafers underwent a dehydration bake prior to spin coating to improve adhesion of the SU-8 PR to the wafer. Additionally, prior to casting, the master wafers were treated with HMDS or PFOTS to aid in release of the cured PDMS from the wafer, extending the life of the master wafer. Despite this, and the extreme care taken to minimize potential sources of poor adhesion, the prevalence of feature lift off remained high throughout this work, specifically for the thicker features of the top and bottom layer master wafers. A possible cause of this could be underexposure, where the cross-linking does not extend all the way through the thickness of the film, to the wafer surface.

SU-8 PR is optimized for near UV (350 - 400 nm), because UV light below 350 nm absorbs intensely at the surface of the of the PR film, resulting in an overproduction of the

hexafluoroantimonic acid at the site of absorption. The local excess of this acid can diffuse wider than the pattern at the film surface, creating a T-profile in the walls of the features. While our profiles did not exhibit the T-profile, these lower wavelengths could result in underexposure (below the local excess of acid at the surface) resulting in fully cross-linked SU-8 at the surface with underexposed SU-8 below this crust that can fail to adhere to the wafer. As such, MicroChem recommends the use of i-line (365 nm) equipment to prevent T-topping and most flood sources used for near UV photolithography are equipped with a filter to block the lower wavelengths. At the time of this work the Adams Microfabrication Facility was operating under the impression that the ABM flood source included this filter when in actuality the lightsource was a broadband mercury UV lamp, which did not filter the lower wavelengths. The facility has since purchased such a filter, which should be used when continuing this work in the future.

The many variables discussed here could explain why we experienced a high variability in wafer success from one photolithography outcome to the next. Top and bottom master wafers made following the same protocol could fail during the photolithography process, after one PDMS casting step, a few PDMS casting steps or dozens of casting steps. Unlike the variability in outcomes for the thick top and bottom layer master wafers, the thinner PM master's did not display any lift off. Despite these sources of variability, SU-8 master wafers were fabricated repeatedly with mixed success for subsequent use in the following steps. Future photolithography procedures should include HMDS pretreatment and filtering of lower wavelength light during exposure.

4.2 Fabrication of a PDMS Porous Membrane with Through-holes

4.2.1 Casting Method

The typical PDMS casting method, in which uncured PDMS is poured over a mold, is insufficient for producing the 10 μm thick porous membrane layer of the lung-on-chip device. Consequently, a spin coater was used to create the PDMS film in the same manner it was used to create SU-8 PR films during photolithography. For PDMS (unlike SU-8 PR), no datasheets exist to define spin rates required to obtain a desired film thickness. As a starting point, 3300 rpm, the spin rate used with SU-8 10 to create a 10 μm PR film, was selected to spread the PDMS over the silanized PM master wafer and through its microfabricated posts. It was not apparent until the three device layers were sealed and a cross-section of the device was observed under a microscope, that the PM layer did not, in fact, have through-holes at this spin speed. The PDMS film created by spin coating at 3300 rpm was actually thicker than the posts were tall, resulting in a PM layer that had a pattern of holes which were actually closed on one side. These closed pores are best seen in Figure 32. As described in Chapter 2, it is typically the spin speed of the spin profile that is adjusted to change the thickness, whereas the acceleration and duration stay the same at 300 rpm s^{-1} and 30 s, respectively. Therefore, to decrease the thickness of the PDMS film below the height of the posts, the spin rate was increased in a stepwise manner beginning at 4000 rpm and increasing to 5000 rpm in 500 rpm increments without changing the duration or acceleration. The results of this investigation can be seen in Figure 30.

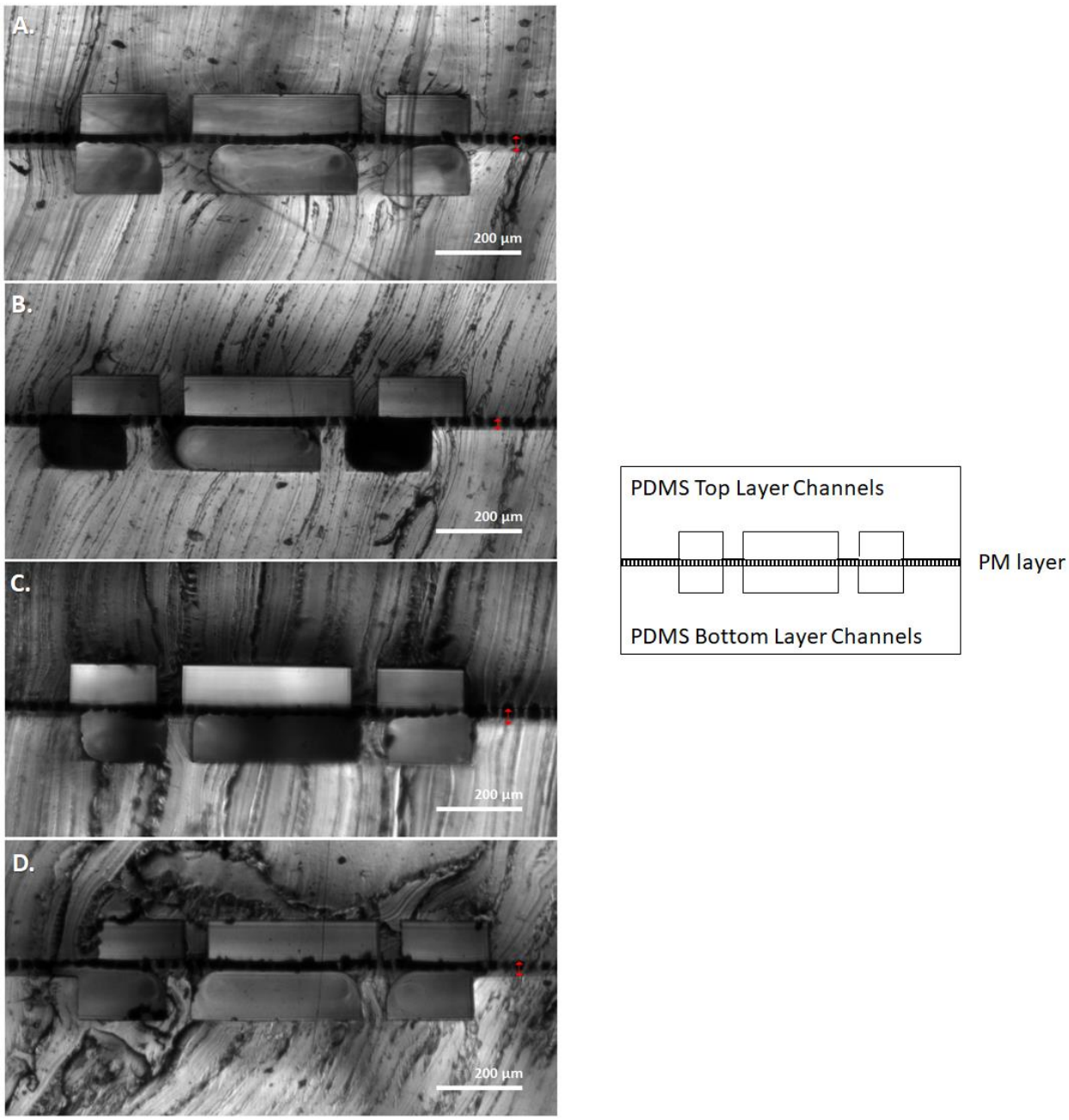

Figure 30: Cross-sectional view (4X magnification) of a fully-assembled device demonstrating PM layers without through-holes obtained by spin coating the PDMS at A) 3300 rpm, B) 4000 rpm, C) 4500 rpm and D) 5000 rpm onto the PM master wafer.

It can be observed in these cross-sectional views that there are no through-holes at any of these spin rates and that the thickness of the membrane does not change significantly with increasing spin speed. With this in mind, a choice was made to decrease the spin rate but significantly

lengthen the duration. This technique was based on a method described in the supporting online material accompanying the lung-on-chip publication by Huh et al [41]. Through-holes were obtained by spinning the PDMS on the master wafer for 10 minutes at 2,500 RPM. A cross-sectional view of the resulting membrane can be seen in Figure 31. Unfortunately, this porous membrane was unintentionally sealed to the non-channel side of the PDMS top layer, which is why there are only channels on one side of the PM.

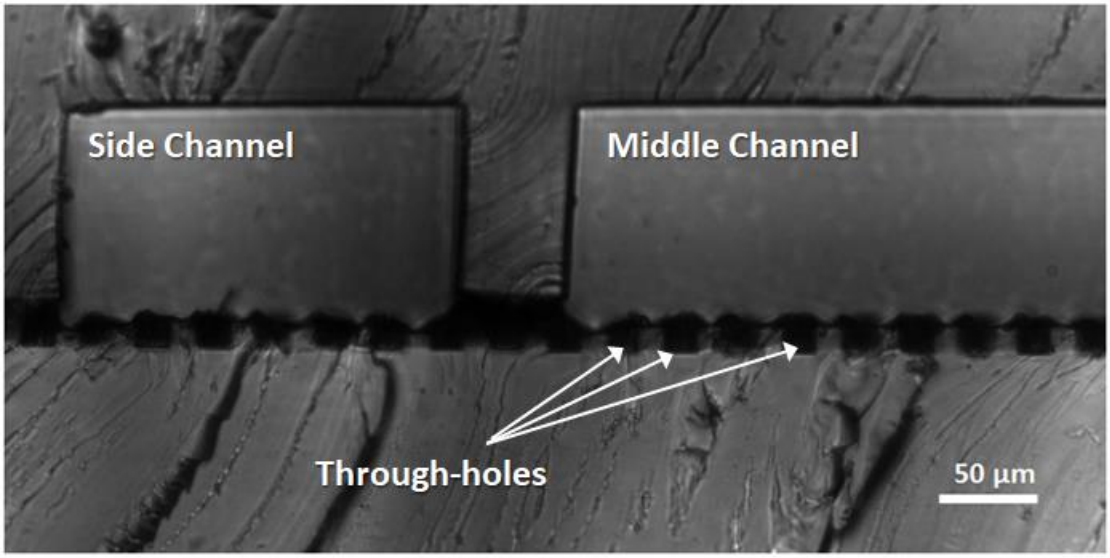

Figure 31: Cross-sectional view (10x magnification) of a porous membrane with through-holes bonded to a PDMS bottom layer (above) and to the non-channel side of a PDMS top layer. The PM layer was created by spin coating the PDMS at 2,500 rpm for 10 minutes.

Although this spin coating technique did result in a PM layer with through-holes, it also introduced new complications in the lung-on-chip device construction that weren't encountered previously. As a reminder, when fabricating the PM layer by the casting method, the PM layer is removed from the posts of the master wafer by bonding the semi-cured PM to the channel-side of the PDMS bottom layer. Once the bonding is complete, the bottom layer, with PM layer attached, is peeled from the PM master wafer. In the initial attempts using high spin speeds and low durations, the PM layer covered the posts of PM master, resulting in a solid layer of PDMS above the posts as

indicated by the red arrow in Figure 32. This undesired lack of through-holes provided both an optimal surface for bonding to the PDMS bottom layer and the rigidity needed for the PM layer to resist tearing as it was peeled from the PM master. Even though the lack of through holes made these two steps of the casting method more easily achieved, they also rendered this method useless, because without through-holes there are no pores in the porous membrane.

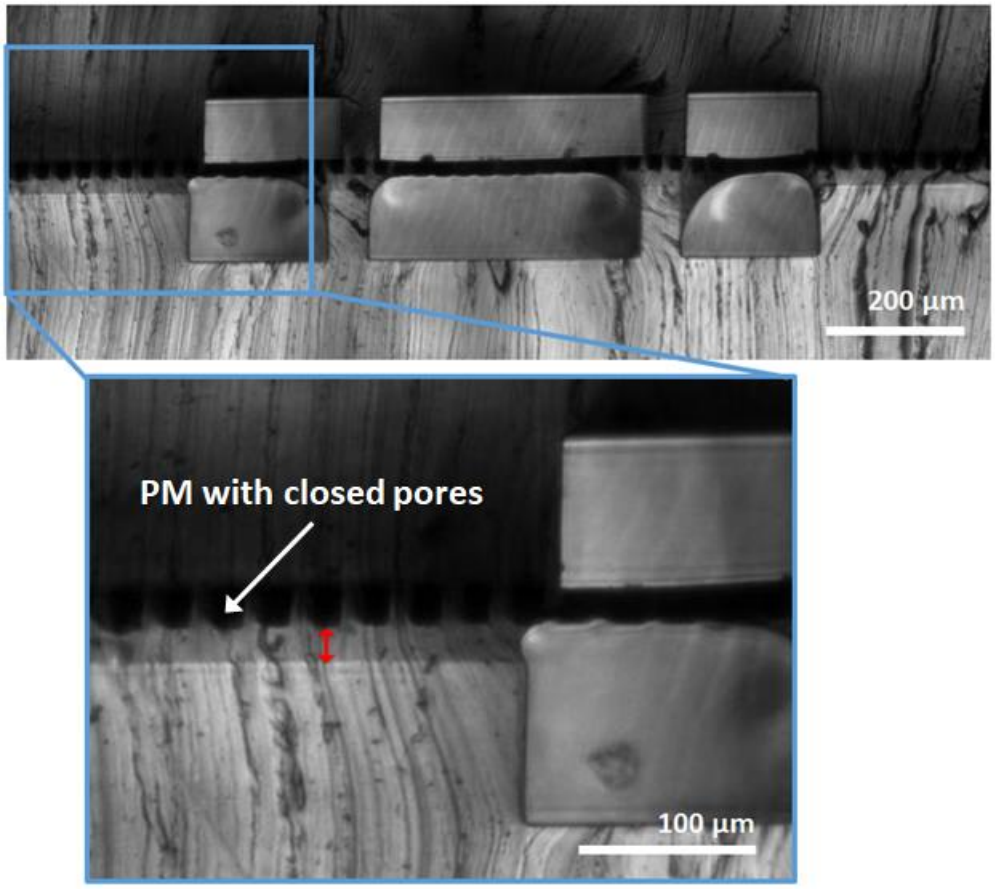

Figure 32: Cross-sectional view (4X magnification) of fully-assembled device demonstrating a PM layer without through-holes obtained by spin coating the PDMS at 3300 rpm for 30 seconds. In the expanded view, the layer of PDMS above the closed pores is visible and the thickness indicated by the red arrow.

In contrast, the PM layers made by spin coating at 2,500 rpm for 10 minutes did have through-holes, but were difficult to remove from the master wafer intact. Since the PDMS of the PM layer is thinner than the height of the posts of the master wafer, contact between the bottom layer and

the PM layer for bonding occurs outside of the area patterned with posts. In the patterned area, however, where the pores are present, the contact is lacking. Porous membrane layers made by this method did not bond as well to the bottom layer, making it difficult for the PM layer to transfer from the posts of the master wafer to the PDMS bottom layer. Additionally, since there are pores in this region, this PDMS layer is fragile and prone to tears. Regularly, the fragile PM layer was unable to remain intact as the layers were peeled from the posts of the master wafer, resulting in regions of PM left behind on the wafer. Therefore, another method was evaluated to fabricate the porous membrane and is discussed in the following section.

To bond the PM layer to the channel-side of the bottom layer, thermal bonding was used. Before the bottom layer was brought into contact with the PM layer on the master wafer, the spin coated PDMS was first semi-cured at 70 °C. The optimized duration for semi-curing this layer was higher when through-holes were not present, and was found to be 12 minutes. When the through-holes were made by spin coating for 10 minutes at 2,500 RPM, the optimized semi-curing duration was 7 minutes. After the layers were brought into contact, with the channels aligned over the PM, The two layers (still on the PM master wafer) were placed in the oven overnight to thermally bond at 70 °C. Sometimes at this point, the formation of bubbles was observed between the layers, where the PDMS cured around trapped air bubbles before the air could escape. This was either due to poor semi-curing or poor technique in bringing the PDMS bottom layer into contact with the PDMS layer on the PM master wafer. After thermal bonding, the layers were carefully peeled off of the PM master wafer. If the PM remained intact, the assembled PM/bottom (PMB) layers were permanently bonded to the channels of a top layer by using a Harrick plasma cleaner. The RF level was set to medium and the optimal duration of RF exposure was 45 seconds.

4.2.2 Stamp Method

The casting method relied upon the fragile PM layer remaining intact after being peeled off of the SU-8 master wafer. As this was rarely the case, the casting method was replaced by the stamp method, in which the microfabricated posts of the PM master wafer are used to stamp through-holes into an uncured film of PDMS. A schematic and detailed description of this method can be found in Section 3.2.3. To reiterate briefly, in this process a PDMS film is spin coated onto a silanized PDMS slab, weighted onto the posts of the silanized PM master wafer so the posts pierce through the film, and cured (Figure 33). The cured film, that is now the PM layer with through-holes, is then removed from the posts by peeling the PDMS slab from the master wafer. The PM layer on the slab is irreversibly bonded to the channel side of a PDMS bottom layer by plasma oxidation using a handheld corona generator and subsequently peeled from the sacrificial slab.

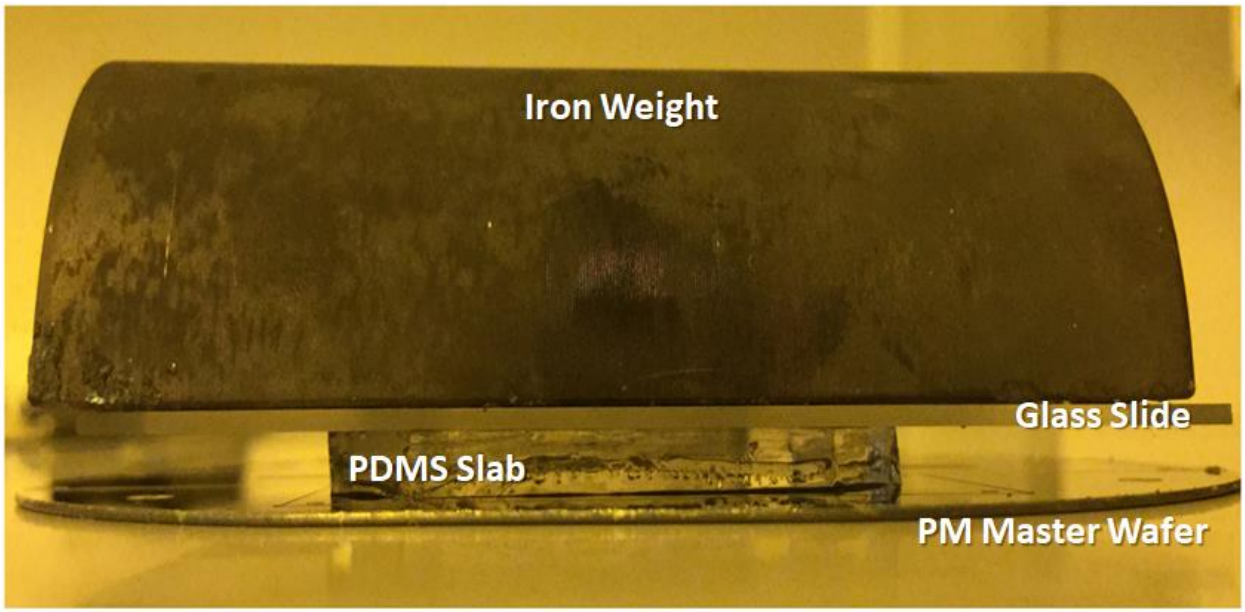

Figure 33: An image of the stamp method used to create through-holes in a spin coated film of uncured PDMS, thereby creating the porous membrane layer. A slab of cured PDMS with a film of uncured PDMS is placed, film side down, on a PM master wafer. A glass slide is placed on the slab and a weight is placed on the glass slide. A schematic of this method can be seen in Figure 18.

Although this method more reliably produced an intact PM layer, it still required refinement of the many steps before it was successful. One undesired outcome, that was actually seen in both methods, was an issue presumably caused by trapped air. This problem was only mentioned above but can be seen here in Figure 34A, which shows a PM master wafer after overnight curing. Disruptions in the PM layers, which are sandwiched between posts of the master wafer and the sacrificial slabs, can be seen in three of the four PM layers shown. We hypothesize that when the film of uncured PDMS was inverted above the posts of the PM master wafer and brought into contact with the posts, air probably became trapped, disrupting the PM layer. Only the southernmost PM layer did not have trapped air. This disruption was not observed until after the overnight curing.

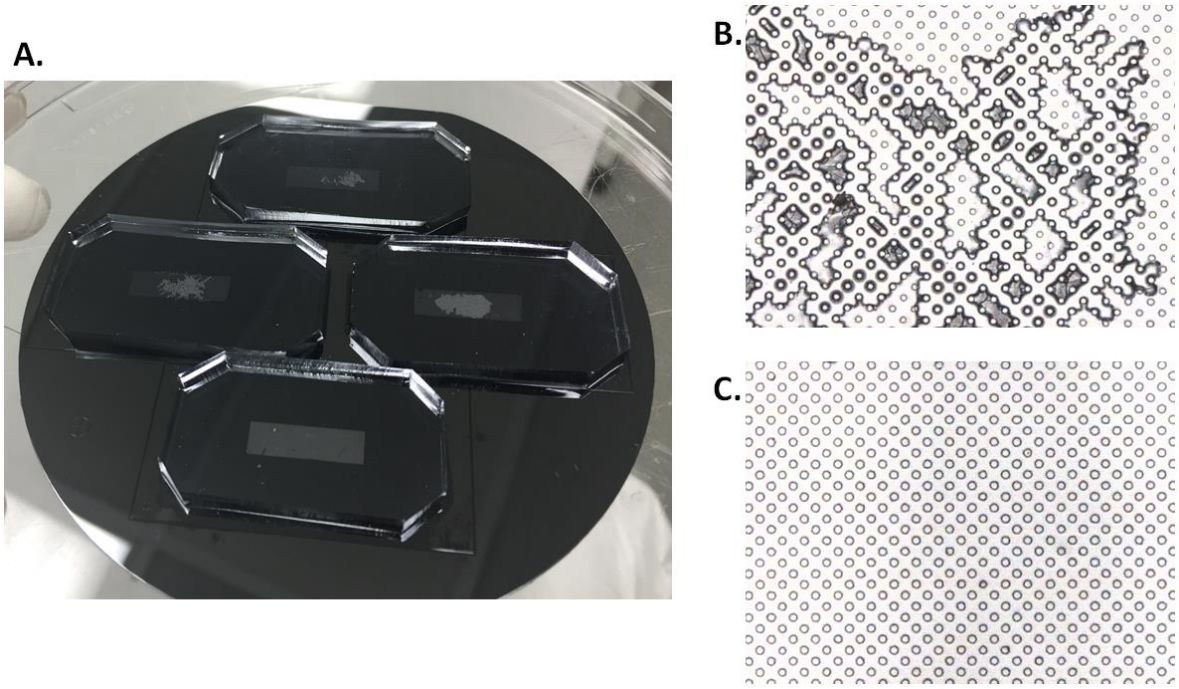

Figure 34: A) PM layers on PDMS slabs that have been inverted onto the posts of the PM master wafer, shown here after overnight curing. The southernmost PM layer is the only one that did not exhibit trapped air. B-C) Images (5X magnification) of a PM layer on the surface of a PDMS slab. B) Example of a PM that results from trapped air and C) example of a PM created when there is no trapped air.

After curing, each of the slabs with the attached PM were peeled from the PM master wafer. Figures 34B and 34C are images of PM layers on slabs, after removal from the PM master wafer. Trapped air results in a PM layer like the one seen in Figure 34B, while a PM without trapped air can be seen in Figure 34C. This disruption to the porous membrane was observed frequently, but fortunately did not occur in all of the films. Porous membranes like the one seen in Figure 34C could be regularly obtained. Additionally, removal of the PM layer from the master wafer was much more successful in this method than in the casting method, but occasionally there were some snags, pun intended. The PM layer in Figure 35 became caught on a region of the PM master wafer when it was being removed, and this snag caused the membrane the stretch until it tore. The PM was cleanly removed from the PM master wafer until this snag occurred, as indicated by PM region to the left of the snag.

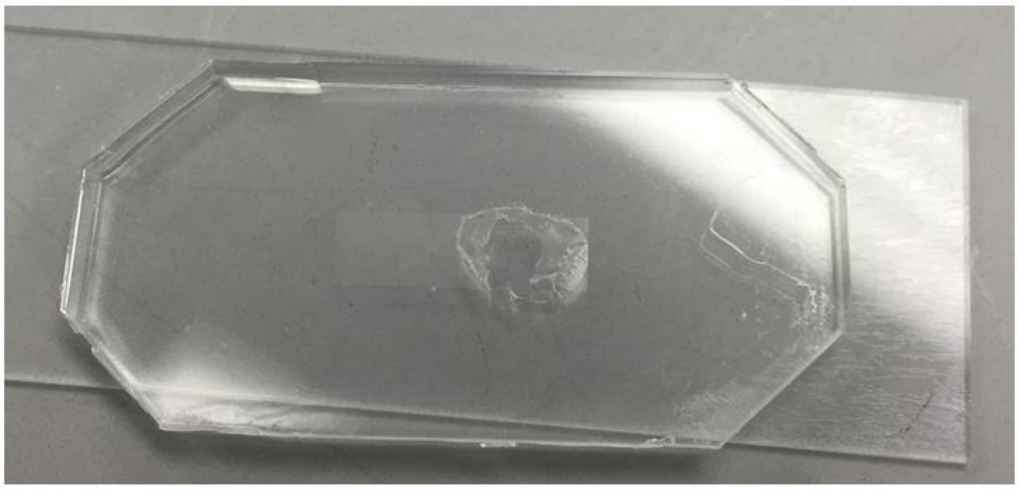

Figure 35: Image of a PM layer (on a PDMS slab) that snagged and tore when being removed from the posts of the PM master wafer.

After a PM layer was successfully removed from the PM master wafer, it was transferred from the PDMS slab to the channel side of a PDMS bottom layer. Plasma treatment was performed using a handheld corona generator and the layers were brought into contact and left in the oven at 70 °C

overnight to complete bonding. When the PDMS bottom layer is peeled from the slab, the PM should preferentially transfer to the PDMS bottom layer both because it was irreversibly bonded to the bottom layer and because the PDMS slab, from which it is being transferred, was silanized with a release agent. Unfortunately, the transfer did not always go according to plan. The images in Figure 36 show the channels of a bottom layer with the pieces of PM that transferred. The remainder of the PM stayed behind on the PDMS slab.

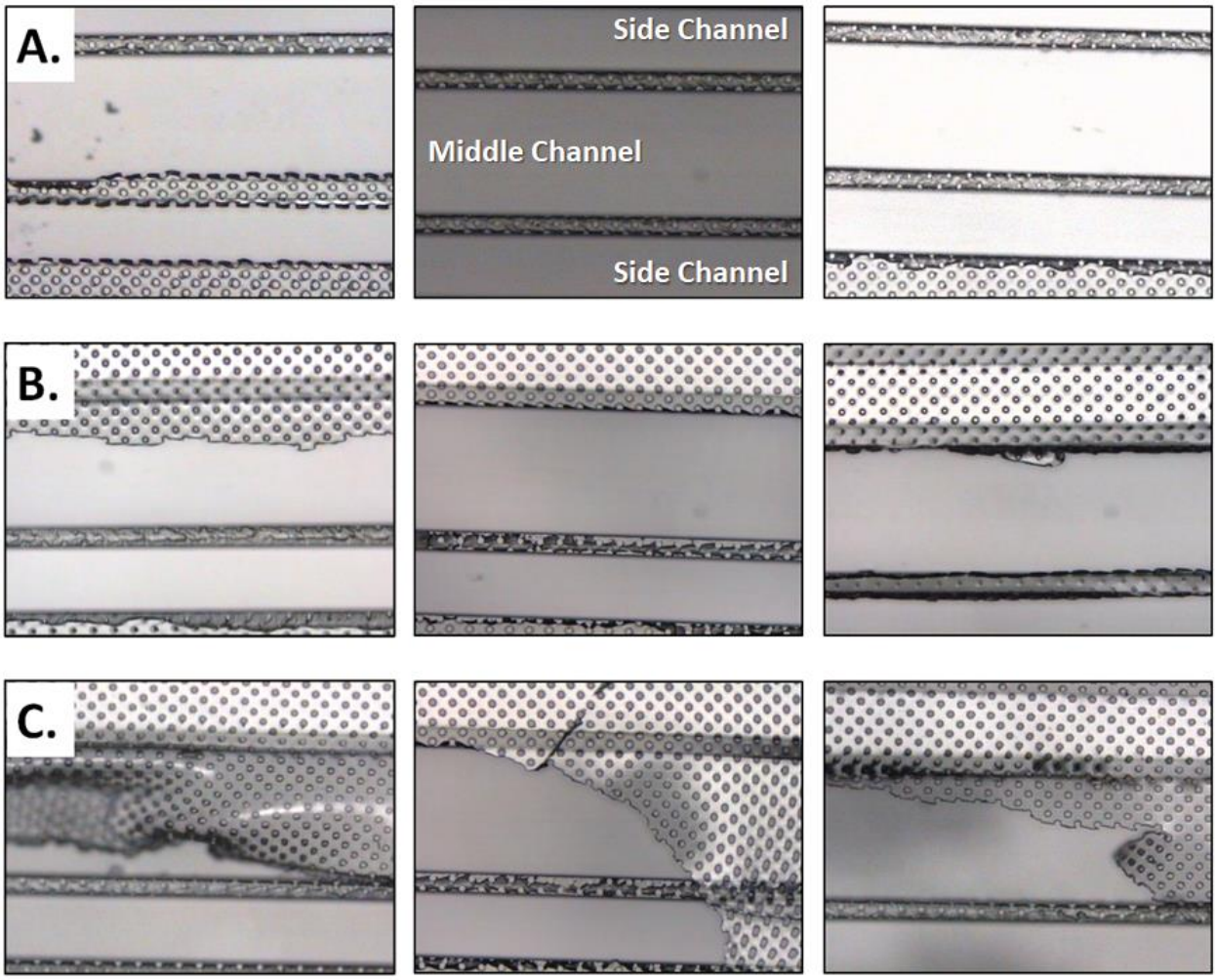

Figure 36: Images (5X magnification) depicting tearing of the PM layer after peeling the bottom layer from the sacrificial slab to transfer the PM layer. HMDS was used as the release agent in the fabrication of these PM layers. A) Transfer of these PM layers only occurred in sidewalls and in regions outside of the channels. B) Transfer of the PM layer was obtained in at least one side channel for these PM layers. C) These PM layers partially transferred center channel.

Row A shows the worst transfer that occurred. In these cases the PM only transferred in the regions where there was direct contact with the PDMS of the bottom layer, i.e. the sidewalls and the areas outside the channels. Within the channels the PM did not have a surface to make contact with, so it tore along the walls and preferentially stayed behind on the slab. This pattern of tearing implied that while the release agent was sufficient where bonding of the PM layer to the PDMS bottom layer could occur, regions extending over channels were not adequately releasing from the slab. In the areas where it was unable to release from the PDMS slab, the fragile PM would tear along the pores as seen in Figure 36. In the transfers shown in row B, the PM layers remained intact across at least one side channel but not the center channel or the second side channel. In Row C the PM layers remained intact across portions of the center channel.

To verify that the stamp method made through-holes, a cross-sectional image of the pores was obtained. Since the PM at this point was not releasing from the PDMS slab and transferring to the PDMS bottom layer, a PM which had remained behind on a slab, was permanently bonded to another slab of PDMS, so the PM could be evaluated. The image in Figure 37, below, shows a cross-sectional image of the of a porous membrane, created by the stamp method, between two slabs of PDMS. The pores extend through the entire thickness of the PDMS membrane unlike the, pores shown in Figure 32.

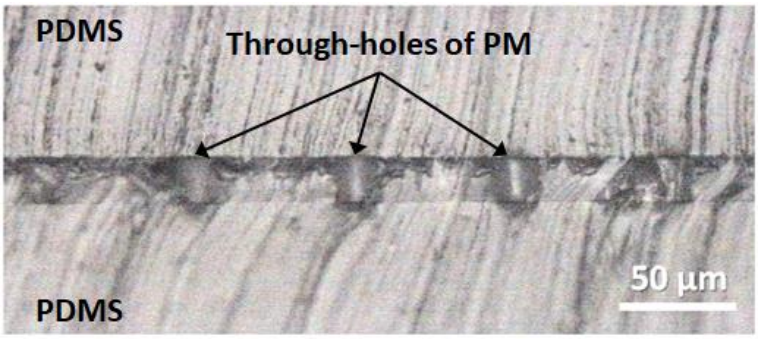

Figure 37: Cross-sectional view of a PM created by the stamp method, displaying through-holes.

A release agent is used on both the PM master wafer and on the PDMS slab to help the PDMS porous membrane release from these two substrates. Essentially, the release agent prevents the PM from irreversibly bonding to the substrate, acting as an anti-adhesive treatment. Vapor deposition of the release agent, either HMDS or PFOTS, is called silanization and is described in Section 3.2.2. Silanization of the PM master wafer is performed to minimize the likelihood of tears or snags, like the one seen in Figure 35 and silanization of the PDMS slab is performed to aid in the transfer of the PM from the slab to the PDMS bottom layer. Although HMDS was adequate as a release agent when applied to the silicon PM master wafer, the images seen in Figure 36 occurred when HMDS was used as the release agent on the PDMS slab. A fully intact PM could not be transferred to the bottom layer, when HMDS was used as a release agent.

Vapor deposition of either of these release agents results in a self-assembled monolayer on the surface of the substrate, modifying the surface chemistry. The release agent reacts with silanol groups on the surface of the substrate, forming covalent bonds. While silanization by either HMDS or PFOTS creates an anti-adhesion layer by rendering the surface hydrophobic, the surface energy of the substrate is lowered more significantly by the highly fluorinated tails of the PFOTS monolayer. This explains why the PFOTS monolayer released the PM layer from the PDMS slab better than HMDS monolayer did (Figure 38). Shao et al. reached the same conclusion when performing PDMS - PDMS casting to produce high aspect ratio PDMS microstructures [60]. For casting PDMS onto their SU-8 master to create the PDMS mold, HMDS was used as a release agent. However, they found that HMDS was not sufficient as a release agent in the secondary casting step, where PDMS was cast onto the PDMS mold. Ultimately, to prevent PDMS-PDMS adhesion they also used PFOTS.

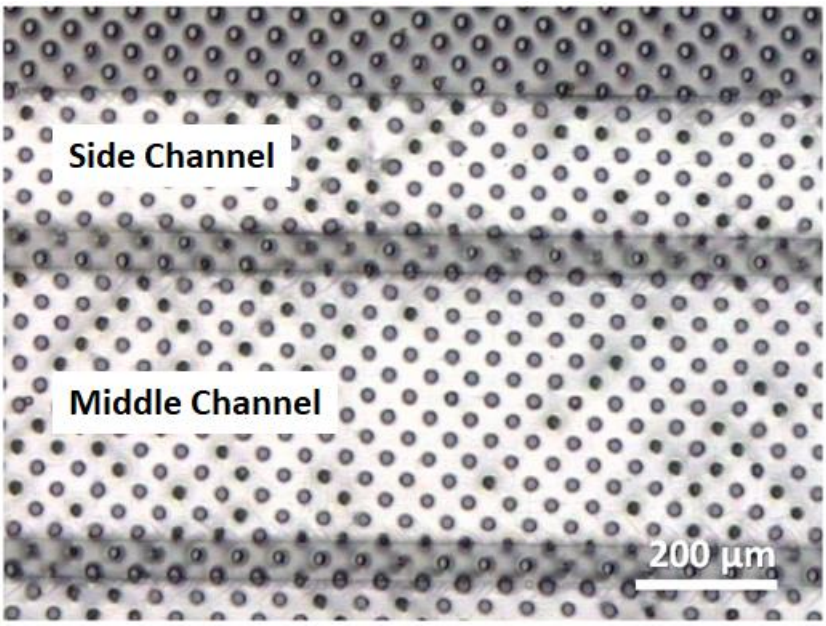

Figure 38: Image (5X magnification) of a PM, bonded to the channels of a PDMS bottom layer, that depicts successful transfer of the PM (across all of the channels) resulting from using PFOTS as a silanizing release agent on the PDMS slab.

Creating the PM by the stamp method had minor issues, like trapped air or PM snags on the master wafer. Fortunately, these issues occurred rarely enough that a PM with through-holes could still be reliably made. The real problem occurred when the PM was transferred from the PDMS slab to the bottom layer. This transfer could not be accomplished when HMDS was used as a release agent, as the PM layer always tore. When PFOTS was used as a release agent, the transfer of a fully intact porous membrane could be achieved.

4.3 Laser Ablation and CNC milling for the Purpose of Creating an Air-liquid Interface

An ultimate goal of the lung-on-chip device was to create an air-liquid interface by opening the middle channel of the top layer of the device. This goal was complicated by the fact that the center channel is only 400 µm wide and is flanked by 75 µm PDMS sidewalls. The sidewalls, which

separate the center channel from the 200 μm wide side channels, must remain unaffected by the opening of the middle channel since they are necessary for proper bonding of the PDMS layers and essential for the mimicked breathing of the lung-on-chip device. Therefore, the middle channel had to be opened using an extremely precise and controlled method to prevent destruction of the sidewalls. These dimensions placed significant constraints on the methods available to open the device. Laser ablation and CNC milling were two methods evaluated as they both had the potential to meet these constraints.

4.3.1 Laser Ablation

Laser ablation is a common method for micromachining and potentially capable of creating an open channel in the lung-on-chip device, due to its narrow beam width. For this work, laser ablation of the PDMS top layer was performed using a CO_2 laser. The model used for this work, the M-Class laser, uses infrared light at a wavelength of 10.6 μm, with an initial beam diameter of 4 mm. This beam is focused using a plano-convex lens with a focal length of 1.5 inches, or 38.1 mm, resulting in a minimum spot size of 127 μm at the focal point, implying the possibility of ablating within the 400 μm channel. The position of the focal point of the beam is positioned by manipulating the z-axis position of the platform. As light focused through a lens to a single point forms a conical shape, we anticipated the conical pattern of ablation to be observed in the cross-sectional view of the PDMS layer. The maximum diameter of the cone within the height of the channel was a limiting factor in the creation of the open interface, as the diameter could not exceed the 400 μm width of the center channel.

Methods used to evaluate the laser ablation technique are detailed in Chapter 3. The beam of the laser (and resulting cut) was aimed at the center channel through three steps. First, a straight-line pattern was ablated on an acrylic sheet that was affixed to the laser platform with tape. Then, the

center channel of the PDMS top layer (or fully-assembled device) was aligned directly over and along this straight cut in the acrylic. Finally, the laser variables were entered using the CorelDraw program and the laser was directed to "print" a second time using the same coordinates, this time ablating the PDMS. If the alignment was accurate and the variables correctly optimized, the beam would ideally cut through the PDMS, reaching the top of the middle channel along the whole length of the channel. The direction along the length of the channel is hereafter referred to as the x-axis and the direction across the width of the channel as the y-axis. In order to optimize the ablation process, a series of variations were planned including varying the speed of the ablation (from 1% to 10% of full speed) and the power setting (from 50% to 100% of full laser power). The full speed of this model of CO_2 laser is 40 in/sec, or 1016 mm/s. In addition to these settings, the number of pulses per inch (PPI) of the laser was set to the maximum value at 1,000 PPI. Cross-sections along the length of the channel were imaged to evaluate the laser cut.

Initial tests to open the top channel were performed on fully-assembled devices with the expectation that manipulation of the focal point (changing the z-axis position of the device) would allow us to cut through the top layer while leaving the underlying porous membrane untouched. Although it was immediately clear that it would be better to ablate the top layer prior to assembling the device, inspection of these cuts led to invaluable insights regarding device fabrication as they revealed that the porous membrane, at this point made by the casting method, did not have through-holes (Section 4.2.1). Additionally, it was evident in the cross-sectional images that what appeared to be proper alignment to the naked eye when the device was viewed from above, was often not the case. This can be seen in Figure 39 below.

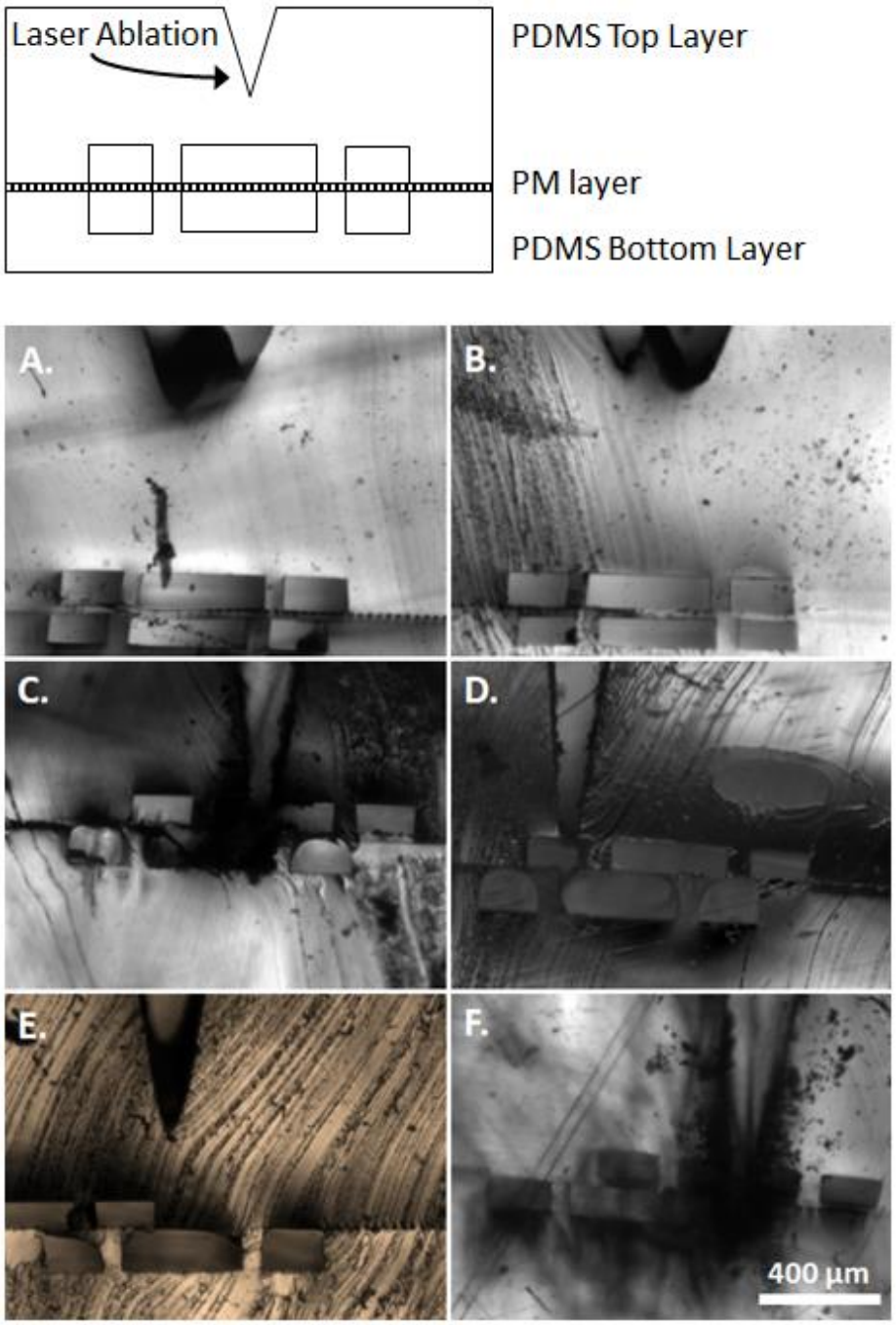

Figure 39: Cross-sectional views (4x magnification) of 5 devices ablated at different speeds while maintaining power at 100% and PPI at 1,000. A-B) Two cross-sectional images taken at different points along the channel of one device that was ablated at 5% speed. C-F) Ablation at 2.8%, 2.7%, 2.5% and 2.0% speed, respectively.

The cross-sectional images in Figure 39 show 5 devices ablated at different speeds while at 100% power and 1,000 PPI. In frames A and B, two cross-sections of a device ablated at 5% speed are

shown at two different points along the channel. One is viewed along the direction the laser traveled and the other from the opposite side. Additionally, two passes were performed, resulting in two conical ablation patterns (most evident in frame B) that reach approximately the same depth, indicating that multiple passes do not increase the depth of the ablation. In frame A, it is clear that porous membrane is poorly aligned and that the pores are not through-holes. Of note, the ablation depth is too shallow. Frames C-F are in the 2.0-2.8% speed range. These slower speeds all result in deeper ablations than the 5% speeds, but the resulting depths within the narrow 2.0-2.8% speed range are variable. Frame C shows that ablation at 2.8% speed resulted in full penetration of the channel, but the ablation may have undesirably penetrated all the way into the bottom layer of the device. Pyrolization obstructs the view and makes it difficult to determine the actual depth of the ablation. Frame D shows a nearly ideal ablation depth at 2.7% speed and minimal pyrolization but poor accuracy of beam aim. The ablation at 2.5%, shown in frame E, is an excellent example of the variability that can be seen with this method as the ablation pattern is shallower than that of the faster 2.7% speed in frame D. Finally, frame F shows ablation at 2.0% speed. The depth of this ablation, similar to the one in frame C, is also obstructed by pyrolization of the surrounding polymer. If the ablation, itself, has not destroyed the porous membrane layer, the pyrolization likely has.

In summary, it was observed that decreasing the speed from 5% to the 2.0-2.8% range allowed for deeper ablation. The laser in some cases even reached to the depth of the channel. However, at this lower speed range pyrolization of the surrounding polymer was more prevalent and the quality of the cut was inconsistent in both depth and amount of pyrolization. These inconsistences could be unrelated to the laser variables. The inconsistent depths could be due to variations in thicknesses of the PDMS layers (and thus the focal point) whereas the pyrolization could be due to local

variations of the PDMS polymer. These observations led to the decision to ablate the top layer of the device prior to assembling the device, thereby protecting the porous membrane from beam depth variations and pyrolization and reducing variations in focal point position. Additionally, it was apparent that obtaining accurate beam aim was difficult either due to poor alignment of the channel onto the cut in the acrylic or to the CO_2 laser's limit of mechanical precision. With respect to device fabrication, the cross-sectional images from these tests revealed that the porous membrane did not have through-holes, which led to optimization of the casting method. These images also indicated that alignment of the PDMS layers needed significant improvement.

To etch the top layer only, PDMS top layers were created as before using 12 g of PDMS (10:1 ratio). This resulted in a PDMS top layer with mean thickness of 1.468 ± 0.102 mm, n=5 as measured by digital calipers. Rather than seal these top layers to the remaining layers of the device, they were instead aligned, channel side down, along an acrylic cut for laser ablation. For these runs the z-axis was fixed such that the focal point of the beam was at the surface of the acrylic. Thus, the beam would be at its narrowest as it breached the channel, which is necessary to prevent destruction of the sidewalls.

As a starting point the initial tests on PDMS slabs without channels began at 10% speed, 100% power. This speed was unable to penetrate the PDMS to a sufficient depth. Decreasing to 5% speed met with the same results. Further tests showed that decreasing the speed from 5% to 1%, laser penetration increased as expected, however at a speed of 1% significant burning of the polymer evident to naked eye began to occur. A range of speed values were evaluated from 1.4% to 2.8% and the power and PPI were kept constant at 100% and 1,000, respectively, to etch the top layer prior to assembling the device. The results of these can be seen in Figure 40, below.

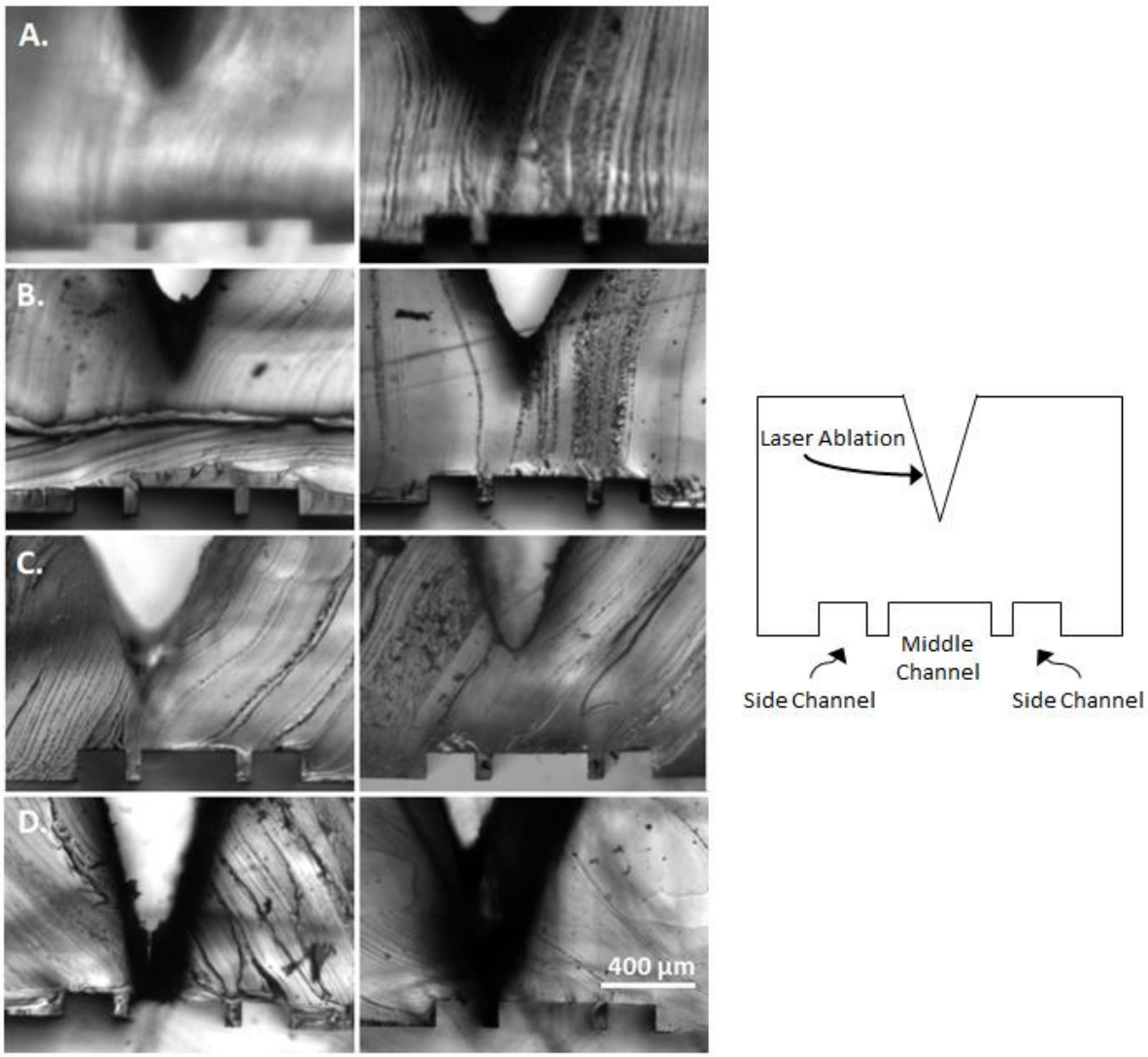

Figure 40: Cross-sectional views (4x magnification) at two points along the channel length (x-axis) of PDMS top layers ablated at different speeds while maintaining power at 100% and PPI at 1,000. A-D) Ablation at 2.4%, 2.0%, 1.7% and 1.4% speed, respectively. Left column: near start of ablation. Right column: near the end of ablation.

Several things can be seen in the cross-sectional images shown in Figure 40. First, the depth of the conical ablation pattern does not reach through to the focal point of the laser (38.1 mm from the lens), which result in ablation through the entire thickness of the PDMS top layer. Second, the depth of the ablation is inversely proportional to the rate at which the laser travels, with slower speeds resulting in deeper etches as the speed is decreased from frame A through D, consistent with the initial work performed on completed devices. It can be seen that while the ablation pattern

approaches the channel in these slower cases, only in the case of 1.4% speed is the channel reached and therefore opened. However, this opening does not extend the length of the channel. It is also evident that despite being at the focal point of the beam, a point at which the spot size should be roughly 127 μm in diameter, the ablation pattern was nearly as wide as the 400 μm channel.

When comparing the left and right columns, which show the same ablated channel at different points along x-axis, variations in the ablation depth and the diameter of the conical ablation pattern and are observed. At a given speed, the widths and/or depths of the 2-D cone in the cross-sectional image differ between columns. For example, the cone is narrower in the right column of frame C and the ablation is deeper in the right column of B. This variability can also be seen when looking at only one of the microscopic images, as dark shadows along the border of the 2-D cone indicate a changing diameter of the ablated area through the depth of the PDMS being imaged (i.e. the x-axis of the device). Since the depth of these cross-sections are small (~3-5 mm) these shadows can indicate a highly variable cone diameter with a small change in x. For example, the clean, narrow borders in the right column of frame C show an ablation pattern that is unchanged with x in this small cross-section; however, it did change between the left and right columns (over a greater change in x). Conversely, the right column of frame B shows an ablation pattern width that is highly variable in the x-direction even in this small cross-section, as seen by the thick dark borders. These shadows are also seen in the z-direction, indicating changes in the ablation depth with small changes in x. This particularly evident in the right column of frame D. Pyrolization is also observed at the 1.4% speed and this could be adding to the dark borders. Ultimately, variations in cone diameter along the x-axis are acceptable as long as the width of the 2-D conical pattern remains inside the width of the 400 μm middle channel. Variations in depth along the x-axis are more problematic, because ideally the entire length of the channel would be opened to create the air-

liquid interface. The highly variable nature of the ablation depth makes it difficult to create a protocol that can consistently open the top channel of the lung-on-chip device.

When comparing Figures 39 and 40, it is clear that beam aim was improved by ablating the top layer alone rather than the fully-assembled device. It was easier to align the middle channel of the PDMS top layer along the cut in the acrylic than it was a fully-assembled device. Poor beam aim can still be seen, however, by observing that the conical tip is directly above the sidewalls in some images. Also, the change in location of the conical tip relative to the channels when comparing the left and right columns shows that maintaining alignment along the whole length of the channels might also be problematic.

This laser ablation study using top layers made with 12 g of PDMS found that speeds well below 2% are needed for the ablated pattern to reach a depth capable of opening the middle channel. Even while keeping all other factors constant, the ablation depth and the diameter of the conical ablation pattern can be highly variable. Despite the variability of the ablation, the 1.4% speed was a relative success as it did ablate through the entire depth of the PDMS, reaching the top of the underlying channel. However, the depth was not consistent along the channel and the beam aim was not accurate, potentially destroying a region of the sidewall. Further tests of lower power settings from 80-100% in an effort to decrease the degree of pyrolization were not able to produce cuts through the entire layer.

In an effort to address the lack of consistency in the ablation depth seen in both studies above, laser ablation of thinner top layers was evaluated. As mentioned previously, we need to ablate at low speeds to reach the necessary depth. Although the broad pattern is that at lower speeds, deeper ablation is observed, at really low speeds the variation is high. Thinner devices decrease the depth that the ablation must penetrate, potentially allowing for the process to be run at higher speeds and

with less variability. To create thinner top layers 5-6 g of PDMS (10:1 ratio) was used. This resulted in a layer with a mean thickness of 0.610 ± 0.178 mm, n=11. A mean thickness of 0.610 mm meant that a substantial depth of ablation was still required. Consequently, work continued with low speeds and high power. Using this thin PDMS layer, speeds from 2.6-3.0% were evaluated while holding the power and PPI constant at 100% and 1,000, respectively. Cross-sectional results of these investigations can be seen in Figure 41.

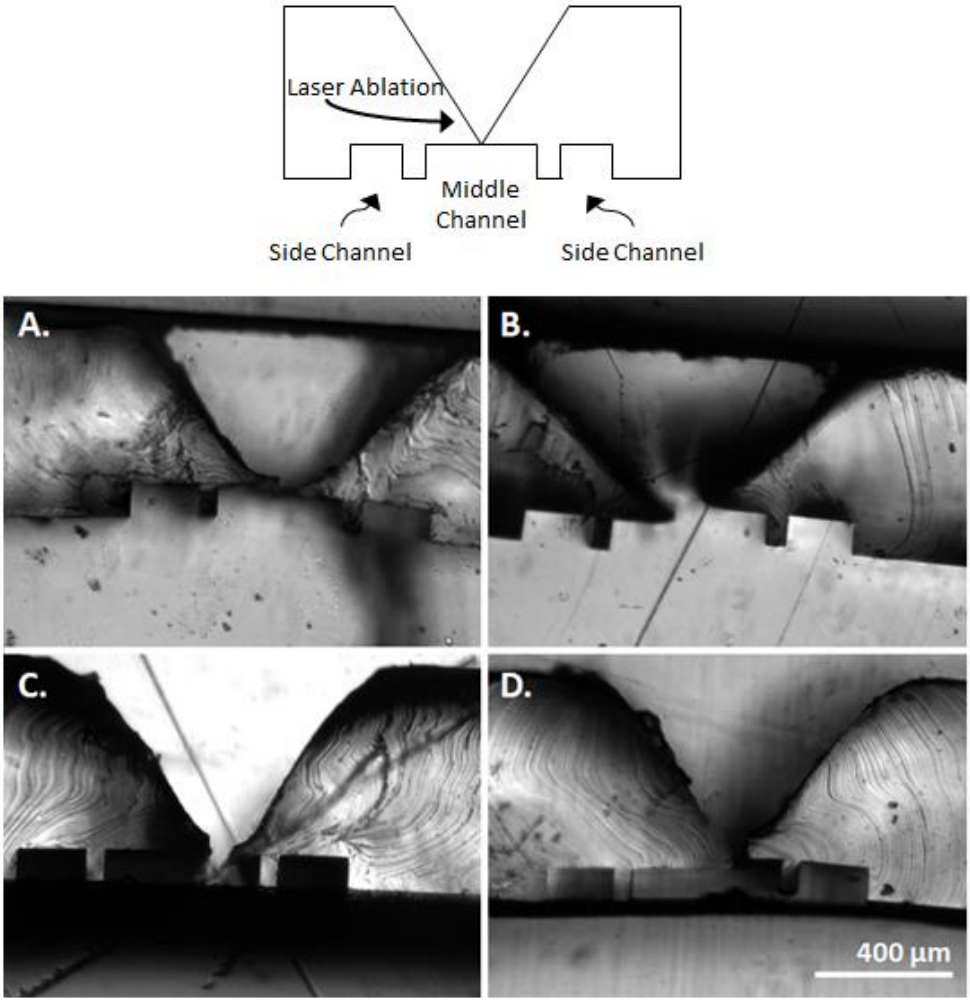

Figure 41: Cross-sectional views (4x magnification) of 5 g PDMS top layers ablated at different speeds while maintaining power at 100% and PPI at 1,000. A-B) 2.6% speed. C-D) 3.0% speed.

As the cross-sectional images show at 2.6% speed, laser ablation was often able to penetrate through the entire depth needed to open the channel (Figure 41B), but not always (Figure 41A).

However, the width of the conical tip made it difficult for the ablation to remain within the channel where it would not harm the sidewalls and allowed for little error in beam aim. At the 3% speed the ablation nearly reached the top of the middle channel but was unable to fully penetrate the PDMS layer. A razor blade was used to cut through the remaining PDMS to open the channel. (Figure 41C-D). This technique was not dependable due to the extremely small size of the underlying structures as well as the tendency for such a thin layer of PDMS to flex or tear. Tape is used to hold the two pieces of the cross-section together after ablation. The tape for the layers ablated at 2.6% speed was placed at the top of the PDMS layer while the tape used for the layers ablated at 3.0% speed was placed at the bottom of the PDMS layer, across the channels. At both of these speeds, a significant decrease in the variation of cone diameter and ablation along the x-axis was observed as compared to the variations observed in Figure 40. Additionally, pyrolization of the polymer was decreased as compared with the ablation patterns of the fully-assembled devices in Figure 39. The thin nature of these PDMS layers led to difficulties in simply handling them and would likely make construction of a complete lung-on-chip device using such layers impossible. Sealing this flimsy layer to the remaining two layers would be nearly impossible especially while maintaining alignment of the top and bottom channels. Additionally, even if the thin layer could be aligned, it could result in structural problems in the device when negative pressure is applied for cyclic breathing.

While reports of laser ablation of PDMS can be found throughout the literature, none attempt to ablate depths such as those attempted here. Two of these reports were particularly relevant for this work. Most notably, Fogarty et al.[61] used this same M-Class laser system for the production of microfluidic channels less than 50 μm on the surface of a PDMS slab. Work by Huft et al.[62] attempted to ablate wells 475 μm in depth, representing the deepest ablation of PDMS found in

the literature. The laser power settings used range from 3-95% (Huft) or were kept constant at 100% (Fogarty) and the speed of the ablation was 30 mm/s (Huft) or 20% of full speed (203 mm/s) (Fogarty). Direct comparisons between the laser used by Huft et al. and laser used here are difficult. Direct comparisons with those of Fogarty et al. are possible however, assuming no change in the equipment during the intervening period. The ablation depth needed to open the 12 g PDMS top layers is at a minimum, 1.2 mm which is over 2.5x deeper than then wells ablated by Huft et al. However, the ablation depth needed to open the thin PDMS top layers should be obtainable based on their work.

At each point in the evaluation of PDMS laser ablation for opening the top layer, it was found that slower speeds did result in deeper ablation of the PDMS layer and 100% power was needed to reach these ablation depths. However, the ablation pattern (depth and cone diameter) was found to be highly variable especially at low speeds. The ablation depth needed for fully-assembled devices could not be reached and the variability in results obtained when ablating a 12 g PDMS top layer made obtaining consistent results nearly impossible. While the ablation depth needed for the thin top layers could be met, cone diameter and beam aim became more of a problem. Additionally, these thinner devices would not be suitable for device construction or function. It was, therefore, decided that this technique would not be capable of consistently creating open top layers. Consequently, another method of opening the top layer of the lung-on-chip device was sought.

4.3.2 CNC Milling

The inability of laser ablation to open the middle channel of the PDMS top layer led to the search for other methods that could remove a region of PDMS with extreme precision. As mentioned above, making a cut that remains within the 400 μm center channel along the length of the channel requires extremely tight mechanical tolerances. Any deviation in path could result in penetration

of the sidewalls, rendering the device useless in terms of its "breathing' capabilities. Among the techniques capable of such a precise cut is CNC milling, which is described in Chapter 3 (Section 3.2.4). The Adams Microfabrication Facility possess a Wabeco 3-Axis CNC Mill. This CNC is capable of a positioning accuracy of ± 5 μm which places it well within the necessary tolerances for this application. Additionally engraving bits down to a tip diameter of 100 μm are available and could be used for these precise cuts.

For the purposes of this work CNC milling has several benefits that laser ablation lacks. One significant benefit is that contrary to the cuts made by laser ablation, where depths of the cuts could not be explicitly defined, the depth of cuts made by CNC milling could be precisely controlled by defining the z-axis coordinate of the milling bit. In other words, cut depth was defined by the user rather than an outcome of a combination of laser ablation parameters. In this way variations in the PDMS thickness of the top channel layer both along a channel and between different layers could be accounted for in each cut made by the CNC. The ability to define the depth of the cut guaranteed complete opening of the top layer.

Two engraving bits that possessed the same geometry were evaluated. The tip diameters of these bits were 100 μm and 200 μm, both of which were narrower than the width of the center channel. Unlike typical cylindrical milling (or drill) bits, which were unavailable at these sizes, the 100 μm and 200 μm bits are triangular in geometry with a 10° angle. As the width of the bit increases above the tip, the cuts were widest at the surface of the cut. To ensure that cut to the channel was as narrow as possible, the cuts were made with the channel side down, such that the surface of the cut was on the non-channel side.

Like laser ablation, CNC milling of a material involves a process of parameter optimization. The two parameters that can be optimized are the feed rate and spindle speed, or "*feeds and speeds*" in

the vernacular of CNC milling. These parameters depend on the geometry of the milling bit and the material being milled. *Feeds* define the rate at which a milling bit travels in the X/Y/Z planes, measured in mm per minute (mm/min) and *Speeds* define how fast the spindle, upon which the milling bit is mounted, spins in rpm. The selection of optimal values for feeds and speeds was performed to create the cleanest possible cut to the polymer, ideally minimizing disruption to the PDMS surrounding the cut. To optimize the feeds and speeds, an array of possible values was tested, with speeds ranging from 20,000 – 40,000 rpm paired with feeds ranging from 100 – 1050 mm/min. These values were laid out in a grid pattern to rapidly evaluate all combinations, incrementing the spindle speed in rows by 5,000 rpm and incrementing the feed rate of the square sides by 50 mm/min (Figure 42).

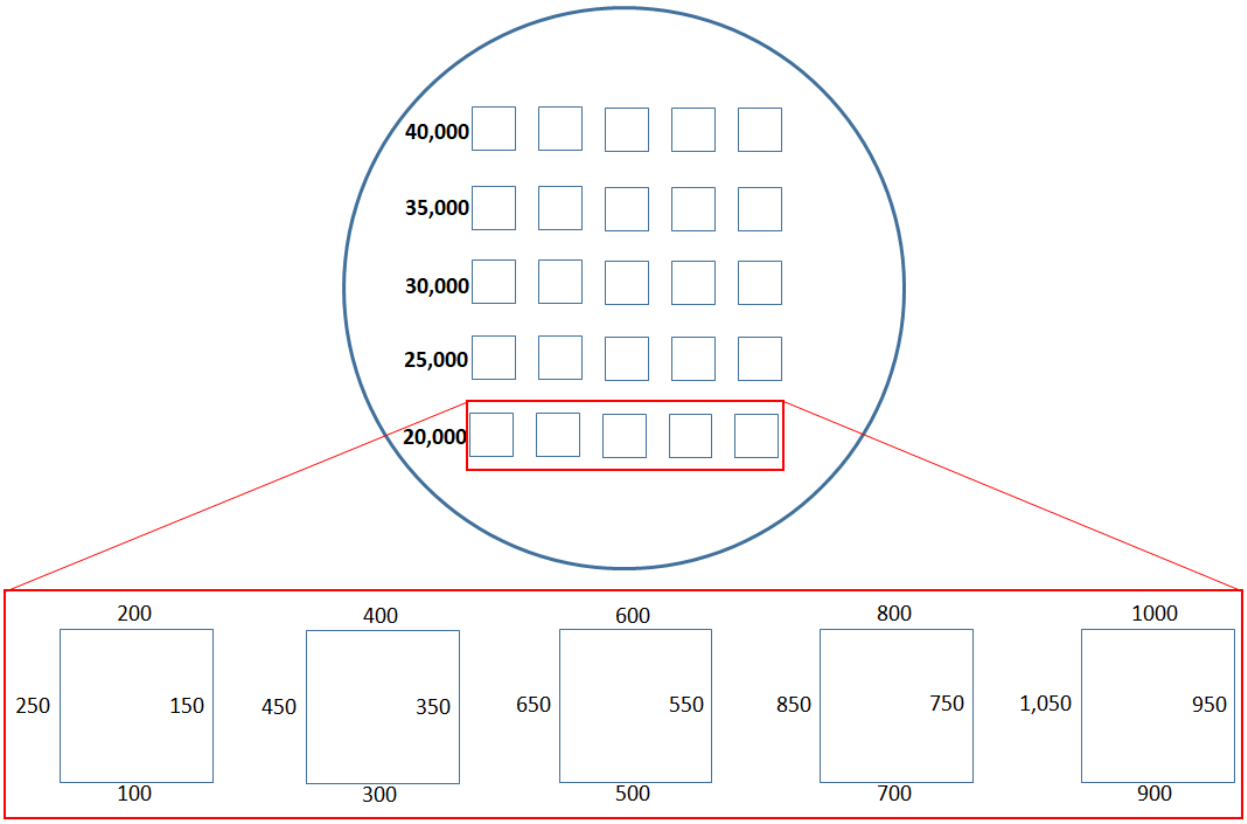

Figure 42: Schematic of the CNC milling that was performed on PDMS, showing the milling pattern that allowed for rapid optimization of the feed and speed variations. Each row tested one spindle speed (rpm), as denoted in the schematic, and within the row each side of a square tested a different feed rate (mm/min), as denoted in the expanded view.

The results of this milling array can be seen in Figure 43. The general finding from this evaluation was that for PDMS, spindle speeds on the lower end of those evaluated combined with feed rates in the mid to high range tended to produce cleaner cuts. For this reason, a spindle speed of 20,000 rpm and a feed rate of 600 mm/min were chosen for the initial evaluation of the milling process.

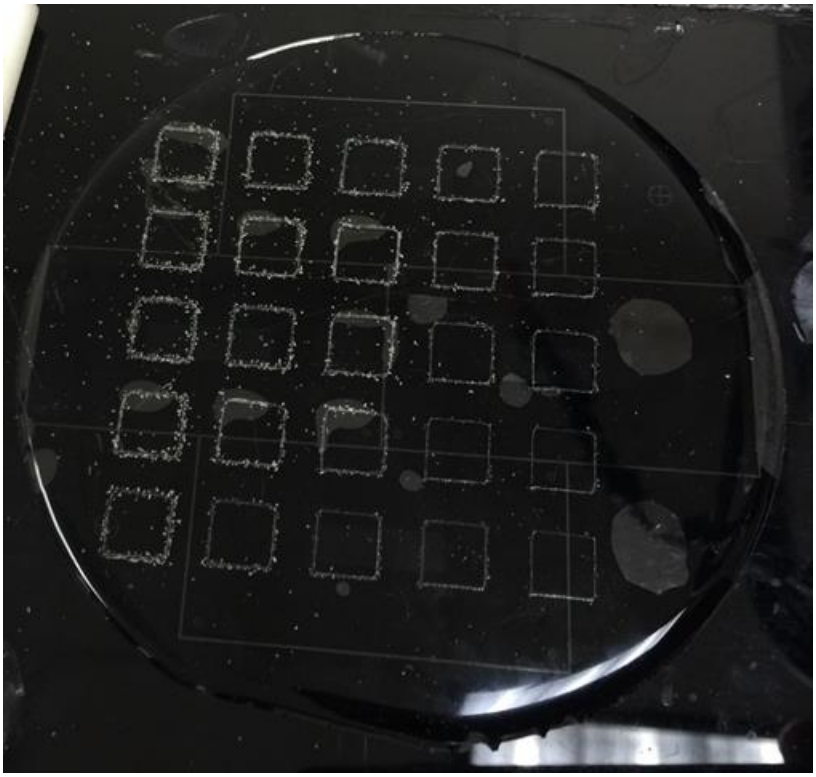

Figure 43: Image of the PDMS, after CNC milling of the optimization array, used to select the spindle speed and feed rate combination.

The process of aligning the milling bit to the center channel was performed by first securing the PDMS top layer, channel side down, to an acrylic surface on the platform of the CNC. Using a digital microscope (described in section 3.2.4) the milling bit was then brought into alignment with the middle channel and lowered until contact was made precisely at the center of the channel (Figure 44). The CNC stored the location of the aligned bit, as XYZ coordinates, that were then defined as the origin of the coordinate system. The bit was then raised slightly and moved to the

other end of the channel and the same alignment was performed. The xy coordinates were recorded again to be typed into the G-code. The G-code directed the CNC controller to make a straight line from the origin to the second defined point at a specified depth. This ease of alignment was an additional benefit to using the CNC as opposed to laser ablation. In fact, the alignment technique when using the CNC is inherently superior to that used to when performing laser ablation. In the case of the CNC, the bit does not need to aimed at the channel. Rather, two points on the channel are defined after the bit, which knows its XYZ coordinates, is physically aligned to them and the CNC cuts a straight line between these two points. On the other hand, for laser ablation the beam had to be aimed at the center channel since coordinates of the print pattern could not be defined within tolerances of the channel. With this aiming method, we could not guarantee that the beam was cutting in the exact same place twice nor that the alignment of the channel to the cut in the acrylic was adequate.

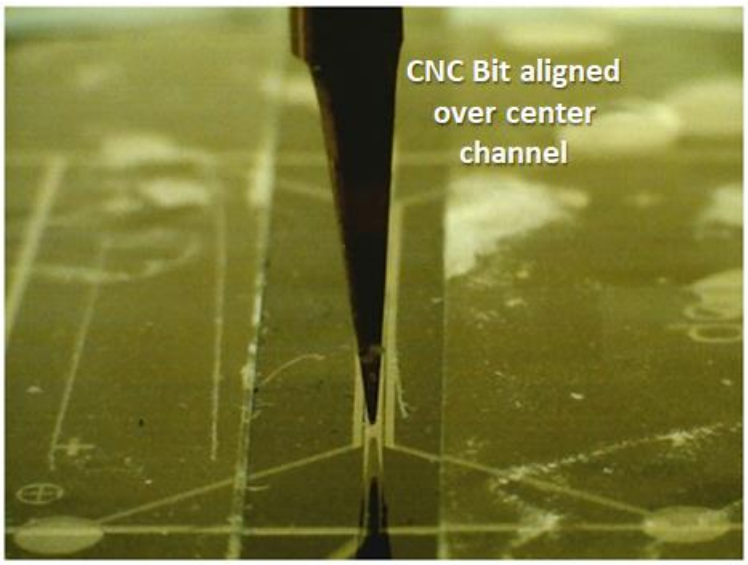

Figure 44: Image taken from video feed of a handheld digital microscope, that was used in aligning the CNC bit to the center channel. Rather than align the PDMS layer to the cut, the CNC allowed us to align the process of cutting to the location of the PDMS.

Preliminary cuts using parameters obtained from the feed rate and spindle speed optimization can be seen in Figure 45. For the center cut, the 200 μm milling bit was aligned over the channel before the spindle was brought up to speed and lowered into the PDMS layer at a rate of 50 mm/min to the full depth of the PDMS, approximately 1.5 mm. The spindle, rotating at 20,000 rpm, was then moved along the channel at a feed rate of 600 mm/min. Despite specifying a completely linear path in the G-code, the resulting milling pattern was shown to initially follow a curved path before straightening. This curvature went unnoticed in the optimization studies and was likely exaggerated here due to the depth of this cut. The PDMS polymer seems to have flexed in response to the bit when it first begins to travel down the channel.

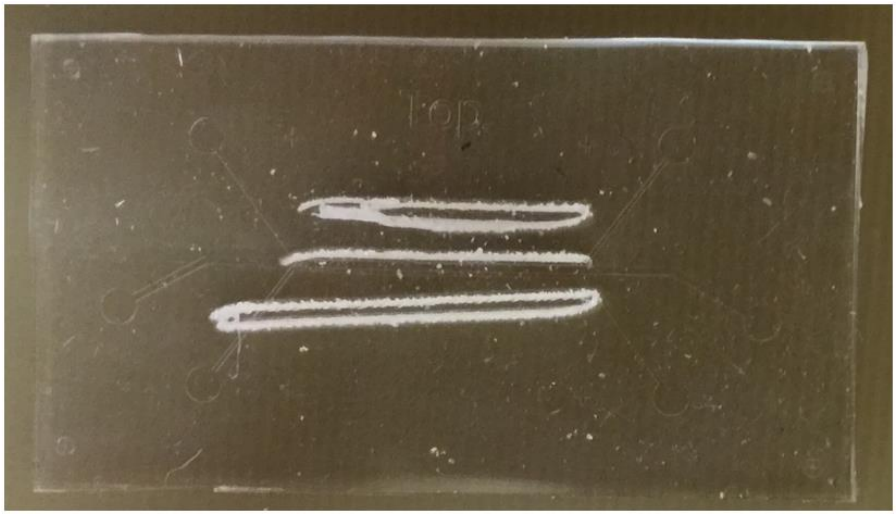

Figure 45: CNC cuts using a 200 μm bit at a feed rate of 600 mm/min and spindle speed of 20,000 rpm. After alignment, the center cut was made in one pass, with a depth of approximately 1.5 mm. The other two cuts (above and below the center cut) were made with a two-pass method, where the first pass went only half the depth and the second pass went the remainder of the depth. Flexing of the PDMS polymer is shown in the curve at the start of the center cut and by the two pass method, where the paths of the passes don't overlap.

The curvature exhibited by the center cut, caused the path to veer outside of the center channel, despite proper alignment. To determine if the curvature could be minimized by making shallower cuts, two subsequent CNC cuts were performed on the same PDMS top layer (seen above and below the center cut). These cuts used two shallow passes in a down and back pattern, milling half

the depth (approximately 750 μm) on the first pass and the remainder of the depth on the second. As Figure 45 demonstrates, despite halving the depth of the cut, the same curvature exists, but now there is an additional curve on the return pass. When reversing direction, rather than returning along the same path, the second pass also curved, forming the elliptical pattern shown. As a result all subsequent CNC cuts were performed with one pass.

Further tests showed that the degree to which the polymer flexed was a function of the surface area of the triangular bit. Using the 100 μm triangular bit, the degree of polymer flex resulted in a path that was improved relative to the larger bit (comparing center cut of Figure 45 to Figure 46). Adjustments were also made to the feed and speed of the cut for the 100 μm bit, focusing on minimizing the curvature produced during the milling process. The resulting path was nearly within the channel (Figure 46). Tape was also used in an effort to secure the PDMS and minimize flexing. However, repeated evaluations demonstrated that even this degree of flexing would breach the thin sidewall of the channel.

As mentioned, at the dimensions necessary for this work, the only commercially available bit styles are triangular in shape due, presumably, to the difficulty in fabricating a 100 μm rectangular end bit with cutting flutes. Additionally, these 100 μm bits represented the smallest available bits of any kind. However, a rectangular end bit was available in the Adams Microfabrication Facility with a diameter of 1/64 of an inch or 396.9 μm. While this bit was too wide for use in opening the 400 μm center channel, the different geometry did provide an opportunity to evaluate whether the triangular shape of the bit was causing the polymer flexing. The results of this test, which can be seen in Figure 46, demonstrate that this is in fact the case. The cut made by the 400 μm rectangular end bit did not curve at the starting point, as all the other cuts had. Without this curve, the cut remained in the intended path, despite producing rough edges. These results imply that if a

rectangular end bit was available in a smaller diameter, this CNC method could be used for this work. Consequently, another method was evaluated to open the PDMS top layer that still utilized the superior alignment of the CNC.

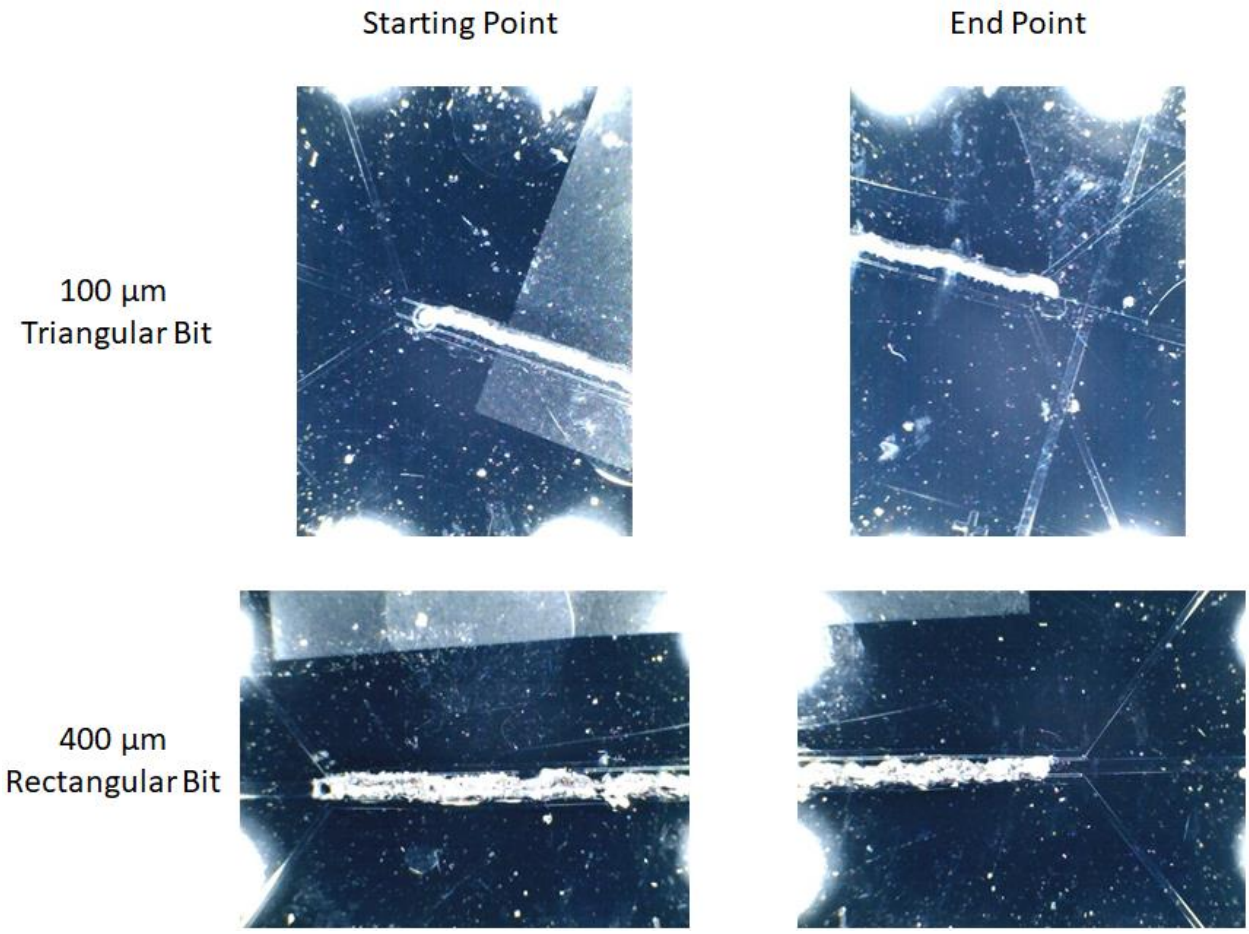

Figure 46: Images taken by a handheld digital microscope of the starting and end points of two CNC cuts made by different types of bits, both performed at a spindle speed of 25,000 rpm and a feed rate of 300 mm/min. Above: 100 µm triangular bit. Below: 400 µm rectangular end bit.

The PDMS top layer was instead placed channel side up. After alignment, the 100 µm bit was used to mill a shallow trench in the center channel 350 µm in depth. Such a shallow cut did not result in significant flexing of the polymer. Using the trench as a guide, a scalpel was used to extend the cut through the remainder of the PDMS top layer, fully opening the channel. Without the aid of the trench, a scalpel cut made by hand could easily veer into the side channel. A cross-sectional

image of a cut made by this method at two points along the channel can be seen in Figure 47. These images demonstrate that this two-step process of opening the channel can produce an open air interface without disrupting the sidewalls.

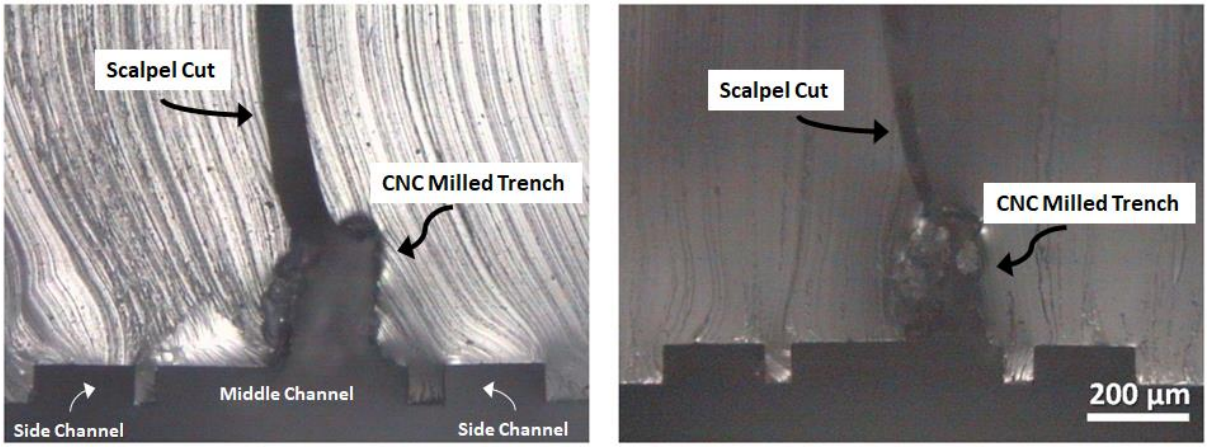

Figure 47: Cross-sectional views (5X magnification) at two points along the channels of a PDMS top layer, showing the ability to create an open top channel using the CNC trench method and scalpel.

In conclusion, the process of opening the top layer of the lung-on-chip device using laser ablation or CNC milling was primarily limited by the depth of the cut being made. In the case of laser ablation, decreasing the thickness of the PDMS layer improved this method but consistency of the resulting cut was a problem. Additionally, aiming the beam of the laser proved to be quite difficult given the channel width constraints. For CNC milling, creating a linear cut without an initial curvature (which altered the path of cut) was problematic due to the viscoelasticity of the polymer. Optimizations to milling feeds and speeds could minimize this curvature but not eliminate it. However, alignment was precise and relatively simple with the aid of a handheld digital microscope. Ultimately, the cuts made by CNC milling were significantly more consistent than those made by laser ablation and alignment was greatly improved. A CNC milling method, where the CNC is first used to create a shallow trench along the channel and a scalpel cut is made, following the trench as a guide, could be used to fully open the top layer prior to assembling the device.

4.4 Assembling the Lung-on-Chip

Chapter 4 of this thesis has described the outcomes of an iterative process of the microfabrication of each component of the multilayer lung-on-chip device. The goal of this process was the construction of a device with an open channel in the PDMS top layer, well-suited for modeling the alveolar-capillary interface in a healthy lung and in a lung with adult respiratory distress syndrome.

As mentioned in section 3.2, the fabrication of the lung-on-chip could be broken into five broad steps of construction: 1) Fabrication of master wafers using photolithography; 2) Creation of top and bottom PDMS layers using replica molding of the SU-8 master wafers made in step one; 3) The creation of a porous membrane; 4) Opening of the top layer of the device and 5) Assembling the 3 layers after careful alignment.

Standard casting methods described in section 3.2.1 successfully produced the top and bottom PDMS layers of the device. PDMS bottom layers were repeatedly made for evaluating the methods used to create the PM and The PDMS top layers were repeatedly made for evaluating methods used to open the center channel of the top layer. To fabricate a PM that both had through holes and could be bonded, intact, to a PDMS bottom layer the stamp method with PFOTS as a release agent was used.

In order to bond the PM to the bottom layer, the first step in assembling the full device, a handheld corona generator was used. Although considerably simpler plasma oxidation by the Harrick plasma cleaner, the handheld corona generator was found to create a much better and more consistent bond between the PDMS pieces. Consequently, in subsequent work only the corona generator was used for PDMS-PDMS bonding. To bond the PDMS, the corona generator was applied to the surface of the PDMS for 1 minute 40 seconds. Bonding was performed by first placing a clean bottom layer on a surface, channel side up. Alongside was placed the sacrificial PDMS slab that held the

PM, PM side up. The PM and bottom layer were both oxidized prior to being brought into contact and this assembly was placed in the oven at 70 °C overnight to irreversibly bond the two layers as described in Section 3.2.5. When bringing the two layers into contact, the channels were placed on a defect-free region of the PM. This process was made simpler, when the PM was made from the master wafer created using the second generation of AutoCad designs, where the width of the PM array was made significantly larger than the width of the channel region (Section 4.1). With this new master wafer, alignment of the channels to the PM was no longer a problem and defect-free regions were available. When PFOTS was used as a release agent, intact PM layers were transferred to the bottom layer after the bonded layers were peeled from the sacrificial slab, thereby creating the PM/bottom (PMB) layer.

To finish assembling the device, the top layer, channel side up, and the PMB layer assembly, PM side up, were oxidized using the same bonding method just described. For this bonding step, however, careful alignment is paramount. The three channels of the top and bottom layers must overlap precisely on either side of the intervening PM for the two sidewalls to properly bond along the entire length of the channels, thereby ensuring that the three channels are independent of one another. When the sidewalls did not bond properly, fluid flowing in the side channels would leak into the center channel. Such a device would not be able simulate breathing as is described in Section 1.3. Cross-sectional views of fully-assembled devices used to examine the through-holes of the PM, were also beneficial in assessing alignment, however, cross-sectioned devices can no longer be used. To assess alignment without destroying the device, the overlapping channels were viewed from the top down and visually inspected. From this perspective, the lines created by the channel walls should nearly overlap when aligned. Additionally the channels were filled with food coloring to determine whether or not there was leakage between channels.

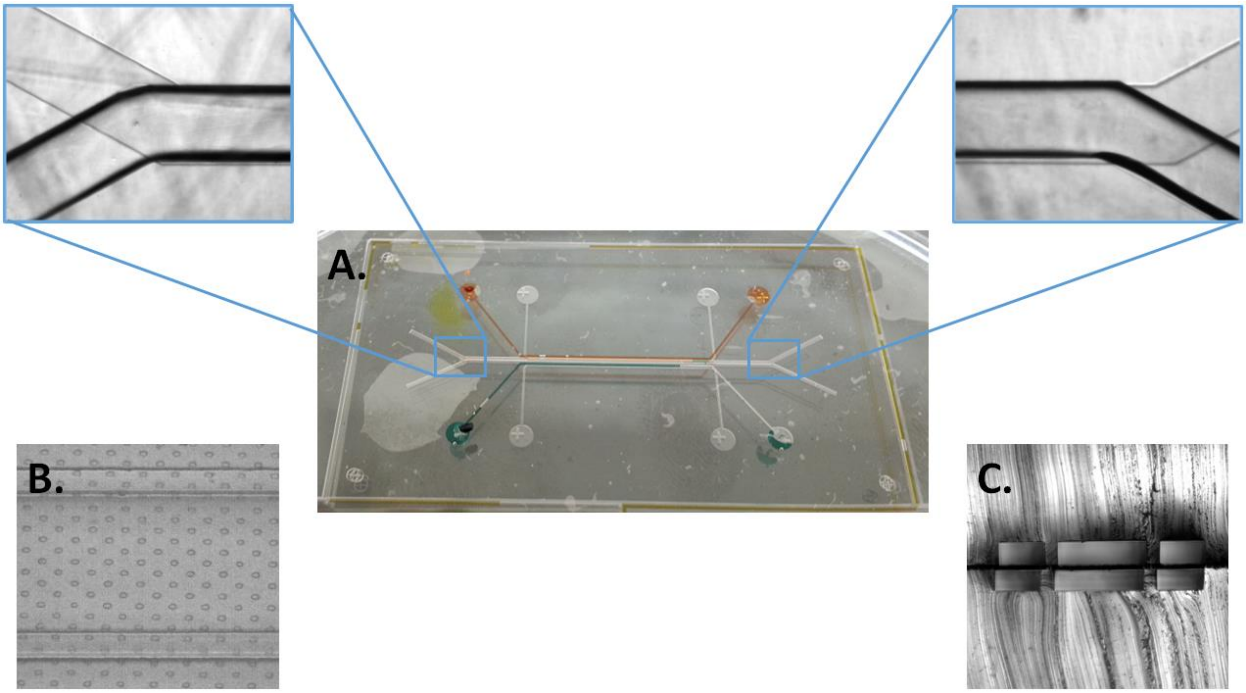

Figure 48: A) Image of a fully-assembled device, with food coloring in the side channels to verify that leaking does not occur. In the expanded views, the walls of the center channel are seen to overlap almost perfectly on both ends, indicating alignment, along the entire length of the device. B) Another top down image of the three assembled layers. Again, the lines made by the walls of the top and bottom layers appear to be perfectly aligned. C) A cross-sectional image, also demonstrating alignment of the sidewalls.

While the assembled device shown here does not have an open top, bonding of an open top layer to a PMB assembly could be performed using the same technique. Methods used to open the top layers obscured the channels of this layer (Figure 46), greatly impairing alignment of the top and bottom layers. Using the CNC to mill a "trench" on the channel side of the top layer, and then using this trench as a guide for a scalpel to cut through remaining thickness of PDMS (Section 4.3.2) was the best method to open the top channel without destroying the sidewalls. Additionally, the slice made by the scalpel made a clean cut that did not obscure the channel features to the extent that the other methods did, making this method ideal for aligning purposes as well.

5. Conclusion and Future Direction

5.1 Conclusion

Although several clinical LS replacement formulations exist to treat conditions in which LS is missing (such as NRDS), there are not currently any LS treatments for disease states in which LS function has been displaced or inhibited (such as ARDS). To address this unmet need and to further improve LS formulations used in treating NRDS, it is necessary to evaluate the role of the individual LS components in overall LS function and to understand how the LS components interact in mixtures. This improved understanding could be used to tailor synthetic LS formulations to the specific disease state. Furthermore, the function of LS should be evaluated within a microenvironment, mimicking the alveoli. To this end, the work described in this thesis details the construction of a three layer PDMS lung-on-chip device well suited to study LS mixtures in health and in a disease model of ARDS all while recapitulating the function and scale of the alveolar-capillary interface.

Three SU-8 master wafers were fabricated with photolithography to be used in creating each of the three individual PDMS layers of the lung-on-chip device. The top and bottom layers were made via standard PDMS casting. Two methods were evaluated for the creation of the porous membrane layer. The first of these used a casting method in which a thin layer of PDMS was spin coated onto the microfabricated posts of the PM master wafer. Unfortunately, the results of this method were unsatisfactory, resulting in pores that were sealed on one side. Additionally, the membrane, when through-holes did exist, was found to be too fragile to remove from the master wafer without damage. Consequently, a second method of creating the porous membrane was evaluated. This method used a stamping process in which the PDMS film was first spin coated onto a sacrificial PDMS slab and then weighted onto the posts of the master wafer before curing to thereby stamp

through-holes into the film. Both the sacrificial slab and the master wafer were silanized to aid in release of the PM first from the master wafer and later from the slab. The first attempt at silanization, using vapor-deposited HMDS, was found to be insufficient. However, vapor deposition of PFOTS allowed the PDMS PM to be easily removed from both the master wafer and the slab. By using the stamp method with PFOTS, a fully-assembled lung-on-chip device was constructed with an intact porous membrane in place.

In an effort to create an open air-liquid interface on the alveolar side of the compartmentalized center channel, two methods were again evaluated. The first of these was a laser ablation method. This method, used a focused CO_2 laser to selectively ablate the PDMS that covered the center channel of the top PDMS layer of the device. In order to remove *only* the region of PDMS over the top layer, without etching too deep or into the nearby sidewalls, several power levels and speeds were evaluated. However, in the end this technique was found to either result in excessive burning of the nearby PDMS, insufficient ablation, or non-uniform ablation. As a result, a second method for opening the center channel of the top layer was evaluated: precision CNC milling. In this method the top layer of the lung-on-chip device was fixed to a surface. Following this, a milling bit 100 μm or 200 μm in diameter was aligned using a digital light microscope before the CNC was used to cut a programmed path through the PDMS layer. The CNC could be programmed to cut all the way through in the Z direction while the path in the XY plane remained a straight line. Multiple speeds for both the feed rate of the bit in the XYZ coordinate system and the revolutions per minute of the milling bit were evaluated. The result of this method was promising and typically resulted in a straight cut with a slight curve as the polymer flexed toward the beginning of the cycle. Using the CNC to cut a shallow trench along the center channel of the PDMS top layer and using a scalpel to cut through to the other side of this layer by following the trench as guide, proved to be the best method for opening the center channel without damaging the sidewalls.

5.2 Future Direction

Given these results, future work will focus on the continued evaluation of the CNC milling method for the opening of the lung-on-chip device. A primary shortcoming of this method has been the tendency of the polymer to flex as it is being milled. This could potentially be addressed however via better methods of fixing the PDMS layer to the milling surface temporarily or through changes in milling speeds. A rectangular end bit with a tip diameter of less than 400 μm could result in straighter cuts without damaging the side wall. The CNC milled top layer will then be bonded to the PM (made via the stamp method and already irreversibly bonded to the bottom layer) following the same procedure used for the closed device.

Completing this lung-on-chip *in vitro* model requires a device capable of breathing with cultured alveolar cells grown on the PM layer. The process of etching the PM from the side channels to create side chambers is the first step in making the device breathe. A 1:3 volumetric mixture of tetrabutylammonium fluoride (TBAF): N-methylpyrrolidinone (NMP) will be used as a PDMS etchant. The solution will be pulled through the side channels using vacuum suction, etching the PM away completely and etching the sidewalls until they are less than 30 μm thick. The side chambers will then be flushed with NMP to flush out any remaining etchant (TBAF). Prior to cell seeding, the assembled lung-on-chip device will be sterilized through UV irradiation and the PM will be coated with extracellular matrix (ECM). We plan to culture a model lung epithelial cell line (A549 from ATCC) on the PM following the protocol outlined by Huh et al [32].

We will collaborate with Dr. Yong Zeng to integrate negative pressure control with the lung-on-chip device to incorporate mechanical stretching of the PM, mimicking the mechanical cues experienced by the lung cells during the ever present cycle of breathing.

Finally, the completed device will allow for the evaluation of LS in an *in vitro* model of healthy lung function and in an *in vitro* model of ARDS. In the ARDS model, the lower channel will be

pumped with a solution containing serum proteins, such as albumin. In both of these models an active microrheology system unique to our lab will be used to obtain surface viscosities and fluorescence microscopy will be used to visualize the LS domain morphology. The microenvironment of this lung-on-chip device uniquely allows the ARDS model because the presence of the lower channel enables the introduction of LS inhibitor proteins and the porous membrane allows uptake of the proteins by the alveolar side of the PM, modeling ARDS.

References

1. Güder, F., et al., *Paper-Based Electrical Respiration Sensor.* Angewandte Chemie, 2016. **128**(19): p. 5821-5826.
2. Campbell, N. and J. Reece, *Biology 7th edition, AP*. 2005, Pearson, Education Inc: San Francisco, CA. p. 886-895.
3. Patton, K.T. and G.A. Thibodeau, *Anatomy & Physiology-E-Book*. 2014: Elsevier Health Sciences.
4. Porter, M.R., *Handbook of surfactants*. 2013: Springer.
5. Zasadzinski, J., et al., *The physics and physiology of lung surfactants.* Current Opinion in Colloid & Interface Science, 2001. **6**(5): p. 506-513.
6. Serrano, A.G. and J. Pérez-Gil, *Protein–lipid interactions and surface activity in the pulmonary surfactant system.* Chemistry and physics of lipids, 2006. **141**(1): p. 105-118.
7. Dobbs, L.G., *Pulmonary surfactant.* Annual review of medicine, 1989. **40**(1): p. 431-446.
8. Pérez-Gil, J., *Molecular interactions in pulmonary surfactant films.* Neonatology, 2002. **81**(Suppl. 1): p. 6-15.
9. Pramanik, A.K. *Respiratory Distress Syndrome*. 2015.
10. Notter, R.H., *Lung surfactants: basic science and clinical applications*. 2000: CRC Press.
11. Bolt, R.J., et al., *Glucocorticoids and lung development in the fetus and preterm infant.* Pediatric pulmonology, 2001. **32**(1): p. 76-91.
12. Gross, I., *Regulation of fetal lung maturation.* American Journal of Physiology-Lung Cellular and Molecular Physiology, 1990. **259**(6): p. L337-L344.
13. Raj, J.U. and J.R. Wright, *Respiratory Distress Syndrome of the Newborn*, in *Breathing in America: Diseases, Progress and Hope*. 2010, American Thoracic Society. p. 197-206.
14. El-Gendy, N., et al., *Delivery and performance of surfactant replacement therapies to treat pulmonary disorders.* 2013.
15. Marchetti, N. *Acute Respiratory Distress Syndrome (ARDS)*. 2016.
16. Raghavendran, K., D. Willson, and R. Notter, *Surfactant therapy for acute lung injury and acute respiratory distress syndrome.* Critical care clinics, 2011. **27**(3): p. 525-559.
17. Chakraborty, A., et al., *Combined effect of synthetic protein, Mini-B, and cholesterol on a model lung surfactant mixture at the air-water interface.* Biochim Biophys Acta, 2016. **1858**(4): p. 904-12.
18. Dhar, P., et al., *Active interfacial shear microrheology of aging protein films.* Physical review letters, 2010. **104**(1): p. 016001.
19. Ghazvini, S., et al., *Monitoring phases and phase transitions in phosphatidylethanolamine monolayers using active interfacial microrheology.* Soft Matter, 2015. **11**(17): p. 3313-21.
20. Whitesides, G.M., *The origins and the future of microfluidics.* Nature, 2006. **442**(7101): p. 368.
21. Voldman, J., M.L. Gray, and M.A. Schmidt, *Microfabrication in biology and medicine.* Annual review of biomedical engineering, 1999. **1**(1): p. 401-425.
22. Madou, M.J., *Fundamentals of Microfabrication*. 1997, Boca Raton, FL: CRC Press.
23. Gravesen, P., J. Branebjerg, and O.S. Jensen, *Microfluidics-a review.* Journal of Micromechanics and Microengineering, 1993. **3**(4): p. 168.
24. Duffy, D.C., et al., *Rapid prototyping of microfluidic systems in poly (dimethylsiloxane).* Analytical chemistry, 1998. **70**(23): p. 4974-4984.
25. Haubert, K., T. Drier, and D. Beebe, *PDMS bonding by means of a portable, low-cost corona system.* Lab on a Chip, 2006. **6**(12): p. 1548-1549.
26. Potkay, J.A., *The promise of microfluidic artificial lungs.* Lab on a Chip, 2014. **14**(21): p. 4122-4138.
27. Streets, A.M., et al., *Microfluidic single-cell whole-transcriptome sequencing.* Proceedings of the National Academy of Sciences, 2014. **111**(19): p. 7048-7053.

28. Ziaie, B., et al., *Hard and soft micromachining for BioMEMS: review of techniques and examples of applications in microfluidics and drug delivery.* Advanced drug delivery reviews, 2004. **56**(2): p. 145-172.
29. Qin, D., Y. Xia, and G.M. Whitesides, *Soft lithography for micro-and nanoscale patterning.* Nature protocols, 2010. **5**(3): p. 491.
30. Oborny, N.J., et al., *Evaluation of a Portable Microchip Electrophoresis Fluorescence Detection System for the Analysis of Amino Acid Neurotransmitters in Brain Dialysis Samples.* Analytical Sciences, 2016. **32**(1): p. 35-40.
31. Saylor, R.A. and S.M. Lunte, *A review of microdialysis coupled to microchip electrophoresis for monitoring biological events.* Journal of Chromatography A, 2015. **1382**: p. 48-64.
32. Huh, D., et al., *Microfabrication of human organs-on-chips.* Nature protocols, 2013. **8**(11): p. 2135.
33. Abgrall, P. and A. Gue, *Lab-on-chip technologies: making a microfluidic network and coupling it into a complete microsystem—a review.* Journal of Micromechanics and Microengineering, 2007. **17**(5): p. R15.
34. Morgan, S., et al., *The cost of drug development: a systematic review.* Health Policy, 2011. **100**(1): p. 4-17.
35. Shuler, M.L., *Organ-, body-and disease-on-a-chip systems.* Lab on a Chip, 2017. **17**(14): p. 2345-2346.
36. Bhise, N.S., et al., *Organ-on-a-chip platforms for studying drug delivery systems.* Journal of Controlled Release, 2014. **190**: p. 82-93.
37. Selimović, Š., M.R. Dokmeci, and A. Khademhosseini, *Organs-on-a-chip for drug discovery.* Current opinion in pharmacology, 2013. **13**(5): p. 829-833.
38. Esch, E.W., A. Bahinski, and D. Huh, *Organs-on-chips at the frontiers of drug discovery.* Nature reviews. Drug discovery, 2015. **14**(4): p. 248.
39. Bhatia, S.N. and D.E. Ingber, *Microfluidic organs-on-chips.* Nature biotechnology, 2014. **32**(8): p. 760-772.
40. Huh, D., et al., *A human disease model of drug toxicity–induced pulmonary edema in a lung-on-a-chip microdevice.* Science translational medicine, 2012. **4**(159): p. 159ra147-159ra147.
41. Huh, D., et al., *Reconstituting organ-level lung functions on a chip.* Science, 2010. **328**(5986): p. 1662-1668.
42. Grosberg, A., et al., *Ensembles of engineered cardiac tissues for physiological and pharmacological study: heart on a chip.* Lab on a chip, 2011. **11**(24): p. 4165-4173.
43. Kim, H.J., et al., *Human gut-on-a-chip inhabited by microbial flora that experiences intestinal peristalsis-like motions and flow.* Lab on a Chip, 2012. **12**(12): p. 2165-2174.
44. Toh, Y.-C., et al., *A microfluidic 3D hepatocyte chip for drug toxicity testing.* Lab on a Chip, 2009. **9**(14): p. 2026-2035.
45. Eisenstein, M., *Artificial organs: Honey, I shrunk the lungs.* Nature, 2015. **519**(7544): p. S16-S18.
46. Dammel, R.R., *Diazonaphthoquinone-based Resists*. Vol. TT-11. 1993, Bellingham, WA: SPIE Optical Engineering Press.
47. Henderson, C. *Brief History of and Introduction to Integrated Circuits, Lithography, and Photoresists*.
48. Martinez-Duarte, R. and M.J. Madou, *SU-8 photolithography and its impact on microfluidics.* Microfluidics and Nanofluidics Handbook, 2011: p. 231-268.
49. Lima, R.S., et al., *Sacrificial adhesive bonding: a powerful method for fabrication of glass microchips.* Scientific reports, 2015. **5**.
50. Altpeter, D.M., *Description of SU-8.* 2005.
51. Ito, H., *Chemical amplification resists: History and development within IBM.* IBM Journal of research and development, 1997. **41**(1.2): p. 119-130.

52. Martinez-Duarte, R. and M.J. Madou, *SU-8 Photolithography and Its Impact on Microfluidics*, in *Microfluidics and Nanofluidics Handbook*. 2011. p. 231-268.
53. Franssila, S., *Wafer Cleaning and Surface Preperation*, in *Introduction to Microfabrication*. 2010, John Wiley & Sons. p. 143-152.
54. *Technical Bulletin*. Photoresist Adhesion and HMDS (hexamethyldisilazane) Processing; Available from: www.imicromaterials.com/index.php/technical/HMDS.
55. Law, K.-Y., *Definitions for hydrophilicity, hydrophobicity, and superhydrophobicity: getting the basics right*. 2014, ACS Publications.
56. Yuan, Y. and T.R. Lee, *Contact angle and wetting properties*, in *Surface Science Techniques*. 2013, Springer. p. 3-34.
57. *SU-8 Negative Tone Photoresist Formulations 50-100 Datasheet*. 2002.
58. Lisensky, G.C., et al., *Replication and compression of surface structures with polydimethylsiloxane elastomer.* J. Chem. Educ, 1999. **76**(4): p. 537.
59. Natarajan, S., D. Chang-Yen, and B. Gale, *Large-area, high-aspect-ratio SU-8 molds for the fabrication of PDMS microfluidic devices.* Journal of Micromechanics and Microengineering, 2008. **18**(4): p. 045021.
60. Shao, G., et al., *Fabrication of elastomeric high-aspect-ratio microstructures using polydimethylsiloxane (PDMS) double casting technique.* Sensors and Actuators A: Physical, 2012. **178**: p. 230-236.
61. Fogarty, B.A., et al., *Rapid fabrication of poly (dimethylsiloxane)-based microchip capillary electrophoresis devices using CO 2 laser ablation.* Analyst, 2005. **130**(6): p. 924-930.
62. Huft, J., et al., *Three-dimensional large-scale microfluidic integration by laser ablation of interlayer connections.* Lab on a Chip, 2010. **10**(18): p. 2358-2365.